DENSE METAL AND PEROVSKITE MEMBRANES FOR

HYDROGEN AND PROTON CONDUCTION

A **Thesis**
Presented to
The Academic Faculty

by

Sung Gu Kang

In Partial Fulfillment
of the Requirements for the Degree
Doctor of Philosophy in the
School of Chemical & Biomolecular Engineering

Georgia Institute of Technology
August 2013

DENSE METAL AND PEROVSKITE MEMBRANES FOR

HYDROGEN AND PROTON CONDUCTION

Approved by:

Dr. David S. Sholl, Advisor
School of Chemical & Biomolecular
Engineering
Georgia Institute of Technology

Dr. William J. Koros
School of Chemical & Biomolecular
Engineering
Georgia Institute of Technology

Dr. Christopher W. Jones
School of Chemical & Biomolecular
Engineering
Georgia Institute of Technology

Dr. Michael A. Filler
School of Chemical & Biomolecular
Engineering
Georgia Institute of Technology

Dr. Seung Soon Jang
School of Materials Science and Engineering
Georgia Institute of Technology

Date Approved: [March 25, 2013]

To my families and friends,

For always being there to support me,

ACKNOWLEDGEMENTS

Ken Onubogu for their kindness, friendship, and support. My friends outside the group, Jason Bentley, Andaç Armutlulu, and Shannon Capps, thank you for sharing the great moments and memories in my life in Atlanta. I would like to express my special thanks for my brothers and sisters who shared joy, sorrow, and time of fellowship with me in the name of Jesus Christ. I also want to acknowledge the friendship of the members of the Korean ChBE Association and Graduate & Family Housing at Georgia Tech.

Finally, I would like to extend my deepest gratitude to my family. The successful completion of my Ph.D. study would not have been possible without the continuous support, love, and prayer of my parents and my brother. Last but not least, I thank God for His love.

Sung Gu Kang

March, 2013, in Atlanta, GA, USA

TABLE OF CONTENTS

LIST OF TABLES

LIST OF FIGURES

SUMMARY

Hydrogen is an attractive alternative energy resource, but pure hydrogen gas does not exist naturally. It is imperative to separate hydrogen from mixed gas streams including CO, CO_2, CH_4, and H_2S when hydrogen is obtained from fossil fuels. The development of hydrogen purification membranes that can operate at high temperatures and pressures is a significant challenge. First-principles modelings are used to predict hydrogen permeability through Palladium (Pd)-rich binary alloy membranes as a function of temperature and H_2 pressure. In previous approaches to this topic, complex models were used with which investigation of new membranes required significant time and effort to predict hydrogen permeability. We introduce a simplified model that incorporates only a few factors and yields quantitative prediction. This model is used to predict hydrogen permeability in a wide range of binary alloy membranes and to find promising alloys that have high hydrogen permeability.

Tritium can be dangerous when absorbed through the skin or ingested by water. Therefore, the US Nuclear Regulatory Commission (NRC) and the US Environmental Protection Agency (EPA) regulate the emission of tritium to the environment. In order to separate tritium from helium cooled gas streams in a very-high-temperature gas-cooled reactor, we study a tritium permeation membrane based on perovskites. We show how our efficient Density Functional Theory (DFT)-based model predicts the chemical stability and proton conductivity of doped barium zirconate ($BaZrO_3$), barium stannate ($BaSnO_3$), and barium hafnate ($BaHfO_3$). Our data is also used to explore the physical origins of the trends in chemical stability and proton conductivity among different

dopants. We also study potassium tantalate ($KTaO_3$), which is a prototype perovskite, to examine the characteristics of undoped perovskites. Specifically, we study the impacts of isotope effects, tunneling effects, and native point defects on proton mobility in $KTaO_3$.

Rechargeable Li-ion batteries are important power sources for many portable electronic devices and electric vehicles. It is important to find and develop solid-state Li-ion electrolyte materials that are chemically stable and have high ionic conductivities for high performance Li-ion batteries. A number of garnet-related structures have been suggested for their application, but little is known about the stability of these materials. We show how we predict the chemical stability of $Li_7La_3Zr_2O_{12}$, $Li_7La_3Sn_2O_{12}$, and $Li_7La_3Hf_2O_{12}$ with respect to carbonate and hydroxide formation reactions. We also demonstrate that the partial pressure of CO_2 and H_2O is an important factor affecting their chemical stability.

CHAPTER 1

INTRODUCTION

1.1   Metal membranes in H_2 purification

Hydrogen is an attractive alternative to traditional fossil fuels. It is a plentiful resource with massive energy density.[1] Two commonly used processes for hydrogen production are water electrolysis and extraction from fossil fuels. Since considerable energy is required for water splitting, hydrogen is mostly produced by steam reforming or partial oxidation of hydrocarbons.[2] These processes generate CO, CO_2, CH_4, and H_2S as by-products. Therefore, it is important to purify hydrogen from these mixed gas streams in order to use hydrogen as a fuel source.[3]

The development of hydrogen separation membranes that can be operated at elevated temperatures and pressures is an important challenge. High hydrogen fluxes, resistance to sulfur poisoning, and operational longevity are significant goals in the field of hydrogen purification. Metal membranes are appropriate for high-temperature applications.[4] Palladium (Pd)-based metal membranes are attractive due to their infinite selectivity for H_2 over other species.[5] However, for pure Pd membranes, H_2-induced embrittlement can occur readily at temperatures below about 300°C.[6] Pure Pd membranes are also susceptible to sulfur poisoning.[7] As seen in Figure 1.1, the process of hydrogen transport across metal membranes involves multiple steps[4]: 1. Movement of the H_2 to surface, 2. Dissociation of H_2 into H, 3. Adsorption of H into the membrane, 4. Diffusion of H through the membrane, 5. Desorption of H to the membrane surface, 6. Reassociation of H into H_2, 7. Movement of H_2 molecules away from the membrane.

1

This description of hydrogen permeation suggests that a good H_2 selective membrane must ideally have high catalytic activity for H_2 dissociation, high solubility and rapid diffusion of interstitial H.
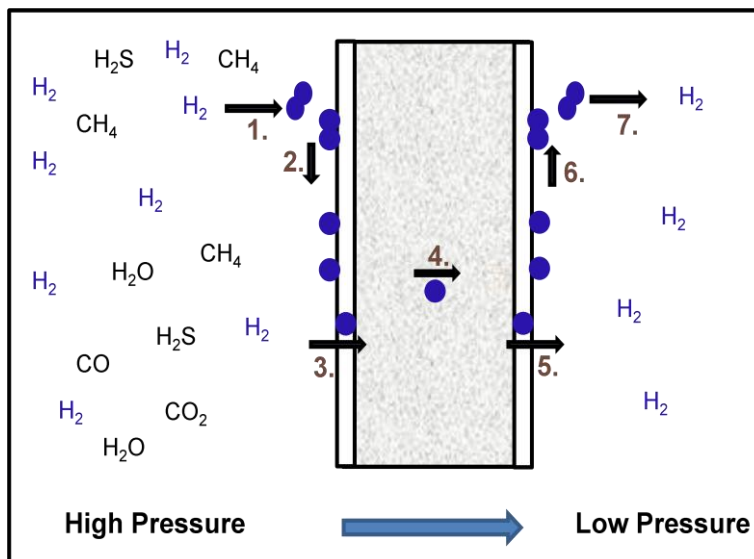
Figure 1.1: Schematic illustration of the process of net H_2 transport through a metal alloy membrane.

To improve the performance of pure metal membranes, metal alloys can be considered. Pd is considered to be the premier material for binary metal membranes, usually alloyed with elements including Ag, Au, B, Ce, Cu, Fe, Ni, Pt, Rh, or Y among others as additive metal atoms.[8] Experimentally, the development and characterization of new metal membranes require significant investments of resources and time. One aim of my work is to develop a theoretical method to identify alloys with promising properties. The adsorption and diffusion of H in amorphous metals has been studied by Hao and Sholl with related theoretical methods.[9]

Many binary and ternary alloys have been studied, and a small number of materials with higher permeability than Pd are known.[3, 8] In particular, PdAg alloys have been used in practical applications because their H_2 permeability is ~50% higher than Pd. In Chapter 3, we use quantitative computational modeling to systematically predict the H_2 permeability of *all* Pd-rich FCC binary alloys with the aim of finding alloys with higher H_2 permeability than pure Pd. We restrict our attention to substitutionally disordered FCC alloys with composition $Pd_{96}M_4$ (in at.%). This composition is convenient for the computational modeling described below and allows a wide range of alloying elements to be considered. Some elements do not form solid solutions with Pd at this composition, so this restricts the number of alloying elements we can consider. 50 elements are known to form solid solutions with Pd at this composition at ~600 K, and we examine all of these elements.

1.2   Proton-conducting perovskites

Negative environmental impacts of fossil fuels (coal, oil, natural gas, and shale gas) and issues with petroleum supplies have spurred interest in alternative fuels. Among the many alternative fuels, hydrogen fuels have received a great deal of attention and this is the focus of our study. Very High Temperature Gas-Cooled Reactors (VHTR) in Generation IV Next Generation Nuclear Plant (NGNP) systems can produce hydrogen from only heat and water.[10] To avoid hazards associated with radioactive toxicity, it is necessary to remove the trace levels of tritium or tritiated species in exhaust gas streams. Therefore, it is important to separate tritium, a radioactive fission product from the high temperature gas stream, to safely utilize this available exhaust heat to produce hydrogen.

Our work is motivated by tritium sequestration technologies based on ceramic membranes such as proton-conducting perovskites. A Perovskite structure has the general chemical formula $A^{x}B^{6-x}O_3$, where the A-site cations have 1^+, 2^+ or 3^+ charge and the B-site cations have 5^+, 4^+ or 3^+ charge, respectively. The cubic perovskite structure is shown in Figure 1.2.
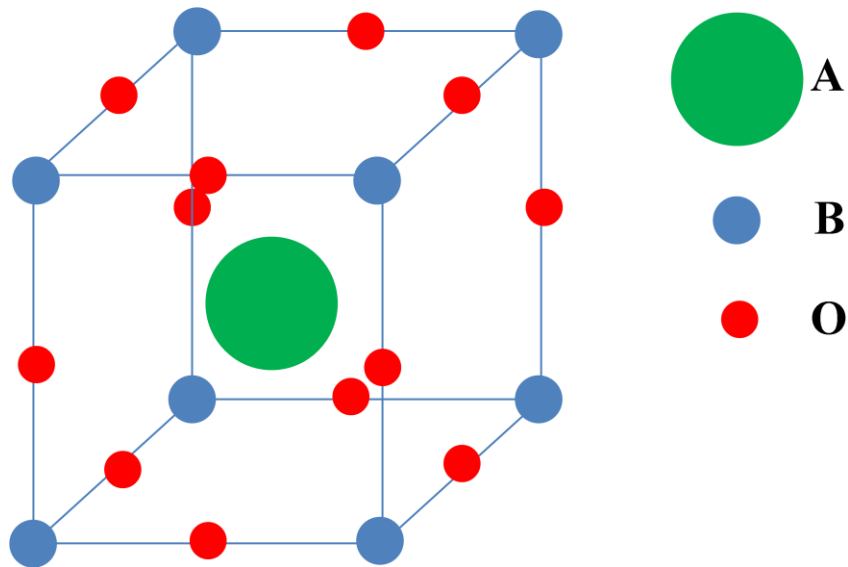
Figure 1.2: Schematic plot of perovskite crystal structure (ABO_3), where the red spheres are the oxygen ions, blue spheres are the B cations, and green sphere is the A cation.

Perovskite-type oxides are candidates for proton-conducting electrolytic materials in applications such as fuel cells, gas sensors, ceramic membranes and steam electrolysers.[11, 12] Ceramic proton-conducting perovskites with dopants providing high proton conductivity are attractive for these technologies.[13] Protons form a covalent bond with the oxygen lattice in perovskite oxides.[10, 11] Proton migration in doped perovskites occurs through two sequential elementary steps: transfer of protons between adjacent oxide ions and rotation.[14] Kreuer noted that proton diffusion can be affected by symmetry

reduction and chemical disruption due to the presence of dopants.[13]

1.2.1   B-site doped Barium Zirconate (BaZrO$_3$)

Perovskite-type oxides are useful materials for proton conduction. A longstanding aim in development of electrolytes is to find dopants that give high proton conductivity coupled with good chemical stability. We use first-principles calculations to address this topic in doped BaZrO$_3$. We use efficient methods to examine a wide range of possible dopants. Specifically, we present results for BaZrO$_3$ doped with Y, In, Ga, Sc, Nd, Al, Tl, Sm, Dy, La, Pm, Er, and Ho in Chapter 4. These calculations correctly identify the doped BaZrO$_3$ materials that are already known to have favorable properties, but also highlight a number of promising materials that have not been examined previously. We investigate the physical origins of the trends in chemical stability and proton mobility among different dopants. Our data allows us to consider several possible physical descriptors for characterizing doped perovskites as proton conductors.

1.2.2   A-site doped and (A, B)-site doped BaZrO$_3$

After examining B-site doped BaZrO$_3$, we extend our first-principles calculations to address this topic in A-site doped and (A,B)-site doped BaZrO$_3$. In particular, we examine BaZrO$_3$ doped with K, Rb, and Cs at A-sites, as well as the pairing of these monovalent alkali dopants at A-site and trivalent dopants at B-site. This work is presented in Chapter 5. We use Y as a representative of a trivalent dopant in this study. We primarily study the formation energy of a wide range of dopant pairs, since the contribution of formation energy to proton conductivity is larger than that of proton

diffusivity. These calculations identify promising pairs of the materials that have not been previously examined. The physical descriptors used in Chapter 4 are also employed to study the trends in chemical stability and proton mobility for perovskites containing different dopants.

1.2.3 B-site doped BaSnO$_3$ and BaHfO$_3$

In Chapter 4, we develop methods to aid in the discovery of the dopant materials by making predictions about chemical stability and proton conductivity of doped BaZrO$_3$ prior to experimental testing. Based on this study, we elucidate chemical stability and proton conductivity of proton conductors through first-principles modeling. From the assessment of the dopants in BaZrO$_3$, we find that Ga-doping shows the highest stability and La-doping leads to the highest proton conductivity in BaZrO$_3$. We extend our studies to the prediction of the chemical stability and proton conductivity of Ga or La-doped barium stannate (BaSnO$_3$) and barium hafnate (BaHfO$_3$) in Chapter 6.

1.2.4 Potassium Tantalate (KTaO$_3$)

KTaO$_3$ (KTO) is a useful prototypical perovskite for examining the mechanisms of proton transport in perovskites. Previously, Gomez *et al.* reported DFT calculations describing proton hopping in defect-free KTO.[15] We use DFT calculations to extend that work in two directions, namely understanding isotope effects in low and high temperature proton transport and the role of native point defects in KTO. At cryogenic temperatures, quantum tunneling plays a vital role in the net hopping of protons in KTO. At the elevated temperature characteristic of applications involving proton-conducting

perovskites, tunneling is negligible but zero point energy effects still lead to non-negligible isotope effects for H^+, D^+, and T^+. We also use DFT to characterize the populations of relevant point defects in KTO as a function of experimental conditions, and to examine the migration of protons that are close in proximity to these defects. This information gives useful insight into the overall transport rates of protons through KTO under a variety of external environments. We also assess the overall diffusivity of protons in KTO at various ranges of oxygen vacancy concentrations by performing Kinetic Monte Carlo (KMC) simulations.

1.3   Chemical stability studies of Li garnet-related structures

Li garnet-related structures are promising solid-state Li-ion electrolytes in Li-ion batteries, which are a potential alternative to fossil fuels. In considering garnets for Li-ion conducting applications, chemical stability is an important problem that needs to be solved. We examine the chemical stability of $Li_7La_3Zr_2O_{12}$, $Li_7La_3Sn_2O_{12}$, and $Li_7La_3Hf_2O_{12}$ with respect to carbonate and hydroxide formation reaction. From these studies, we rank the chemical stability of Li garnet-related structures against CO_2 and H_2O in Chapter 8.

1.4   References

1.   Schlapbach, L., Zuttel, A., *Nature* **2001,** 414, 353-358.
2.   Muradov, NZ., Veziroglu, TN., *Int. J. Hydrogen Energy* **2005**, 30, 225.
3.   Steele, B. C. H., Heinzel, A., *Nature* **2001,** 414, 345-352.
4.   Sholl, D. S., Ma, Y. H., *MRS Bull.* **2006**, 31, 770-773.
5.   Su, C., Jin, T., Kuraoka, K., Matsumara, Y., Yazawa, T., *Ind. Eng. Chem. Res.* **2005**, 44, 3053.
6.   Ke, X., Kramer, G. J., *Phys. Rev. B* **2002**, 66, 184304.
7.   Kamakoti, P., Sholl, D. S., *J. Membr. Sci.* **2003**, 225, 145.
8.   Paglieri, S.N., Way, J.D., *Sep. Purif. Meth.* **2002,** 31, 1-169.
9.   Hao, S. Q., Sholl, D. S., *J. Chem. Phys.* **2009**, 130, 244705.
10.   S, S. *Nuclear reactor/hydrogen process interface*, Department of Energy Hydrogen Program Annual Merit Review Proceedings: Washington, D.C., **2007**.
11.   Iwahara, H., Esaka, T., Uchida, H., Maeda, N., *Solid State Ionics* **1981**, 3-4, 359.
12.   Iwahara, H., *Solid State Ionics* **1992**, 575-586.
13.   Kreuer, K. D., *Annu. Rev. Mater. Res.* **2003**, 33, 333.
14.   Kreuer, K. D., Dippel, T., Hainovsky, N. G., Maier, J., *Ber. Bunsen. Phys. Chem.* **1992**, 96, 1736.
15.   Gomez, M.A., Jindal, S., Fletcher, K. M., Foster, L. S., Addo, N. D. A., Valentin, D., Ghenoiu, C., Hamilton. A., *J. Chem. Phys.* **2007**, 126, 19.

CHAPTER 2

MODELS AND METHODS

2.1   Density functional theory

Density Functional Theory (DFT) is a first-principles theory of electronic ground-state structure based on the electron density distribution.[1, 2] In this section, we present a short overview of DFT methods, which are useful complementary tools.

It is not possible to solve the Schrödinger equation for a many-body system exactly. Therefore, we have to use some approximations to obtain approximate solution to the Schrödinger equation of a many-body system. DFT is based on two core theorems proved by Hohenberg and Kohn and the derivation of a set of equations by Kohn and Sham. Hohenberg and Kohn's first theorem stated that the ground state electron density uniquely determines all ground state properties of the system.[3] In other words, the ground state energy is a unique functional of the electron density. This theorem greatly reduces the number of dimensions in a calculation, since the electron density is only a function of three variables x, y and z, whereas a many-body electronic wave function is a function of $3N$ variables, where N is the number of electrons in the system. However, this theorem cannot define what the actual functional is. The second theorem by Hohenberg and Kohn asserted that the true electron density minimizes the energy of the overall functional. Kohn and Sham showed that the electron density can be obtained from a system of single-electron equations.[4] The Kohn-Sham equations are

$$\left[-\frac{\hbar^2}{2m}\nabla^2 + V(r) + V_H(r) + V_{XC}(r)\right]\psi_i(r) = \varepsilon_i(r)\psi_i(r), \tag{2.1}$$

where m is the electron mass. The four terms in brackets in Equation (2.1) are kinetic energy, the interaction between an electron and the collection of atomic nuclei, the Coulomb repulsion between electrons, and exchange and correlation contributions to the single-electron equations, respectively.

An approximation for the exchange-correlation functional in the Kohn-Sham equations must be specified. These are two well-known approximations to describe this energy functional. One of them is the *local density approximation* (LDA). The LDA uses only the local density to define the approximate exchange-correlation functional. However, this does not provide the true exchange-correlation functional to solve the true Schrödinger equation.[1] Another one is the *generalized gradient approximation* (GGA). Even if the GGA has more physical information from the gradient of the electron density than the LDA, it is not always true that the GGA is more accurate than the LDA. Among GGA functionals, the Perdew-Wang functional (PW91) and the Perdew-Burke-Ernzerhof (PBE) are widely used. There are still issues of using DFT in describing van der Waals forces and estimating band gaps, etc.[1]

We use plane wave DFT calculations using the Vienna *Ab-initio* Simulation Package (VASP).[1, 5-7] The ionic cores are described by ultrasoft pseudopotentials (USPP)[7, 8] or the projector augmented wave (PAW) method[9, 10]. The generalized gradient approximation (GGA) with the Perdew-Wang functional (PW91)[11] or the Perdew-Burke-Ernzerhof (PBE) functional[12, 13] is employed to describe the exchange-correlation contributions to the total energy. Calculation details on each topic are shown in each chapter.

First-principles calculations have been used in the past to successfully describe the adsorption and diffusion behavior of hydrogen in bulk phase of numerous metals and metal alloys (crystalline and amorphous), as well as on their surfaces and subsurface layers without any experimental input.[14-17] In addition, first-principles calculations can provide information about spin-lattice coupling and magnetodielectric effects.[18-21] Moreover, a large number of studies have shown that DFT is quantitatively accurate for describing the tunneling jump rate of H at very low temperatures[22], the free energies of solid phase hydride reactions, and material properties of photovoltaics and batteries.[23-27]

In the following chapters, we discuss in detail how to apply DFT calculations, together with the models introduced above, to obtain the macroscopic properties of H (H^+) in different metal alloys (perovskites).

2.2   Phonon density of states calculations

In this section, we present an overview of the calculations of the phonon density of states (DOS) and vibrational contributions to the free energy we perform using the PHONON code developed by Parlinski.[28] The temperature-dependent free energy of solid phases is derived from the phonon frequencies of the compounds. Classical lattice dynamics are employed to calculate phonon frequencies within the harmonic approximation. This approach constructs the Hessian matrix (or the matrix of force constants) and uses this matrix to build a dynamical matrix for a particular wave vector, k. The dynamical matrix is diagonalized to get phonon frequencies, and the phonon density of states, ($g(\omega)$), is obtained.[29] DFT calculations are firstly performed to optimize a supercell. Then, a series of small displacements of the atoms are made and the

11

Hellman-Feynman forces exerted on all atoms are calculated to yield the force constant matrix. The vibrational contribution to the internal energy is[29]

$$U_{vib}(T) = \int_0^\infty g(\omega)\,\bar{\varepsilon}(\omega, T)d\omega, \tag{2.2}$$

$$\bar{\varepsilon}(\omega) = -\frac{\partial \log(Z(\omega))}{\partial \beta} = \frac{\hbar\omega}{2\tanh\left(\frac{\beta\hbar\omega}{2}\right)}, \tag{2.3}$$

where $Z(\omega)$ is the canonical partition function for a harmonic oscillator, $\beta = 1/kT$, k is Boltzmann's constant, ω is the phonon dispersion frequency, and $g(\omega)$ is the phonon density of states. Once U_{vib} of the compound is known, other thermodynamic properties can be derived from it using the first and second laws of thermodynamics.[29] Within the harmonic approximation, Helmholtz free energy of solid phases is obtained from phonon density of states calculations at the ground state volume. The Helmholtz free energy of solid phases is defined as[30]

$$F = rkT \int_0^\infty g(\omega)\, ln\left[2sinh\left(\frac{\hbar\omega}{2kT}\right)\right]d\omega, \tag{2.4}$$

where r is the number of degrees of freedom in the primitive unit cell, k is the Boltzmann constant, T is temperature, and the other terms are defined above. These calculations use the same exchange-correlation functional and an energy cutoff as our total energy calculations. The number of k-points is chosen so that the density of k-points in k-space is approximately equal to the mesh used for our total energy calculations.

2.3   Methods to calculate hydrogen solubility

In this section, we show how to describe the solubility of hydrogen in metals, from first-principles calculations. Hydrogen dissolves in metal alloys by dissociative absorption of molecular H_2. This can be written as

$$H_2\,(g) \leftrightarrow 2H(a). \tag{2.5}$$

Hydrogen atoms dissolved in a metal alloy are in equilibrium with gaseous H_2 in the neighboring gas phase having a well defined partial pressure. At low concentrations of atomic hydrogen, Sieverts' law defines the solubility:[31]

$$c = K_s\sqrt{P_{H_2}}\,, \tag{2.6}$$

where K_s is the Sieverts' constant. Kamakoti and Sholl developed a theoretical model to predict hydrogen solubility in both pure Pd and disordered alloys.[32] Their Sieverts' constant for an individual site, $K_{s,i}$, with known binding energy can be expressed as[32, 33]

$$K_{s,i} = \exp\left(\frac{-E_b - 1.5hv_H + 0.25hv_{H_2}}{kT}\right)\frac{1}{\sqrt{\alpha}}\frac{\sqrt{1-\exp\left(-hv_{H_2}/2kT\right)}}{\prod_{i=1}^{3}(1-\exp\left(-hv_{H,i}/kT\right))^3}\,, \tag{2.7}$$

$$\alpha = \left(\frac{2\pi mkT}{h^2}\right)^{1.5}\frac{8\pi^2 I(kT)^2}{\sigma h^2}\,, \tag{2.8}$$

where h is Planck's constant, I is the molecular moment of inertia, m is the molecular mass of H_2, σ is the symmetry number for the molecule, v_{H_2} is the vibrational frequency of the molecule, and D_E is the classical dissociation energy of gaseous H_2. The vibrational degrees of freedom are treated as harmonic. The known quantities, such as molecular mass (m), vibrational frequency (v) of the molecule, molecular moment of inertia (I), and symmetry number (σ) for H_2 are listed in table 2.1.

Table 2.1: The molecular mass, vibrational frequency, molecular moment of inertia, and symmetry number for H_2.[34,35]

	Value	unit
m	3.32×10^{-27}	kg
v_{H_2}	6.48×10^{-13}	s^{-1}
I	4.67×10^{-48}	$kg \cdot m^2$
σ	2	unitless

Equations (2.7) and (2.8) provide the hydrogen solubility at one interstitial site with binding energy, E_b and vibrational frequency of H, v_H. The net Sieverts' constant for the material, K_s, is found by summing $K_{s,i}$ over the all possible individual sites in the bulk material:

$$K_s = \sum K_{s,i} . \tag{2.9}$$

2.4   Methods to calculate hydrogen diffusivity

In FCC metals, there are two distinct kinds of interstitial sites, octahedral (O) and tetrahedral (T) for hydrogen occupation.[36] At elevated temperatures, hydrogen diffuses in FCC metals via a succession of discrete hops over the energy barriers that exist between adjacent O site and T site through transition state, TS.[37, 38] From transition rate theory, the hopping rate (k_{ot}) for hydrogen motion from O site to T site can be expressed as[39, 40]

$$k_{ot} = \frac{\prod_{n=1}^{3} f(hv_i^n/2kT)v_i^n}{\prod_{n=1}^{2} f(hv_{TS}^n/2kT)v_{TS}^n} \exp(-E_a/kT) , \tag{2.10}$$

where $f(x) = \sinh(x)/x$.

This model provides the local hopping rates of hydrogen atoms. However, this is not sufficient to explain the net diffusivity of hydrogen at the interstitial site in the bulk of disordered alloys. For disordered alloys, different atoms in the material are randomly distributed in the lattice. To obtain the net hydrogen diffusivity, local hopping rates are associated with the long range hydrogen transport within the bulk. A Kinetic Monte Carlo simulation (KMC) describing dynamics of hydrogen moving on a lattice is utilized to describe hydrogen atom in random walk throughout standard lattice for disordered materials. This approach is defined in the next section.

2.4.1 **Kinetic Monte Carlo (KMC) simulations**

Kinetic Monte Carlo (KMC) simulations are performed to obtain the diffusivity of hydrogen in disordered systems. To predict hydrogen diffusivity, it is necessary to consider the effects of both localized hopping rates and long range hydrogen transport. It is appropriate to model stochastic systems by a sequence of discrete hops with known rates. The short-time dynamics are replaced by discrete hops in a lattice. We use the following KMC algorithm to predict the time evolution of non-interacting hydrogen atoms:[15, 31, 41]

1. Let a simulation volume of an alloy consist of randomly arranged atoms with the desired composition.

2. Define the fastest hopping rate within all possible hops in the volume to be k_{fast}.

3. Randomly place the N_H hydrogen atoms within the volume.

4. At each time step, randomly select a hydrogen atom from the simulation volume. Then randomly choose a move direction.

5. Hydrogen atom hops are accepted based on probability.

6. Regardless of the success of the attempted hop, increment time by $\Delta t = 1/N_d N_H k_{fast}$, where N_d is number of possible hopping directions for hydrogen.

2.5   References

1.   Sholl, D. S., Steckel, J. A., Density Functional Theory: A Practical Introduction (Wiley, Hoboken, NJ, 2009).
2.   C. Fiolhais, F. N., and M. A. L. Marques, A Primer in Density Functional Theory (Spinger-Verlag, Berlin, 2003).
3.   Hohenberg, P., Kohn, W., *Phys. Rev.* **1964**, 136, B864.
4.   Kohn, W., Sham, L. J., *Phys. Rev.* **1965**, 140, 1133-1137.
5.   Kresse, G., Furthmüller, J., *Phys. Rev. B* **1996**, 54, 11169.
6.   Kresse, G., Hafner, J., *Phys. Rev. B* **1993,** 47, 558.
7.   Kresse, G., Hafner, J., *J. Phys.: Condens. Matter* **1994**, 6, 8245-8257.
8.   Vanderbilt, D., *Phys. Rev. B* **1990**, 41, 7892-7895.
9.   Kresse, G., Joubert, D., *Phys. Rev. B* **1999**, 59, 1758.
10.   Blochl, P. E., *Physical Review B* **1994**, 50, 17953-17979.
11.   Perdew, J. P., Chevary, J. A., Vosko, S. H., Jackson, K. A., Pederson, M. R., Singh, D. J., Fiolhais, C., *Phys. Rev. B* **1992**, 46, 6671.
12.   Perdew, J. P., Burke, K., Ernzerhof, M., *Phys. Rev. Lett.* **1996**, 77, 3865-3868.
13.   Perdew, J. P., Burke, K., Ernzerhof, M., *Phys. Rev. Lett.* **1997**, 78, 1396-1396.
14.   Greeley, J., Mavrikakis, *J. Phys. Chem. B* **2005**, 109, 3460-3471.
15.   Kamakoti, P., Sholl, D. S., *Phys. Rev. B* **2005,** 71, 014301.
16.   Hao, S. Q., Sholl, D. S., *Energy Environ. Sci.* **2008,** 1, 175-183.
17.   Hao, S. Q., Widom, M., Sholl, D. S., *J. Phys.: Condens. Matter* **2009**, 21, 11.
18.   Kumar, A., Fennie, C. J., Rabe, K. M., *Physical Review B* **2012**, 86, 184429.
19.   Lee, J. H., Fang, L., Vlahos, E., Ke, X. L., Jung, Y. W., Kourkoutis, L. F., Kim, J. W., Ryan, P. J., Heeg, T., Roeckerath, M., Goian, V., Bernhagen, M., Uecker, R., Hammel, P. C., Rabe, K. M., Kamba, S., Schubert, J., Freeland, J. W., Muller, D. A., Fennie, C. J., Schiffer, P., Gopalan, V., Johnston-Halperin, E., Schlom, D. G., *Nature* **2010**, 466, 954.
20.   Lee, J. H., Fang, L., Vlahos, E., Ke, X. L., Jung, Y. W., Kourkoutis, L. F., Kim, J. W., Ryan, P. J., Heeg, T., Roeckerath, M., Goian, V., Bernhagen, M., Uecker, R., Hammel, P. C., Rabe, K. M., Kamba, S., Schubert, J., Freeland, J. W., Muller, D. A., Fennie, C. J., Schiffer, P., Gopalan, V., Johnston-Halperin, E., Schlom, D. G., *Nature* **2011**, 476, 114.
21.   Kamba, S., Goian, V., Orlita, M., Nuzhnyy, D., Lee, J. H., Schlom, D. G., Rushchanskii, K. Z., Lezaic, M., Birol, T., Fennie, C. J., Gemeiner, P., Dkhil, B., Bovtun, V., Kempa, M., Hlinka, J., Petzelt, J., *Phys. Rev. B* **2012**, 85, 094435.
22.   Bhatia, B., Sholl, D. S., *Phys. Rev. B* **2005**, 72, 224302.
23.   Jain, A., Hautier, G., Moore, C., Kang, B., Lee, J., Chen, H. L., Twu, N., Ceder, G., *J. Electrochem. Soc.* **2012**, 159, A622-A633.
24.   Alapati, S. V., Johnson, J. K., Sholl, D. S., *Phys. Chem. Chem. Phys.* **2007**, 9, 1438-1452.
25.   Alapati, S. V., Johnson, J. K., Sholl, D. S., *J. Phys. Chem. C* **2007**, 111, 1584-1591.
26.   Alapati, S. V., Johnson, J. K., Sholl, D. S., *J. Phys. Chem. C* **2008**, 112, 5258-5262.
27.   Sun, R. S., Chan, M. K. Y., Ceder, G., *Phys. Rev. B* **2011**, 83, 235311.

28.   Parlinski, K. Software PHONON, 2005.
29.   Ackland, G. J., *J. Phys.: Condens. Matter* **2002**, 14, 2975.
30.   Sternik, M., Parlinski, K., *J. Chem. Phys.* **2005**, 123, 204708.
31.   Kamakoti, P., Sholl, D. S., *J. Membr. Sci.* **2003,** 225, 145-154.
32.   Kamakoti, P., Morreale, B. D., Ciocco, M. V., Howard, B. H., Killmeyer, R. P., Cugini, A. V., Sholl, D. S., *Science* **2005**, 307, 569-573.
33.   McQuarrie, D. A., Statistical Mechanics. (University Science Books, Sausalito, California, 2000).
34.   Kuhn, H., Försterling, H. D., Waldeck, D. H., Principles of Physical Chemistry (John Wiley & Sons, Chicester , 2009).
35.   Mattera, L., Musenich, R., Salvo, C., Terren, S., *Faraday Discuss. Chem. Soc.* **1985**, 80, 115.
36.   Mittemeijer, E. J., Fundamentals of materials science (Springer-Verlag, Berlin Heidelberg, 2010).
37.   Barlag, H., Opara, L., Zuchner, H., *J. Alloys Compd.* **2002**, 330, 434.
38.   Fujita, S., Garcia, A., *J. Phys. Chem. Solids* **1991**, 52, 351.
39.   Kirchheim, R., Mclellan, R. B., *Acta Mater.* **1980**, 28, 1549-1554.
40.   Katz, L., Guinan, M., Borg, R. J., *Phys. Rev. B* **1971**, 4, 330-341.
41.   Semidey-Flecha, L., Sholl, D. S., *J. Chem. Phys.* **2008,** 128, 144701.

CHAPTER 3

METAL MEMBRANES IN HYDROGEN PURIFICATION

3.1 Introduction

Hydrogen is an abundant elementary resource with huge energy capacity.[1] There is no pure hydrogen in nature. Two commonly employed processes for hydrogen production are water electrolysis and extraction from fossil fuels. Since water splitting is energy intensive, hydrogen is mostly produced by steam reforming or partial oxidation of hydrocarbons.[2, 3] The purification of hydrogen with mixed gas species is important if hydrogen is obtained from fossil fuels.[4, 5]

Pd-based metal membranes have been attractive due to their perfect selectivity for H_2.[6] However, pure Pd membranes are susceptible to H_2-induced embrittlement at temperatures below about 300˚C, and may suffer from sulfur poisoning.[7, 8] Metal alloys may provide membranes that have improved performance. Pd has been considered the primary material for binary alloy membranes with elements such as Ag, Au, B, Ce, Cu, Fe, Ni, Pt, Rh, or Y, among others, as additive metal atoms.[5] PdAg, PdAu, or PdCu alloys were shown to decrease embrittlement[9], and PdCu alloys were helpful to improve the resistance to sulfur poisoning.[10-12]

In this chapter, we use computational methods to comprehensively calculate the H_2 permeability of *all* Pd-rich FCC binary alloys with the aim of finding alloys with higher H_2 permeability than pure Pd. We restrict our attention to substitutionally disordered FCC alloys with composition $Pd_{96}M_4$ (in at.%), where M is an additive metal atom such as Ag, Al, Au, Bi, Cd, Ce, Co, Cr, Cu, Dy, Er, Eu, Fe, Ga, Gd, Hf, Ho, In, Ir,

Li, Lu, Mg, Mn, Mo, Na, Nb, Ni, Os, Pb, Pt, Re, Rh, Ru, Sb, Sc, Sm, Sn, Ta, Tb, Tc, Te, Ti, Tl, Tm, V, W, Y, Yb, Zn, or Zr. This composition is convenient for the computational modeling described below and allows a wide range of alloying elements to be considered. Some elements do not form solid solutions with Pd at this composition, so this restricts the number of alloying elements we can consider. 50 elements are known to form solid solutions with Pd at this composition at ~600 K, and we examine all of these elements.[13]

Either hydrogen flux or permeability can describe a membrane's hydrogen transport performance. The H flux through a membrane is obtained from Fick's first law as the product of the diffusion coefficient and the concentration gradient across the membrane.[14, 15] The rate-limiting step of hydrogen transport in thick membranes is the diffusion of hydrogen atoms through the bulk membrane.[13] The hydrogen permeability, k, via a membrane can be described as [5, 11]

$$k = \frac{JL}{(P_{feed}^{1/2} - P_{perm}^{1/2})} .$$ (3.1)

Here, P_{feed} (P_{perm}) is the H_2 pressure on the feed side (permeate side) of the membrane, J is the H_2 flux, and L is the thickness of the membrane. In many crystalline materials, the solubility of H under conditions of practical interest for high temperature separations satisfies Sieverts' law.[16] In this case the interstitial concentration, c, satisfies $c = K_s\sqrt{P_{H_2}}$, where K_s is the Sieverts' constant. When this is true, and diffusion of H through the bulk of the membrane is the rate-limiting step of the process, k is independent of the feed and permeate pressures and can be written as [17]

$$k = \frac{1}{2}DK_s ,$$ (3.2)

where D is the diffusion coefficient of interstitial H.

Quantitatively accurate methods already exist for using DFT calculations to predict H_2 permeability through individual metal alloys.[18-20] These methods use large collections of site and transition state energies for interstitial H to derive lattice models suitable for defining net solubility and diffusion rates. Unfortunately, these methods are very time consuming, with a typical treatment of one alloy requiring ~600 individual DFT calculations.[18-20] To make this approach more amenable to screening large numbers of materials, we develop simplified lattice models that are motivated by the results of previous detailed treatments of Pd alloys, yet can be parameterized with a small number of DFT calculations. Specifically, our simplified models require 12 geometry optimizations with DFT in a supercell containing 27 atoms. This approach is applied to all of the Pd alloys defined above. In this chapter we describe a simplified lattice model that is suitable for rapidly characterizing H solubility and diffusion in alloys, and show how this model can focus the search of new materials for membranes.

3.2   Calculation methods

All DFT calculations are performed with the PW91 generalized gradient approximation functional using the Vienna *ab initio* simulation package (VASP).[21, 22] The core electrons of most atoms are described by ultrasoft pseudopotentials (USPP). For the lanthanides (Ce, Sm, Eu, Gd, Tb, Dy, Ho, Er, Tm, Yb, and Lu) the Projector Augmented Wave method is used instead, since USPPs are unavailable for these elements. Each calculation uses a 27 atom supercell with 3×3×3 primitive FCC unit cell with periodic boundary conditions, a plane wave basis set with reciprocal space sampled with a 4×4×4 Monkhorst-Pack mesh, and an energy cutoff of 241.622 eV. Geometries are relaxed until the forces on all atoms are less than 0.03 eV/Å using a conjugate gradient method.

As shown in Figure 3.1, hydrogen can occupy either the sixfold octahedral (O) or the fourfold tetrahedral (T) interstitial sites in FCC metals. These two types of interstial sites are shown in Figure 3.1.
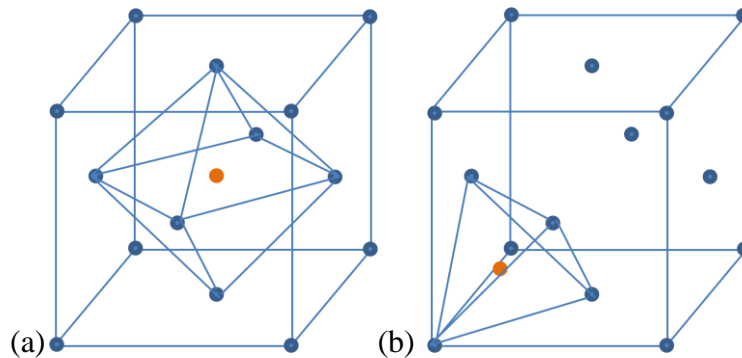
Figure 3.1: Schematic of (a) octahedral and (b) tetrahedral interstitial sites in a FCC lattice. Filled spheres signify metal atoms defining the FCC lattice, and the orange sphere represents an interstitial site occupied by hydrogen.

3.2.1 **Bulk calculations**

Lattice constants for each metal system are optimized using DFT in the absence of hydrogen. To obtain the optimized lattice constants, supercells containing 26 Pd atoms and 1 atom of the additive metal species are used. Vegard's law provides an approximate way to predict the lattice constant of an alloy. The lattice constant is a linearly weighted sum of the lattice constants of each metal comprising the alloy based on Vegard's law. Vegard's law predicts the lattice constant as[23]

$$a_{PdM} = x_{Pd}a_{Pd} + (1 - x_{Pd})a_M, \tag{3.3}$$

where a_{PdM}, a_{Pd} , and a_M are the lattice constants for the FCC alloy, pure Pd, and pure additive metal atom M in the material of interest, respectively, and x_{Pd} is the atomic composition of Pd. This lattice constant, predicted by Vegard's law, is employed as an initial lattice constant in DFT calculations to find the DFT optimized lattice constant. In DFT calculations, we allow all the metal atoms to relax as the cell volume varies.

Table 3.1: DFT optimized lattice constants for Pd-rich alloys.

System	DFT Calculated LC (Å)	System	DFT Calculated LC (Å)
$Pd_{96}Co_4$	3.947	$Pd_{96}In_4$	3.965
$Pd_{96}Cr_4$	3.948	$Pd_{96}Lu_4$	3.965
$Pd_{96}Cu_4$	3.950	$Pd_{96}Na_4$	3.965
$Pd_{96}Li_4$	3.950	$Pd_{96}Yb_4$	3.965
$Pd_{96}Mn_4$	3.950	$Pd_{96}Ag_4$	3.966
$Pd_{96}V_4$	3.950	$Pd_{96}Au_4$	3.968
$Pd_{96}Fe_4$	3.952	$Pd_{96}Cd_4$	3.969
$Pd_{96}Ga_4$	3.952	$Pd_{96}Sc_4$	3.969
$Pd_{96}Ni_4$	3.952	$Pd_{96}Sn_4$	3.969
$Pd_{96}Al_4$	3.953	$Pd_{96}Zr_4$	3.970
$Pd_{96}Ir_4$	3.956	$Pd_{96}Sb_4$	3.974
$Pd_{96}Tc_4$	3.956	$Pd_{96}Ce_4$	3.978
$Pd_{96}Ti_4$	3.956	$Pd_{96}Dy_4$	3.978
$Pd_{96}Zn_4$	3.956	$Pd_{96}Er_4$	3.978
$Pd_{96}Os_4$	3.957	$Pd_{96}Gd_4$	3.978
$Pd_{96}Re_4$	3.957	$Pd_{96}Ho_4$	3.978
$Pd_{96}W_4$	3.957	$Pd_{96}Pb_4$	3.978
$Pd_{96}Mo_4$	3.959	$Pd_{96}Sm_4$	3.978
$Pd_{96}Pt_4$	3.959	$Pd_{96}Tb_4$	3.978
$Pd_{96}Mg_4$	3.960	$Pd_{96}Te_4$	3.978
$Pd_{96}Rh_4$	3.960	$Pd_{96}Tl_4$	3.978
$Pd_{96}Ta_4$	3.961	$Pd_{96}Tm_4$	3.978
$Pd_{96}Nb_4$	3.962	$Pd_{96}Eu_4$	3.979
$Pd_{96}Ru_4$	3.963	$Pd_{96}Bi_4$	3.983
$Pd_{96}Hf_4$	3.965	$Pd_{96}Y_4$	3.983

3.2.2   DFT-based modeling of crystalline metal membranes

DFT calculations can give accurate information about the energies of systems with small numbers of atoms (10s-100s of atoms). It is therefore critical when using DFT calculations to describe metal membranes, that these calculations be combined with a

coarse-graining approach that leads to a meaningful description of macroscopic permeation. Below, we outline the ideas required to achieve this goal.

For a crystalline metal material, it is not difficult to locate the interstitial sites that can be occupied by H. The binding energy of H in each site is defined by[10]

$$E_b = E_{host/H} - E_{host} - \frac{1}{2}E_{H_2} + E^{ZP}_{host/H} - \frac{1}{2}E^{ZP}_{H_2} , \qquad (3.4)$$

where E_{host} ($E_{host/H}$) is the DFT-calculated energy of the system without (with) atomic H in the host lattice, E_{H_2} is the energy of a free H_2 molecule, and $E^{ZP}_{host/H}$ ($E^{ZP}_{H_2}$) is the zero point energy contribution from H in the host lattice (in a free molecule). Zero point energies are computed in the harmonic approximation, and for interstitial H we assume that vibrations of H are decoupled from lattice phonons.[18]

The binding energies of H at the interstitial sites are employed to calculate the net solubility of H in the alloy. As mentioned above, Sievert's law provides the hydrogen solubility at dilute hydrogen concentration.[16] This use of Sievert's law associates the interstitial concentration of atomic H with the gas phase H_2 pressure by $c = K_s\sqrt{P_{H_2}}$, where K_s is the Sieverts' constant.[24] The Sieverts' constant for an individual site with a known binding energy $K_{s,i}$ can be calculated by considering the zero point energy corrected binding energy for the interstitial site and the translational and rotational effects in the partition function of gas phase H_2.[18] The net K_s is then found by summing over the $K_{s,i}$ for each interstitial site in the material.

It is required to locate the transition states in order to model local hopping of hydrogen atoms between interstitial sites. Transition states for diffusion of H between two adjacent interstitial sites can be determined within DFT calculations by using the Nudged Elastic Band (NEB) method[25] for simple structures. The vibrational frequencies

of local minima and transition states are calculated in the harmonic approximation with similar assumptions as above. This procedure gives three real frequencies at a local energy minimum and two real frequencies and one imaginary frequency at a transition. Once a transition state between two neighbor binding sites is characterized, the H hopping rate between the sites can be computed using quantum corrected harmonic transition state theory,[26] giving

$$k_{OT} = \frac{\prod_{i=1}^{3} v_{0,i} f(h v_{0,i}/2kT)}{\prod_{j=1}^{2} v_{TS,j} f(h v_{TS,j}/2kT)} \exp\left(-E_a/kT\right) . \tag{3.5}$$

Here, $f(x) = \sinh(x)/x$, v_i is the real vibrational frequency of the binding site, v_j is the real vibrational frequency of the TS, and E_a is the activation energy for the particular hop. This expression explicitly includes contributions from each temperature dependent vibrational energy level available to the interstitial H.[18]

The model above defines the hopping rate between adjacent interstitial sites. However, this model is not sufficient to obtain the net hydrogen diffusivity in disordered alloys. To calculate this hydrogen diffusivity, we employ Kinetic Monte Carlo (KMC) simulations of hopping dynamics within a lattice model with local hopping rates. KMC is ideal to model stochastic systems defined by a succession of hops with known hopping rates.[26, 27] We simulate the hopping of many non-interacting H atoms within a simulation volume with periodic boundary conditions using an algorithm that specifies the absolute rate for each local hop. Once we observe many hydrogen hops, the mean square displacement of each H atom is calculated. Then, an Einstein expression is used to determine the diffusivity D_s [12, 28]:

$$D_s = \lim_{t \to \infty} \frac{1}{6t} < |\vec{r}(t) - \vec{r}(0)|^2 > \tag{3.6}$$

Here, $\vec{r}(t)$ is the position of the tagged particle at time t and $<...>$ represents an average over all particles of the diffusing species. It is straightforward to calculate the self diffusivity from these trajectories using Equation (3.6). If the diffusion of H in an ordered structure such as an intermetallic is being considered, an analytic method is available to describe the net diffusivity once the local hopping rates are known.[29] This theory is developed by Braun and Sholl.[30]

The methods just outlined make it possible to predict the solubility and diffusivity of H at dilute concentrations in the bulk of a metal alloy. Once these quantities are found, the net permeability of H through a membrane of the alloy may be predicted using Equation (3.2).

3.2.3   Cluster expansion methods

For binary or ternary alloys that exhibit substitutional disorder, a key challenge in using DFT calculations to describe interstitial H is that these materials have a large number of structurally different binding sites. To solve this challenge, Kamakoti and Sholl[12] first performed DFT calculations for hydrogen at diverse interstitial sites. Then, they fit the binding energies and transition state energies to a lattice model with the parameters illustrating the environment of each interstitial site. Once a lattice model of this kind is defined, the net solubility, diffusivity, and permeability of H through the bulk alloy can be calculated using a combination of statistical mechanical calculations and Kinetic Monte Carlo simulations. Because the macroscopic quantities defined by a lattice model for interstitial H can be calculated to high precision with minimal computational

effort, the quality of the agreement between the DFT data set and corresponding lattice model is the key to the success of the approach defined above.

An important difficulty with the model fitting methods used by Kamakoti and Sholl is that they do not provide a reliable way to verify the precision of the lattice model with respect to a DFT-based description of the full range of interstitial sites that can exist in a substitutionally disordered material.[10, 27] Semidey-Flecha and Sholl developed a more general model based on the concept of a cluster expansion (CE) to define the energies of interstitial H atoms in crystalline metals to overcome this difficulty.[18]

CE offers a mathematical framework based on pairs, triplets, four-body terms, etc. to describe multiple body interactions that sum together to identify the energy of a configuration.[31, 32] In the CE model, it is assumed that the total energy of a given configuration can be described by a linear combination of the energy of a special cluster as

$$E_{b\,(ZPE)} = E_0 + \sum_i J_i^{(1)} \sigma_i^{(1)} + \sum_i J_i^{(2)} \sigma_i^{(2)} + \sum_i J_i^{(3)} \sigma_i^{(3)} + \cdots, \qquad (3.7)$$

where each $J_i^{(n)}$ specifies the interaction energy of a hydrogen atom with n metal atom clusters. This infinite expansion must be truncated to determine which truncated model offers the most accurate prediction. The least squares minimization between the truncated CE and the available data is employed to determine interaction parameters $J_i^{(n)}$ once a truncation is chosen. The "leave one out (LOO)" method[33] is used to determine a truncated form of the CE. In every case, the model with the lowest LOO error is selected to define a lattice model.

In the application of the CE approach to crystalline metal alloys, there are several stages. First, a set of DFT calculations is used to define binding energies in the two

different kinds of interstitial sites such as octahedral (O) sites, tetrahedral (T) sites, along with transition states (TS) of the alloys of interest. The LOO method is then used to fit a CE model for each site to this data. This level of comparison establishes that the CE model is able to accurately fit the available DFT data. However, this comparison is only available to observe the performance of the CE model with the sites for which DFT data is presently available. Therefore, it is significant to compare the distribution of site binding energies found in DFT calculations with the distribution of energies predicted in a large volume of substitutionally random material treated with the CE models. Semidey-Flecha and Sholl have described methods to make this kind of comparison that allow CE models to be iteratively refined, if necessary, by computing additional DFT data when necessary.[19]

3.3   Model description

It is ideal to efficiently identify new promising alloys using a simplified lattice model that only require a less time and resources consuming. This chapter introduces the simplified lattice model based on the physical effects, such as lattice expansion or contraction, and the chemical effect due to the presence of an additive metal atom to interstitial sites.

Predicting H solubility and diffusivity in the FCC materials we consider requires specifying the binding energy and zero point energy at each interstitial octahedral (O) and tetrahedral (T) site and each transition state (TS) separating O and T sites. We express each of these energies as

$$E = E_{latt} + E_{chem},$$ (3.8)

where E_{latt} is the contribution due to the expansion or contraction of the lattice relative to pure Pd. This contribution is written as

$$E_{latt} = E_0 + E_1 \Delta L, \tag{3.9}$$

$$\Delta L = (L_{alloy} - L_{Pd})/L_{Pd}.$$

The parameters E_0 and E_1 are fitted to data from DFT calculations for Pd performed with a range of lattice constants, and are listed in Table 3.A.1 in Appendix 3.A. For interstitial O and T sites, the chemical contribution to the binding energy and zero point energy is written as

$$E_{chem} = E_2 n_{NN} + E_3 n_{NNN} + E_4, \tag{3.10}$$

where n_{NN} (n_{NNN}) is the number of non-Pd atoms in the nearest neighbor (next nearest neighbor) shell around the site. DFT calculations for 4 (3) DFT distinct O (T) sites are used to fit these parameters. As in earlier more rigorous models of this type[18, 19], the energies of transition states between O and T sites are defined in terms of the local coordination of the two interstitial sites. Specifically, for each TS, we define the energy and zero point energy using expressions of the form

$$E_{chem}^{TS} = E_5^{TS} n_{NN,O} + E_6^{TS} n_{NNN,O} + E_7^{TS} n_{NN,T} + E_8^{TS} n_{NNN,T} + E_9^{TS} \tag{3.11}$$

DFT calculations for 5 distinct TS are used to fit these parameters.

Once the binding energy and zero point energy for each interstitial site and transition state is defined with the models defined above, the methods of Kamakoti *et al*. are used to calculate the solubility and diffusivity of H in the limit of low interstitial H concentrations.[11, 12, 18] These calculations account for the vibrational energy levels available to interstitial H atoms within the harmonic approximation with the assumption that H vibrations are decoupled from lattice phonons. Site to site hopping rates are

defined in these calculations using quantum corrected harmonic transition state theory, and net diffusion is determined from Kinetic Monte Carlo (KMC) simulations that rigorously represent the hopping rate between adjacent interstitial sites. In our KMC simulations, the simulation volume size includes $80 \times 80 \times 80$ unit cells. To thermally equilibrate the system, 5000 MC steps per H atom, are performed. Additionally, 5000 MC steps per H atom are employed (after equilibration) while collecting data on the trajectory of each atom.

A small number of alloys are treated with more detailed DFT-based models to examine the accuracy of the simplified approach described above. For these calculations, the methods described by Semidey-Flecha *et al.* are used to derive cluster expansion models for the energy and zero point energy of each interstitial site and transition state [18, 19]. This approach requires characterization of at least 297 distinct sites with DFT. The resulting models are then used to predict solubility and diffusion in the same way as described above.

3.4   Hydrogen solubility, diffusivity, and permeability in metal alloys

Once a DFT-based lattice model is derived for each alloy, the solubility of H in the Sieverts' law regime and the self diffusion coefficient, D_s, for interstitial H is calculated with rigorous methods developed previously.[11, 12, 18] We work with Pd-based binary alloys for which dilute amounts of H are present in the bulk material. This implies we can predict H solubility using Sieverts' Law.[24] In the Sieverts' regime, the number of interstitial H atoms per metal is $c = K_s \sqrt{P_{H_2}}$, where K_s is the Sieverts' constants and P_{H2}

is the external pressure of H_2. The resulting solubility and diffusivity values are shown in Figure 3.2, where each quantity is normalized using the DFT result for pure Pd.

Previous analysis of H solubility in Pd alloys has emphasized that the overall solubility involves both lattice expansion and chemical effects.[19] In pure Pd, increasing (decreasing) the lattice constant makes the binding energy of interstitial H more (less) favorable. As a result, lattice expansion relative to pure Pd due to the presence of an alloying element influences solubility of H. The results in Figure 3.2 are shown as a function of the DFT-calculated lattice constants. The DFT calculations we use are known to slightly overestimate the lattice constants of a broad range of metals.[34] The influence of lattice expansion is clear in Figure 3.2 as a correlation between solubility and lattice constant. Specific interactions of H with atoms of the alloying element, however, also have an effect. This so-called chemical effect is clear in Figure 3.2 for groups of alloying elements such as Lu, Hf, In, Yb, and Na, which have very similar alloy lattice constants but considerably different solubility for H. Many, but not all, of the alloys we examined are predicted to have higher solubility for H than pure Pd. Our predictions are consistent with available experimental data. For example, experiments have shown enhanced solubility relative to pure Pd in binary alloys with Ag, Sn, Au, Pb, and Ce,[8, 35] and this is also seen in our calculations.
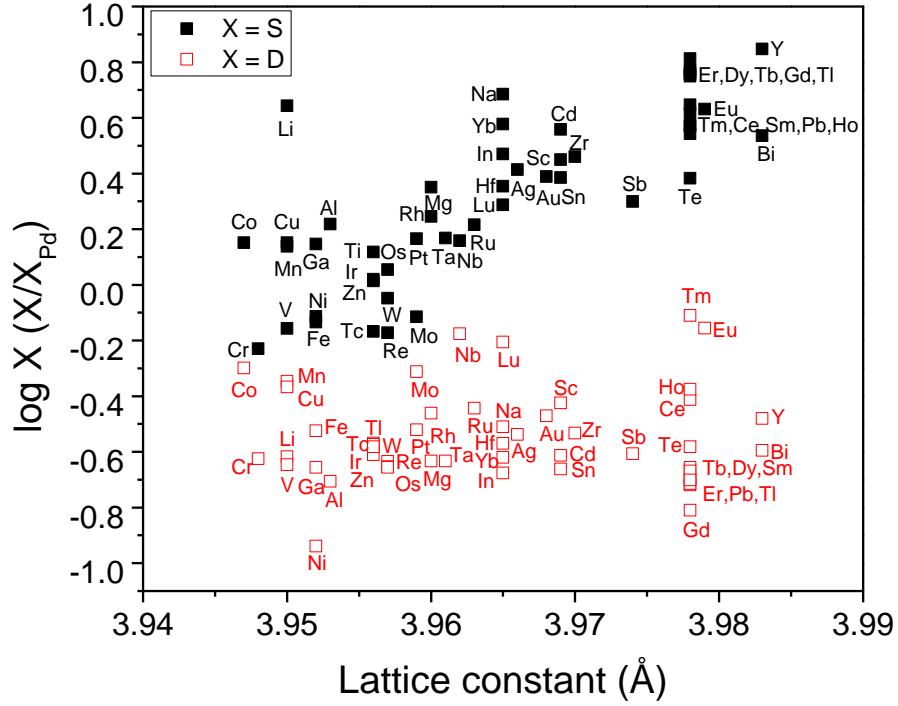
Figure 3.2: Solubility (as quantified by the Sieverts' constant) and self diffusion coefficient for interstitial H in $Pd_{96}M_4$ alloys at 600 K predicted using the methods described in the text for 50 alloys. Each data point is labeled by the alloying element, M. Each quantity is normalized by the DFT-calculated value for pure Pd at the same conditions and is shown as a function of the DFT-calculated lattice constant of the alloy. The dashed line indicates where log X = 0.

Table 3.2: Solubility, self diffusion coefficient, and permeability for interstitial H in $Pd_{96}M_4$ alloys at 600 K for 50 alloys. Each quantity is normalized by the value for pure Pd at the same conditions. Solubility and self diffusion coefficient are in log scale.

Additive metal atom	log (S/S_{Pd})	log (D/D_{Pd})	k/k_{Pd}	Additive metal atom	log (S/S_{Pd})	log (D/D_{Pd})	k/k_{Pd}
Ag	0.414	-0.538	0.752	Nb	0.158	-0.176	0.959
Al	0.218	-0.706	0.325	Ni	-0.114	-0.939	0.088
Au	0.389	-0.471	0.827	Os	0.055	-0.656	0.251
Bi	0.535	-0.595	0.872	Pb	0.572	-0.714	0.720
Cd	0.559	-0.613	0.883	Pt	0.165	-0.521	0.440
Ce	0.617	-0.412	1.600	Re	-0.173	-0.654	0.149
Co	0.151	-0.299	0.711	Rh	0.245	-0.461	0.608
Cr	-0.230	-0.625	0.139	Ru	0.216	-0.444	0.592
Cu	0.151	-0.367	0.609	Sb	0.300	-0.607	0.493
Dy	0.772	-0.670	1.270	Sc	0.450	-0.425	1.060
Er	0.813	-0.701	1.290	Sm	0.573	-0.697	0.751
Eu	0.631	-0.156	2.990	Sn	0.385	-0.662	0.529
Fe	-0.135	-0.524	0.219	Ta	0.168	-0.633	0.343
Ga	0.147	-0.656	0.310	Tb	0.764	-0.656	1.280
Gd	0.757	-0.810	0.885	Tc	-0.168	-0.573	0.181
Hf	0.354	-0.570	0.608	Te	0.382	-0.582	0.632
Ho	0.542	-0.376	1.470	Ti	0.118	-0.569	0.354
In	0.470	-0.676	0.623	Tl	0.749	-0.719	1.070
Ir	0.020	-0.582	0.274	Tm	0.646	-0.110	3.440
Li	0.643	-0.618	1.060	V	-0.157	-0.646	0.158
Lu	0.287	-0.206	1.210	W	-0.048	-0.635	0.208
Mg	0.351	-0.633	0.522	Y	0.847	-0.480	2.330
Mn	0.138	-0.347	0.618	Yb	0.577	-0.620	0.906
Mo	-0.115	-0.312	0.374	Zn	0.014	-0.611	0.253
Na	0.685	-0.510	1.500	Zr	0.460	-0.533	0.845

A striking observation from Figure 3.2 is that every alloy we consider is predicted to show slower diffusion for H than pure Pd. The strength of this effect varies from examples where the reduction in diffusivity is slight (e.g. Nb and Tm) to cases where even the small amount (4 at %) of the alloying element we consider reduces the H diffusivity by almost an order of magnitude. One simplistic description of H diffusion in these alloys is that diffusion is reduced by the existence of highly favorable sites for H

associated with non-Pd atoms. If trap sites like this exist, they enhance H solubility but depress H diffusion. Our solubility and diffusion data are plotted together in Figure 3.3. No clear correlation exists between these two quantities, implying that the simplistic description outlined above cannot fully account for our results. This is a useful observation because, as we discuss below, the permeability of an alloy is the product of H solubility and diffusivity. The lack of correlation between these quantities means that even though all alloys are predicted to have lower diffusivity than pure Pd, there are materials that have high solubility for which the decrease in diffusivity relative to pure Pd is small.
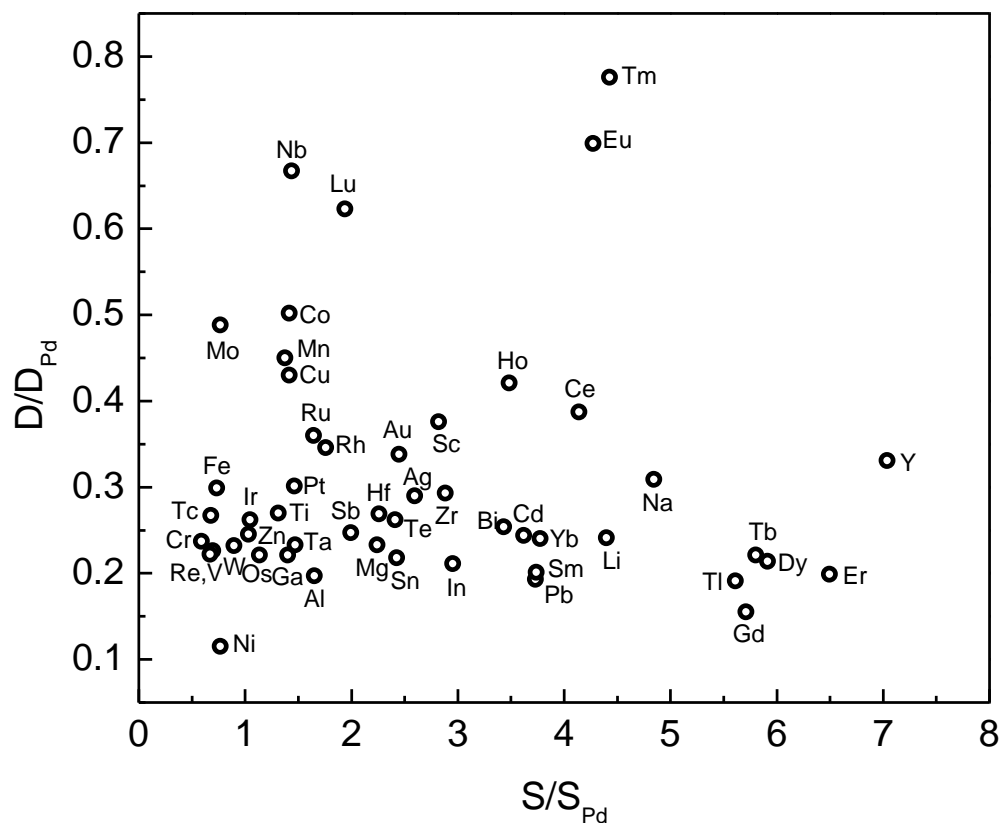
Figure 3.3: Solubility and self diffusion coefficient for interstitial H in $Pd_{96}M_4$ alloys at 600 K for 50 alloys. Each quantity is normalized by the value for pure Pd at the same conditions.

The predicted permeability of each alloy we examine is shown in Figure 3.4. The majority of the alloys are predicted to have lower permeability than pure Pd. In some cases, the differences from pure Pd are large. For $Pd_{96}Ni_4$, for example, our calculations predict a permeability that is 91% lower than pure Pd. This is in reasonable agreement with experimental data for $Pd_{90}Ni_{10}$, which reported a permeability 82% lower than pure Pd at T = 623 K.[36] A number of alloys, however, are predicted to have permeability larger than pure Pd. Previous experiments have shown enhanced permeability relative to Pd in binary alloys with Y and Ce.[37, 38] PdY films with composition similar to the

composition we consider have been reported to have a permeability ~4.5 times larger than pure Pd at 573-623 K.[37] Our calculations predict a more moderate enhancement in permeability for PdY, a factor of 2.33 at 600 K.
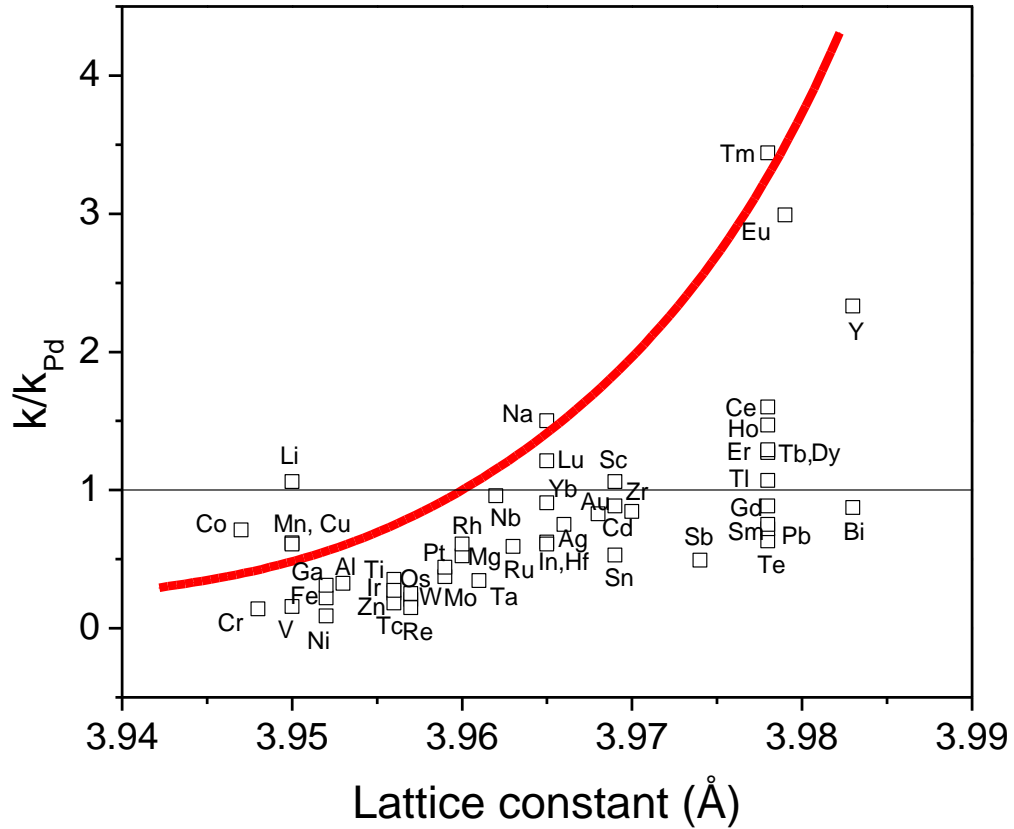
Figure 3.4: Permeability of $Pd_{96}M_4$ alloys at 600 K as predicted by the DFT-based methods described in the text as a function of the DFT-calculated alloy lattice constants. Each value is normalized by the result for pure Pd. The solid curve shows the permeability for pure Pd as a function of lattice expansion/contraction.

Figure 3.4 also shows the permeability that results from simply compressing or expanding the lattice constant of pure Pd (as calculated using our DFT-based models); we refer to this as stretched Pd. In this instance, expanding the lattice constant increases both solubility and diffusivity, leading to higher permeability. For almost all alloys we

considered, the permeability of stretched Pd has higher permeability than the alloy when they are compared for the same lattice constant. This effect is particularly strong for most of the alloying components that expand the Pd lattice. Bi and Te are two examples of this outcome. Fortunately, there are some materials that do not follow this trend. $Pd_{96}Tm_4$ and $Pd_{96}Eu_4$ are both alloys that show significant lattice expansion relative to Pd and the permeability of these alloys is predicted to be similar to that of stretched Pd.

To evaluate the reliability of our results, it is important to assess the precision of the simplified lattice models that form the basis of our calculations. To do this, we select 12 alloys with a range of predicted permeabilities and develop detailed DFT-based cluster expansion models for each alloy using the methods defined by Semidey-Flecha et al.[18-20] This approach consists of several stages. First, a set of DFT calculations is used to define binding energies in the O sites, T sites, and transition states (TS) of the alloys of interest. The LOO method is then used to fit a CE models for each site to this data. One level of comparison between the DFT data and the resulting CE model is shown in Figure 3.5 (a) using data calculated for $Pd_{96}Ru_4$. It is clear from this figure that the CE models accurately capture the variation in site energies observed with DFT. A limitation of the data shown in Figure 3.5 (a) is that it only observes the performance of CE model with sites for which DFT data is currently available. We also compare the distribution of site binding energies observed in our DFT calculations with the distribution of energies predicted in a large volume of a substitutionally random material treated with the CE models. We examine random volumes containing 4000 metal atoms to collect the latter distributions. This comparison for $Pd_{96}Ru_4$ plotted using the cumulative probability for the energy of each site is shown in Figure 3.5 (b). This comparison suggests that the

37

available DFT data and CE expansion as applied to the full random material are in good agreement. The values for O, T and TS site parameters for 12 alloys were shown in Appendix 3.A.
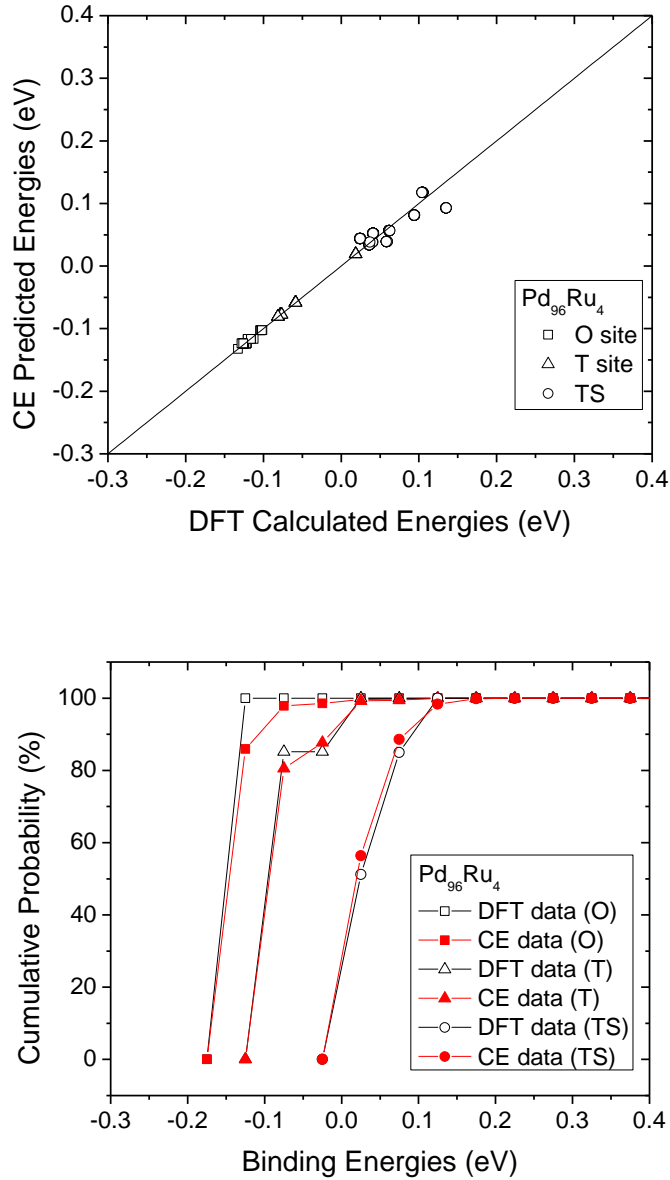
Figure 3.5: Cluster expansion results for $Pd_{96}Ru_4$. (a) A comparison of the CE model and the DFT data. (b) The energy distribution of sites observed in the DFT data and from applying the CE models to a large substitutionally random volume.

A comparison between the permeability predicted with these detailed calculations and our simplified approach is shown in Figure 3.6. In general, the agreement between the two models is good, although the simplified calculations underpredict the permeability for $Pd_{96}Ag_4$ substantially. Our results indicate that it is appropriate to broadly classify the alloys we consider as low, moderate, and high permeability when the permeability relative to Pd predicted with our simplified model is less than 0.75, between 0.75 and 1.25, and larger than 1.25, respectively. It is possible that some materials from the moderate permeability group will, like PdAg, be found to have favorable permeability when considered with more detailed models. Critically, however, it is highly unlikely that alloys from the low (high) permeability group will be reclassified as having high (low) permeability when treated with more detailed models. This means that our simplified models are a practical approach for seeking high permeability materials.
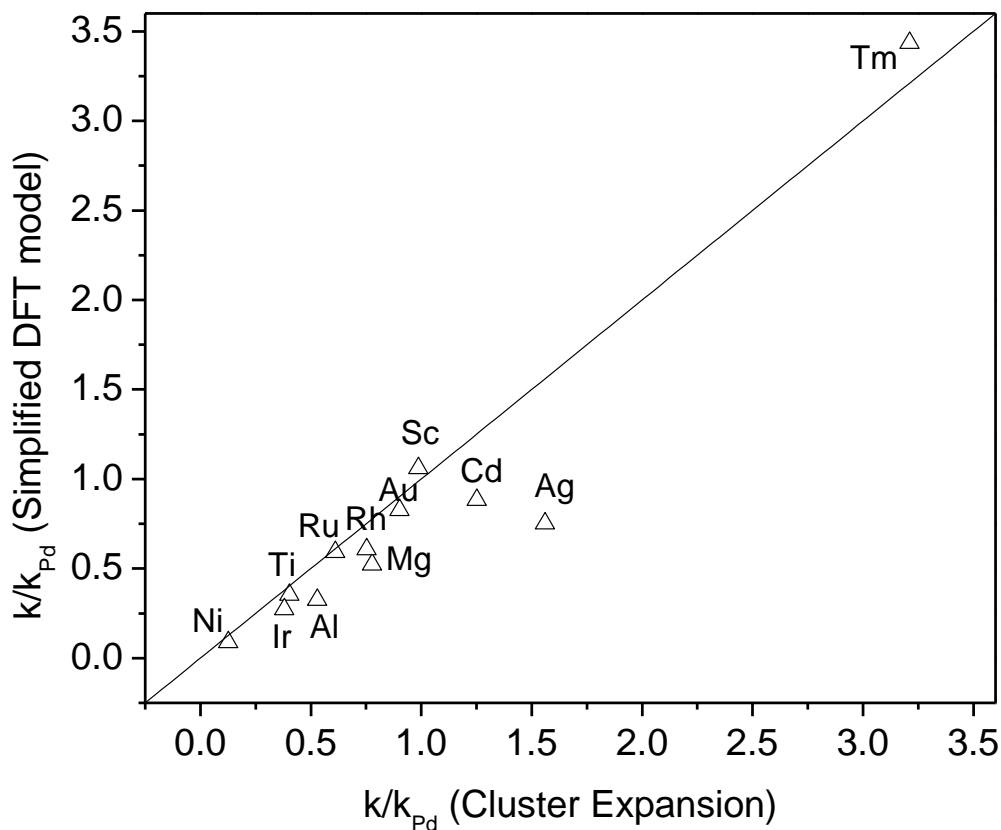
Figure 3.6: Permeability of selected $Pd_{96}M_4$ alloys at 600 K as predicted by the simplified DFT-based methods used for Figure 3.2 and Figure 3.4 and detailed DFT-derived cluster expansion models.

To test the predictions of our models, our collaborators fabricated and measured pure hydrogen permeance through PdTm foils. To the best of our knowledge, no prior experiments have been performed assessing hydrogen transport through this material, although Sakamoto *et al.* noted some time ago that PdTm alloys may have "potential applications as hydrogen diffusion membranes".[39] In the experiments, our collaborators used films with composition $Pd_{95.5}Tm_{4.5}$ at.% ($Pd_{93}Tm_7$ in wt.%). These films were quite sensitive to low temperature hydrogen embrittlement, rupturing when high pressure

hydrogen was applied at 623 or 573 K, as well as when kept under high H_2 pressures at 773 K overnight. This behavior is likely to be related to the stable hydride phase formed by pure Tm.[40] The lattice expansion associated with formation of TmH_2 is much larger than the expansion associated with formation of PdH, so even small quantities of incompletely alloyed or segregated Tm may lead to destructive embrittlement.

Hydrogen permeation measurements were successfully performed in a leak-free regime between 673 and 773 K by our collaborators.[41] The experimental data are compared to earlier results for pure Pd in Figure 3.7. Consistent with our theoretical prediction, PdTm has permeability considerably higher than pure Pd.
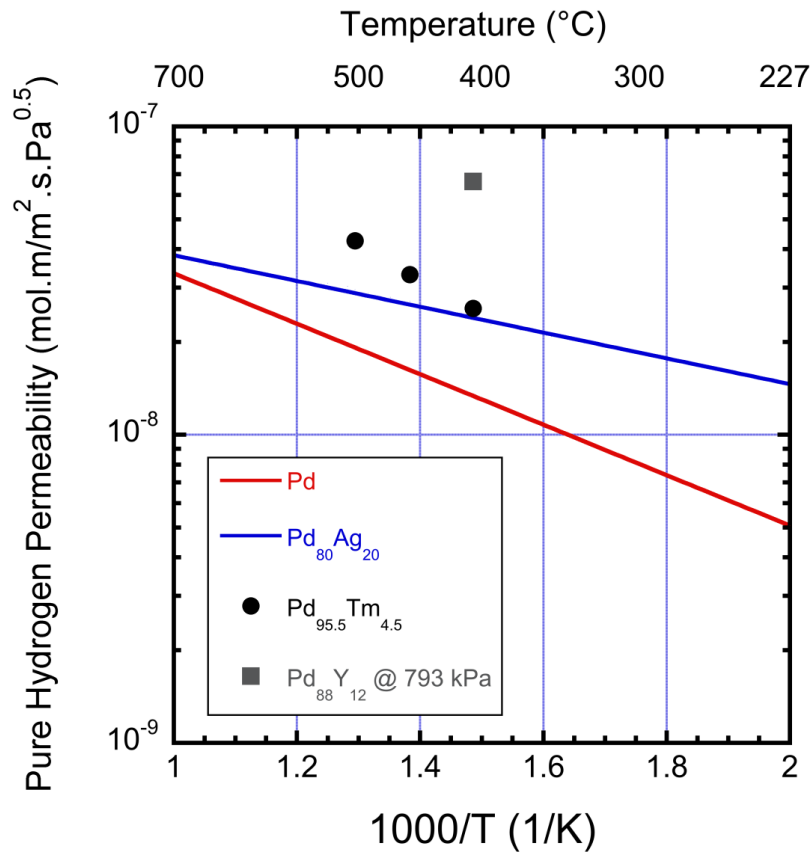
Figure 3.7: Comparison of the experimentally observed pure hydrogen permeability of $Pd_{95.5}Tm_{4.5}$ with other metals and metal alloys. Pd permeabilities are from Steward[42], $Pd_{80}Ag_{20}$ alloy data from Holleck[43], $Pd_{88}Y_{12}$ from Fort $et\ al.$[44] Alloy compositions are reported in at.%.

As mentioned above, PdAg alloys are perhaps the most widely used alloy in current practical applications of metal membranes, in part because these alloys have higher permeability than pure Pd. The experimental results for PdTm are compared to the widely used $Pd_{80}Ag_{20}$ (wt.%) alloy in Figure 3.7 and Table 3.3. In all experiments, PdTm showed higher permeability than PdAg. For example, at 773 K the permeability of PdTm foil was 44% higher than $Pd_{80}Ag_{20}$ and 111% higher than pure Pd under the same conditions. Table 3.3 also compares the predictions of our theoretical model with experimental results. Our calculations give permeability ratios in excellent agreement with experiment at 723 and 773 K, although the theory overpredicts the permeability enhancement in the alloy at 673 K. We note that our modeling does not use any experimental information apart from the knowledge that at the composition chosen PdTm forms an FCC solid solution.

Table 3.3: Experimentally measured pure hydrogen permeability of pure Pd[44], $Pd_{80}Ag_{20}$[43,] and $Pd_{95.5}Tm_{4.5}$ (this work in this chapter). Alloy compositions are shown in at.%. Permeabilities given in units of 10^{-8} mol.m/m^2.s.Pa$^{0.5}$. The ratio between the alloy permeability and the result for pure Pd is also shown. The final column shows the permeability ratio for the PdTm alloy treated in our DFT-based model.[41]

T (K)	Pd (expt.)	$Pd_{80}Ag_{20}$ (expt.)	PdAg/Pd (expt.)	$Pd_{95.5}Tm_{4.5}$ (expt.)	PdTm/Pd (expt.)	PdTm/Pd (model)
673	1.45	2.36	1.63	2.57	1.77	2.70
723	1.62	2.71	1.67	3.31	2.04	2.33
773	1.92	2.95	1.54	4.26	2.21	2.11

3.5   Conclusion

In this chapter, we use efficient DFT-based modeling to systematically examine hydrogen permeation through *all* FCC Pd-rich binary alloys. These methods make predictions about the membrane properties of alloys in far less time than is required for

experimental testing. Our work significantly expands the range of materials for which information on hydrogen permeation is available. Our models identify the small number of alloys that are known from prior experiments to have enhanced permeability relative to pure Pd, as well as several unexpected new alloys with this property. Experimental tests with one of these alloys, $Pd_{95.5}Tm_{4.5}$ (at. %), confirm that this binary alloy has higher permeability for pure hydrogen than pure Pd and the "industry standard" PdAg binary alloy. PdTm is not a panacea for the development of high flux membranes; the experiments by our collaborators showed significant challenges associated with embrittlement at moderate temperature or high H_2 pressures, and PdY alloys are known to have higher permeability.[37, 44] The modeling methods we use here are well suited to study more complex materials such as multi-component alloys[20] and ordered compounds[29], so may play a useful role in future identification of high performance membrane materials. Our calculations cannot predict other important physical properties such as the robustness of an alloy to chemical contaminants in the feed stream.[45] This issue, which is crucial in the use of membranes in practical environments, will need to be addressed through experiments. Despite this caveat, it seems likely that the modeling methods we describe will play an important role in future efforts to develop new membranes by focusing experimental attention on novel compositions that have potential to have high permeability for hydrogen.

3.6   References

1.   Schlapbach, L., Zuttel, A., *Nature* **2001,** 414, 353-358.
2.   Muradov, NZ., Veziroglu, TN., *Int. J. Hydrogen Energy* **2005**, 30, 225.
3.   Sigfusson, T. I., *Phil. Trans. R. Soc. A* **2007,** 365, 1025-1042.
4.   Steele, B. C. H., Heinzel, A., *Nature* **2001,** 414, 345-352.
5.   Paglieri, S.N., Way, J.D., *Sep. Purif. Meth.* **2002,** 31, 1-169.
6.   Su, C., Jin, T., Kuraoka, K., Matsumara, Y., Yazawa, T., *Ind. Eng. Chem. Res.* **2005**, 44, 3053.
7.   Ke, X., Kramer, G. J., *Phys. Rev. B* **2002**, 66, 184304.
8.   Kamakoti, P., Sholl, D. S., *J. Membr. Sci.* **2003**, 225, 145.
9.   Sonwane, C. G., Wilcox, J., Ma, Y. H., *J. Phys. Chem. B* **2006,** 110, 24549.
10.   Kamakoti, P., Sholl, D. S., *J. Membr. Sci.* **2003,** 225, 145-154.
11.   Kamakoti, P., Morreale, B. D., Ciocco, M. V., Howard, B. H., Killmeyer, R. P., Cugini, A. V., Sholl, D. S., *Science* **2005,** 307, 569-573.
12.   Kamakoti, P., Sholl, D. S., *Phys. Rev. B* **2005,** 71, 014301.
13.   Massalski, T.B., Murray, J.L., Bennett, L.H.; Baker, H. *Binary Alloy Phase Diagrams.* (American Society for Metals, Metals Park, OH, 1986).
14.   Fick, A., *Poggendorff's Annalen der Physik und Chemie* **1855**, 94, 59.
15.   Fick, A., *Phil. Mag. J. Sci.* **1855**, 10, 30.
16.   Ward, T. L., Dao, T., *J. Membr. Sci.* **1999,** 153, 211-231.
17.   Morreale, B. D., Ciocco, M. V., Enick, R. M., Morsi, B. I., Howard, B. H., Cugini, A. V., Rothenberger, K. S., *J. Membr. Sci.* **2003,** 212, 87-97.
18.   Semidey-Flecha, L., Sholl, D. S., *J. Chem. Phys.* **2008,** 128, 144701.
19.   Semidey-Flecha, L., Ling, C., Sholl, D. S., *J. Membr. Sci.* **2010,** 362, 384-392.
20.   Ling, C., Semidey-Flecha, L., Sholl, D. S., *J. Membr. Sci.* **2011,** 371, 189-196.
21.   Kresse, G., Furthmuller, *Comput. Mater. Sci.* **1996,** 6, 15-50.
22.   Kresse, G., Hafner, J., *Phys. Rev. B* **1993,** 47, 558.
23.   Denton, A. R., Ashcroft, N. W., *Phys. Rev. A* **1991,** 43, 3161-3164.
24.   Morreale, B. D., Ciocco, M. V., Howard, B. H., Killmeyer, R. P., Cugini, A., Enick, R. M., *J. Membr. Sci.* **2004,** 241, 219-224.
25.   Henkelman, G., Uberuaga, B. P., Jonsson, H., *J. Chem. Phys.* **2000,** 113, 9901-9904.
26.   Kamakoti, P., Sholl, D. S., *J. Membr. Sci.* **2006,** 279, 94-99.
27.   Kamakoti, P., Sholl, D. S., *Phys. Rev. B* **2005,** 71, 014301.
28.   M. P. Allen, D. J. T., *Computer Simulation of Liquids*. Claredon Press: Oxford, 1987.
29.   Ling, C., Sholl, D. S., *J. Membr. Sci.* **2009,** 329, 153-159.
30.   Braun, O. M., Sholl, C. A., *Phys. Rev. B* **1998,** 58, 14870-14879.
31.   Sluiter, M. H. F., Kawazoe, Y., *Phys. Rev. B* **2005,** 71, 012105.
32.   Seko, A., Yuge, K., Oba, F., Kuwabara, A., Tanaka, I., Yamamoto, T., *Phys. Rev. B* **2006,** 73, 094116.
33.   Drautz, R., Diaz-Ortiz, A., *Phys. Rev. B* **2006,** 73, 224207.
34.   Milman, V., Winkler, B., White, J. A., Pickard, C. J., Payne, M. C., Akhmatskaya, E. V., Nobes, R. H., *Int. J. Quantum Chem.* **2000,** 77, 895-910.

35. Brodowsk.H, Poeschel, E., *Zeitschrift Fur Physikalische Chemie-Frankfurt* **1965,** 44, 143.
36. Knapton, A. G., *Platinum Met. Rev.* **1977,** 21, 44-50.
37. Burkhanov, G. S., Gorina, N. B., Kolchugina, N. B., Roshan, N. R., Slovetsky, D. I., Chistov, E. M., *Platinum Met. Rev.* **2011,** 55, 3-12.
38. Grashoff, G. J. P., C. E., Corti, C. W., *Platinum Met. Rev.* **1983,** 27, 157–169.
39. Sakamoto, Y. C., F. L., Furukawa, M., Mine, K, *J. Less-Common Met.* **1990,** 159, 191-198.
40. Subramian, P.R., Villars, P., Okamoto, H., Cenzual, K. *H-Tm Phase Diagram.* (American Society for Metals, Materials Park, OH, 2006).
41. Kang, S. G., Coulter, K. E., Gade, S. K., Way, J. D., Sholl, D. S., *J. Phys. Chem. Lett.* **2011,** 2, 3040-3044.
42. Steward, S.A. *Review of Hydrogen Isotope Permeability Through Materials.* Lawrence Livermore National Laboratory UCRL-53441, August 15, **1983**.
43. Holleck, G. L., *J. Phys. Chem.* **1970,** 74, 503–511.
44. Fort, D. F., J. P. G., Harris, I. R., *J. Less-Common Met.* **1975,** *39*, 293–308.
45. Hao, S. Q., Sholl, D. S., *Energy Environ. Sci.* **2008,** 1, 175-183.

APPENDIX 3.A

Table 3.A.1: The parameters E_0 and E_1 for E_{LC} and ZPE for the O site, T site, and TS of pure bulk Pd as the lattice is varied from 3.9204 Å – 3.9996 Å.

	E_0 (eV)	E_1 (eV)
O site E_{LC}	-0.1399	-8.2093
O site ZPE_O	0.10067	-0.8
T site E_{LC}	-0.0843	-12.5547
T site ZPE_T	0.1827	-0.8
TS site E_{LC}	0.04	-12.8908
TS site ZPE_{TS}	0.1645	-0.8

Table 3.A.2: List of parameters used to describe the DFT calculated O sites in our FCC Pd based alloys. All parameters were normalized, or divided by either the shell number or the distance of the interaction. L represents the lattice constant in Å. Atom spacing is for the ideal FCC structures.[18]

Parameter ID #:	Description
1	Number of Pd atoms in the $2 \times N$ shell normalized by 2
2	Number of Pd atoms in the $3 \times N$ shell normalized by 3
3	Number of Cu (M in the case of binary alloys) atoms in the $2 \times N$ shell normalized by 2
4	Number of Cu (M in the case of binary alloys) atoms in the $3 \times N$ shell normalized by 3
5	Number of M (in the ternary alloys) atoms in the $2 \times N$ shell normalized by 2
6	Number of M (in the ternary alloys) atoms in the $3 \times N$ shell normalized by 3
7	2 body interactions between metal atoms separated by $L/\sqrt{2}$ in the $2 \times N$ shell normalized by $L/\sqrt{2}$
8	2 body interactions between metal atoms separated by L in the $2 \times N$ shell normalized by L
9	2 body interactions between metal atoms separated by L in the $3 \times N$ shell normalized by L
10	2 body interactions between metal atoms separated by $\sqrt{2}L$ in the $3 \times N$ shell normalized by $\sqrt{2}L$
11	2 body interactions between metal atoms separated by $\sqrt{3}L$ in the $3 \times N$ shell normalized by $\sqrt{3}L$
12	2 body interaction between metal atoms in the $2 \times N$ shell separated by $L/\sqrt{2}$ to atoms in the $3 \times N$ shell normalized by $L/\sqrt{2}$
13	3 body interactions between metal atoms in the $2 \times N$ shell where each atom is separated by $L/\sqrt{2}$ normalized by $L/\sqrt{2}$
14	3 body interactions between metal atoms in the $3 \times N$ shell where each atom is separated by L normalized by L
15	4 body interactions between metal atoms in the $2 \times N$ shell where each atom is separated by $L/\sqrt{2}$ normalized by 2
16	4 body interactions between metal atoms in the $3 \times N$ shell where each atom is separated by $\sqrt{2}L$ normalized by 3
17	Number of Pd atoms in the $4 \times N$ shell normalized by 4
18	Number of Cu (M in binary alloys) atoms in the $4 \times N$ shell normalized by 4
19	Number of M (in ternary alloys) atoms in the $4 \times N$ shell normalized by 4
20	Number of Pd atoms in the $5 \times N$ shell normalized by 5

Table 3.A.3: List of parameters used to describe the DFT calculated T sites in our FCC Pd based alloys. All parameters were normalized, or divided by either the shell number or the distance of the interaction. L represents the lattice constant in Å. Atom spacing is for the ideal FCC structures.[18]

Parameter ID #:	Description
1	Number of Pd atoms in the $2 \times N$ shell normalized by 2
2	Number of Pd atoms in the $3 \times N$ shell normalized by 3
3	Number of Cu (M in the case of binary alloys) atoms in the $2 \times N$ shell normalized by 2
4	Number of Cu (M in the case of binary alloys) atoms in the $3 \times N$ shell normalized by 3
5	Number of M (in the ternary alloys) atoms in the $2 \times N$ shell normalized by 2
6	Number of M (in the ternary alloys) atoms in the $3 \times N$ shell normalized by 3
7	2 body interactions between metal atoms separated by $L/\sqrt{2}$ in the $2 \times N$ shell normalized by $L/\sqrt{2}$
8	2 body interactions between metal atoms separated by $L/\sqrt{2}$ in the $3 \times N$ shell normalized by $L/\sqrt{2}$
9	2 body interactions between metal atoms separated by $\sqrt{6}L/2$ in the $3 \times N$ normalized by $\sqrt{6}L/2$
10	2 body interactions between metal atoms separated by $\sqrt{2}L$ in the $3 \times N$ normalized by $\sqrt{2}L$
11	2 body interactions between metal atoms separated by $\sqrt{10}L/2$ in the $3 \times N$ shell normalized by $\sqrt{10}L/2$
12	2 body interaction between metal atoms in the $2 \times N$ shell separated by $L/\sqrt{2}$ to atoms in the $3 \times N$ shell normalized by $L/\sqrt{2}$
13	2 body interaction between metal atoms in the $2 \times N$ shell separated by L to atoms in the $3 \times N$ shell normalized by L
14	2 body interaction between metal atoms in the $2 \times N$ shell separated by $\sqrt{6}L/2$ to atoms in the $3 \times N$ shell normalized by $\sqrt{6}L/2$
15	Number of Pd atoms in the $4 \times N$ shell normalized by 4
16	Number of Cu (M in binary alloys) atoms in the $4 \times N$ shell normalized by 4
17	Number of M (in ternary alloys) atoms in the $4 \times N$ shell normalized by 4
18	2 body interactions between metal atoms separated by $L/\sqrt{2}$ in the $4 \times N$ shell normalized by $L/\sqrt{2}$
19	2 body interaction between metal atoms in the $3 \times N$ shell separated by $L/\sqrt{2}$ to atoms in the $4 \times N$ normalized by $L/\sqrt{2}$

Table 3.A.3 continued

20	2 body interaction between metal atoms in the 3×N shell separated by L to atoms in the 4×N normalized by L
21	Number of Pd atoms in the 5×N shell normalized 5
22	Number of Cu (M in binary alloys) atoms in the 5×N shell normalized by 5
23	Number of M (in ternary alloys) atoms in the 5×N shell normalized by 5
24	3 body interactions between metal atoms in the 2×N shell separated by $L/\sqrt{2}$ normalized by $L/\sqrt{2}$
25	3 body interactions between metal two metal atoms separated by $L/\sqrt{2}$ in the 2×N shell to atoms in the 3×N shell separated by $L/\sqrt{2}$ normalized by separated by L 2
26	3 body interactions between metal atoms in the 3×N shell separated by $L/\sqrt{2}$ normalized by $L/\sqrt{2}$
27	3 body interactions between two metal atoms separated by $L/\sqrt{2}$ in the 3×N shell to atoms in the 2×N shell separated by $L/\sqrt{2}$ normalized by $L/\sqrt{2}$
28	3 body interactions between two metal atoms separated by $\sqrt{6}L/2$ in the 3×N shell to atoms in the 2×N shell separated by $L/\sqrt{2}$ normalized by $\sqrt{6}L/2$
29	3 body interactions between atoms in the 4×N shell separated by $L/\sqrt{2}$ normalized by $L/\sqrt{2}$
30	3 body interactions between two metal separated by $L/\sqrt{2}$ in the 3×N shell to atoms in the 4×N shell separated by $L/\sqrt{2}$ normalized by $L/\sqrt{2}$

Table 3.A.4: O site CE coefficients for the $Pd_{96}Ag_4$, $Pd_{96}Al_4$, $Pd_{96}Au_4$, and $Pd_{96}Cd_4$ alloys. Parameters identified by numbers from 1 through 20 are described in detail in Table 3.A.2. Coefficients for the CE model for E_b are listed separately from the coefficients of the ZPE for each individual alloy. All coefficients have units of eV.

	$Pd_{96}Ag_4$		$Pd_{96}Al_4$		$Pd_{96}Au_4$		$Pd_{96}Cd_4$	
	E_b	ZPE	E_b	ZPE	E_b	ZPE	E_b	ZPE
E_0	0.2101	0.1182	0.0336	-0.0185	0.7067	0.9206	-0.0434	0.3133
1	0.1413	0.0096	0.0000	0.0000	0.3194	0.2929	0.0915	0.0797
2	0.0000	0.0000	0.0000	0.0000	0.0000	0.0000	-0.0120	0.0039
3	0.0000	0.0000	0.5119	0.2057	0.0000	-0.2296	0.0993	0.0000
4	0.0000	0.0000	0.0687	-0.0040	0.0325	0.0000	0.0000	0.0000
5	0.0000	0.0000	0.0000	0.0000	0.0000	0.0000	0.0000	0.0000
6	0.0000	0.0000	0.0000	0.0000	0.0000	0.0000	0.0000	0.0000
7	-0.0045	0.0000	-0.0150	0.0153	0.0000	0.0169	-0.0094	0.0000
8	0.0787	0.0139	0.0000	0.0000	0.1510	-0.0541	0.0000	0.0000
9	0.0000	0.0164	0.0053	-0.0021	0.0000	0.0000	0.0000	0.0000
10	0.0057	0.0000	0.0000	0.0000	0.0000	0.0000	-0.0040	0.0000
11	0.0000	0.0000	0.0000	0.0000	0.0000	0.0000	0.0000	0.0000
12	0.0008	0.0000	0.0000	0.0000	0.0000	0.0000	0.0000	0.0000
13	0.0000	0.0000	-0.0474	-0.0130	0.0000	0.0000	0.0000	0.0000
14	0.0011	0.0078	0.0000	0.0000	0.0000	0.0000	0.0000	0.0000
15	0.0000	0.0000	0.0000	0.0000	0.0000	0.0000	0.0000	0.0000
16	0.0000	0.0000	0.0000	0.0000	0.0000	0.0000	-0.0057	-0.0022
17	0.0000	0.0000	0.0000	0.0000	0.0000	0.0000	-0.0314	0.0000
18	0.0000	0.0000	0.0000	0.0000	0.0000	0.0000	0.0682	0.0128
19	0.0000	0.0000	0.0000	0.0000	0.0000	0.0000	0.0000	0.0000
20	0.0000	0.0000	0.0570	0.0007	0.0000	0.0000	0.0043	0.0000

Table 3.A.5: O site CE coefficients for the $Pd_{96}Ir_4$, $Pd_{96}Mg_4$, $Pd_{96}Ni_4$, and $Pd_{96}Rh_4$ alloys. Parameters identified by numbers from 1 through 20 are described in detail in Table 3.A.2. Coefficients for the CE model for E_b are listed separately from the coefficients of the ZPE for each individual alloy. All coefficients have units of eV.

	$Pd_{96}Ir_4$		$Pd_{96}Mg_4$		$Pd_{96}Ni_4$		$Pd_{96}Rh_4$	
	E_b	ZPE	E_b	ZPE	E_b	ZPE	E_b	ZPE
E_0	-0.0623	0.0083	0.0329	0.1847	-0.0999	0.0103	0.3801	0.0169
1	0.0000	0.0000	0.0000	0.0000	0.0518	-0.0486	0.1478	0.0610
2	0.0000	0.0000	0.0270	0.0251	0.0000	-0.0122	0.0963	0.0000
3	0.0000	0.0000	0.0000	0.0000	0.0871	0.0010	0.0000	0.0000
4	0.0348	0.0746	0.0000	0.0000	0.0000	0.0000	0.0000	0.0000
5	0.0000	0.0000	0.0000	0.0000	0.0000	0.0000	0.0000	0.0000
6	0.0000	0.0000	0.0000	0.0000	0.0000	0.0000	0.0000	0.0000
7	-0.0328	0.0243	0.0000	0.0000	0.0511	-0.0090	0.0206	0.0101
8	0.0000	0.0000	0.0000	0.0000	0.0090	-0.0129	0.0315	0.0401
9	0.0019	0.0237	0.0000	0.0000	0.0000	0.0000	0.0053	0.0000
10	0.0000	0.0000	0.0000	0.0000	0.0050	0.0000	0.0000	0.0000
11	0.0000	0.0000	0.0000	0.0000	0.0000	-0.0077	0.0000	0.0000
12	-0.0026	-0.0061	-0.0145	-0.0095	0.0019	-0.0025	0.0069	0.0000
13	-0.0181	0.0324	0.0000	0.0000	0.0252	0.0000	0.0000	0.0000
14	0.0000	0.0000	-0.0104	-0.0083	0.0000	0.0000	0.0000	0.0000
15	0.0000	0.0000	0.0000	0.0000	-0.0009	0.0025	0.0000	0.0000
16	0.0019	0.0009	0.0000	0.0000	0.0000	0.0000	0.0000	0.0000
17	0.0000	0.0000	0.0000	0.0000	0.0000	0.0000	0.0000	0.0000
18	0.0000	0.0000	0.0494	-0.0007	0.0000	0.0000	0.0000	0.0000
19	0.0000	0.0000	0.0000	0.0000	0.0000	0.0000	0.0000	0.0000
20	-0.0091	-0.0062	0.0083	0.0011	0.0000	0.0107	0.0000	0.0000

Table 3.A.6: O site CE coefficients for the $Pd_{96}Ru_4$, $Pd_{96}Sc_4$, $Pd_{96}Ti_4$, and $Pd_{96}Tm_4$ alloys. Parameters identified by numbers from 1 through 20 are described in detail in Table 3.A.2. Coefficients for the CE model for E_b are listed separately from the coefficients of the ZPE for each individual alloy. All coefficients have units of eV.

	$Pd_{96}Ru_4$		$Pd_{96}Sc_4$		$Pd_{96}Ti_4$		$Pd_{96}Tm_4$	
	E_b	ZPE	E_b	ZPE	E_b	ZPE	E_b	ZPE
E_0	0.0948	0.0440	-0.0721	0.0117	-0.0549	-0.0493	0.7702	0.0952
1	0.0000	0.0000	0.0308	0.0000	0.0000	0.0000	0.1109	0.0542
2	0.0000	0.0000	0.0000	0.0000	0.0629	0.0062	0.0000	0.0213
3	0.2948	0.1543	0.0787	0.1635	0.2944	0.2459	0.0000	0.0000
4	0.1179	0.0855	0.1241	0.0000	0.0000	0.0000	0.0000	0.0000
5	0.0000	0.0000	0.0000	0.0000	0.0000	0.0000	0.0000	0.0000
6	0.0000	0.0000	0.0000	0.0000	0.0000	0.0000	0.0000	0.0000
7	0.0000	0.0000	0.0000	0.0000	0.0083	0.0186	-0.0065	0.0000
8	0.1743	0.1475	0.0000	0.0000	0.0000	0.0000	-0.0300	-0.0350
9	0.0087	0.0156	-0.0993	0.0122	0.0000	0.0000	-0.0161	0.0000
10	0.0000	0.0000	-0.0069	0.0000	0.0000	0.0000	0.0000	0.0000
11	0.0020	0.0450	0.0000	0.0000	0.0000	0.0000	0.0000	0.0000
12	0.0148	0.0033	0.0000	0.0000	0.0000	0.0000	0.0000	0.0000
13	0.0256	0.0068	0.0000	-0.0161	-0.0155	-0.0138	0.0000	0.0000
14	0.0000	0.0000	-0.0541	0.0077	0.0000	0.0000	0.0000	-0.0044
15	0.0000	0.0000	0.0000	0.0000	0.0000	-0.0001	0.0000	0.0000
16	0.0208	0.0072	0.0000	0.0000	0.0000	0.0000	0.0000	-0.0148
17	0.0000	0.0000	-0.0117	0.0000	0.0000	0.0000	0.0886	-0.0369
18	0.0000	0.0000	0.0985	0.0318	0.0665	0.0205	0.0000	0.1108
19	0.0000	0.0000	0.0000	0.0000	0.0000	0.0000	0.0000	0.0000
20	0.0217	0.0045	0.0000	0.0000	-0.0007	-0.0041	0.0000	0.0000

Table 3.A.7: T site CE coefficients for the $Pd_{96}Ag_4$, $Pd_{96}Al_4$, $Pd_{96}Au_4$, and $Pd_{96}Cd_4$ alloys. Parameters identified by numbers from 1 through 20 are described in detail in Table 3.A.3. Coefficients for the CE model for E_b are listed separately from the coefficients of the ZPE for each individual alloy. All coefficients have units of eV.

	$Pd_{96}Ag_4$		$Pd_{96}Al_4$		$Pd_{96}Au_4$		$Pd_{96}Cd_4$	
	E_b	ZPE	E_b	ZPE	E_b	ZPE	E_b	ZPE
E_0	0.5897	0.2321	0.2843	0.1955	0.8591	0.1960	0.1340	0.1896
1	0.3873	0.0228	0.0961	0.0000	0.5054	0.0100	0.0000	0.0000
2	0.0000	0.0000	0.0000	0.0000	0.0000	0.0000	0.0000	0.0000
3	0.0000	0.0000	0.0000	0.0000	0.0000	0.0000	0.0000	0.0000
4	0.0000	0.0000	0.0000	0.0000	0.0000	0.0000	0.0000	0.0000
5	0.0000	0.0000	0.0000	0.0000	0.0000	0.0000	0.0000	0.0000
6	0.0000	0.0000	0.0000	0.0000	0.0000	0.0000	0.0000	0.0000
7	0.0497	0.0041	-0.0263	0.0000	0.0086	0.0043	0.0000	0.0000
8	0.0000	0.0000	0.0226	0.0000	0.0000	0.0000	0.0000	0.0000
9	0.0000	0.0000	0.0000	0.0018	0.0000	0.0000	0.0223	0.0000
10	0.0000	0.0000	-0.0105	0.0000	0.0000	0.0000	0.0000	0.0000
11	0.0343	0.0000	0.0000	0.0000	-0.0040	0.0000	0.0000	0.0000
12	0.0000	0.0000	0.0000	0.0000	0.0000	0.0000	0.0058	0.0000
13	-0.0069	0.0000	-0.0014	0.0000	0.0260	0.0000	-0.0649	0.0000
14	-0.0112	0.0000	0.0062	-0.0089	-0.0056	0.0012	0.0000	-0.0018
15	0.0000	0.0048	0.0000	0.0000	0.0000	0.0000	0.0545	0.0000
16	0.0000	0.0000	0.0000	0.0000	0.0000	0.0000	0.0000	0.0000
17	0.0000	0.0000	0.0000	0.0000	0.0000	0.0000	0.0000	0.0000
18	0.0000	0.0000	0.0069	0.0000	0.0000	0.0000	0.0000	0.0000
19	-0.0028	0.0000	-0.0054	0.0000	-0.0005	0.0000	-0.0016	0.0000
20	-0.0050	0.0000	-0.0043	0.0000	-0.0019	-0.0013	-0.0063	0.0000
21	0.0000	0.0000	0.0000	0.0000	0.0000	0.0000	0.0000	0.0000
22	0.0000	0.0000	0.0000	0.0000	0.0000	0.0000	0.0000	0.0000
23	0.0000	0.0000	0.0000	0.0000	0.0000	0.0000	0.0000	0.0000
24	0.0000	0.0000	0.0678	0.0000	0.0000	0.0000	0.0000	0.0000
25	0.0000	0.0000	0.0000	0.0000	0.0000	0.0000	0.0000	0.0000
26	0.0000	0.0000	0.0203	0.0000	0.0000	0.0000	0.0000	0.0000
27	0.0000	0.0000	0.0088	0.0000	0.0000	0.0000	0.0000	0.0000
28	0.0000	0.0000	0.0000	0.0000	0.0000	0.0000	0.0000	0.0000
29	0.0000	0.0000	0.0000	-0.0029	0.0000	0.0000	0.0000	0.0017
30	0.0000	0.0000	0.0000	0.0000	0.0000	0.0000	0.0000	0.0000

Table 3.A.8: T site CE coefficients for the $Pd_{96}Ir_4$, $Pd_{96}Mg_4$, $Pd_{96}Ni_4$, and $Pd_{96}Rh_4$ alloys. Parameters identified by numbers from 1 through 20 are described in detail in Table 3.A.3. Coefficients for the CE model for E_b are listed separately from the coefficients of the ZPE for each individual alloy. All coefficients have units of eV.

	$Pd_{96}Ir_4$		$Pd_{96}Mg_4$		$Pd_{96}Ni_4$		$Pd_{96}Rh_4$	
	E_b	ZPE	E_b	ZPE	E_b	ZPE	E_b	ZPE
E_0	0.7376	0.1810	0.0948	0.1589	-0.4576	0.6535	0.4890	0.1835
1	0.3799	0.0000	0.0000	0.0000	-0.0632	0.2311	0.1271	0.0066
2	0.0000	0.0000	-0.0179	-0.0451	0.0000	0.0000	0.0594	0.0000
3	0.0000	0.0000	0.0000	0.0000	0.0000	-0.2412	0.0000	0.0000
4	0.0000	0.0000	0.0000	0.0000	0.0000	-0.0038	0.0000	0.0000
5	0.0000	0.0000	0.0000	0.0000	0.0000	0.0000	0.0000	0.0000
6	0.0000	0.0000	0.0000	0.0000	0.0000	0.0000	0.0000	0.0000
7	0.0000	0.0000	0.0000	0.0000	0.0054	0.0018	0.0192	0.0011
8	0.0000	0.0000	0.0123	-0.0205	0.0000	0.0000	0.0000	0.0000
9	-0.0375	0.0000	0.0000	0.0000	0.0000	-0.0003	0.0000	0.0000
10	0.0000	0.0000	0.0000	0.0000	0.0000	-0.0037	-0.0078	0.0000
11	0.0000	0.0000	0.0000	0.0000	0.0000	0.0000	0.0000	0.0000
12	0.0000	0.0000	-0.0225	-0.0267	0.0009	-0.0001	0.0023	0.0000
13	0.0000	0.0938	0.0000	0.0000	-0.0019	0.0000	0.0000	0.0000
14	0.0000	-0.1161	0.0000	0.0000	0.0000	-0.0023	0.0000	0.0000
15	0.0000	-0.0023	0.0498	-0.0020	-0.1174	0.0000	0.0545	0.0000
16	0.0000	0.0000	0.0000	0.0000	0.0000	0.0000	0.0000	0.0000
17	0.0000	0.0000	0.0000	0.0000	0.0000	0.0000	0.0000	0.0000
18	0.0000	0.0000	0.0000	0.0000	-0.0122	0.0000	0.0083	0.0011
19	0.0000	0.0000	0.0000	0.0000	-0.0039	0.0000	0.0000	0.0000
20	0.0000	0.0000	0.0000	0.0000	0.0048	0.0000	0.0050	0.0000
21	0.0000	0.0000	0.0000	0.0000	0.0000	0.0000	0.0076	-0.0026
22	0.0000	0.0000	0.0000	0.0000	0.0000	0.0000	0.0000	0.0000
23	0.0000	0.0000	0.0000	0.0000	0.0000	0.0000	0.0000	0.0000
24	0.0000	0.0000	0.0000	0.0000	0.0000	0.0000	0.0000	0.0000
25	0.0000	0.0000	0.0000	0.0000	0.0000	0.0000	0.0000	0.0000
26	0.0000	0.0000	0.0000	0.0000	0.0000	0.0000	0.0000	0.0000
27	0.0000	0.0000	-0.0010	-0.0230	0.0000	0.0000	0.0000	0.0000
28	-0.0273	0.0000	0.0000	0.0000	0.0000	0.0000	0.0000	0.0000
29	-0.0090	0.0000	0.0000	0.0000	0.0000	0.0000	0.0000	0.0000
30	0.0000	0.0000	0.0000	0.0000	0.0000	0.0000	0.0000	0.0000

Table 3.A.9: T site CE coefficients for the $Pd_{96}Ru_4$, $Pd_{96}Sc_4$, $Pd_{96}Ti_4$, and $Pd_{96}Tm_4$ alloys. Parameters identified by numbers from 1 through 20 are described in detail in Table 3.A.3. Coefficients for the CE model for E_b are listed separately from the coefficients of the ZPE for each individual alloy. All coefficients have units of eV.

	$Pd_{96}Ru_4$		$Pd_{96}Sc_4$		$Pd_{96}Ti_4$		$Pd_{96}Tm_4$	
	E_b	ZPE	E_b	ZPE	E_b	ZPE	E_b	ZPE
E_0	0.0658	0.0732	0.2383	0.1992	0.1469	0.1996	0.0487	0.2076
1	0.0000	0.0000	0.0000	0.0000	-0.0273	0.0000	0.0000	0.0000
2	-0.0162	0.0000	0.0384	0.0000	0.0000	0.0000	0.0000	0.0000
3	0.0000	0.0000	0.0000	0.0000	0.0000	0.0000	0.0000	0.0000
4	-0.1219	0.0770	0.0000	0.0000	0.0000	0.0000	0.0000	0.0000
5	0.0000	0.0000	0.0000	0.0000	0.0000	0.0000	0.0000	0.0000
6	0.0000	0.0000	0.0000	0.0000	0.0000	0.0000	0.0000	0.0000
7	0.0000	0.0185	0.0000	0.0000	-0.1064	0.0000	0.0000	0.0000
8	0.0117	0.0236	0.0000	0.0000	0.0000	0.0000	-0.0085	0.0009
9	-0.0012	0.0000	0.0135	0.0009	-0.0185	0.0000	0.0106	0.0000
10	0.0000	0.0000	0.0000	0.0000	0.0000	0.0000	0.0000	0.0000
11	-0.0548	0.0000	0.0243	0.0000	0.0000	0.0000	0.0000	0.0000
12	-0.0084	0.0000	-0.0160	0.0000	0.0000	0.0000	0.0000	0.0000
13	0.0000	0.0000	0.0000	0.0000	0.0000	0.0000	-0.0101	0.0000
14	0.0000	0.0000	-0.0296	-0.0083	0.0000	0.0000	0.0000	0.0000
15	-0.0067	0.0000	0.0200	0.0000	0.0000	0.0000	0.0000	0.0000
16	0.0000	-0.0028	0.0000	0.0000	0.0665	0.0000	0.0000	0.0000
17	0.0000	0.0000	0.0000	0.0000	0.0000	0.0000	0.0000	0.0000
18	0.0000	0.0000	0.0000	0.0000	0.0000	0.0000	0.0000	0.0000
19	0.0000	0.0000	0.0000	0.0000	0.0000	0.0000	0.0000	0.0000
20	0.0000	0.0000	0.0000	0.0000	0.0000	0.0000	0.0000	0.0000
21	0.0000	0.0000	0.0000	0.0000	0.0000	0.0000	0.0000	0.0000
22	0.0000	0.0000	0.0000	0.0000	0.0000	0.0000	0.0000	0.0000
23	0.0000	0.0000	0.0000	0.0000	0.0000	0.0000	0.0000	0.0000
24	0.0000	-0.0517	0.0000	0.0000	0.0000	0.0000	0.0547	0.0000
25	0.0000	0.0359	0.0000	0.0000	-0.0099	0.0054	0.0000	0.0000
26	0.0000	0.0000	0.0000	0.0000	0.0000	0.0000	0.0000	0.0000
27	0.0143	0.0000	0.0000	0.0000	0.0000	0.0000	0.0000	0.0000
28	0.0000	0.0000	0.0000	0.0000	0.0000	0.0000	0.0000	0.0000
29	0.0000	0.0000	0.0327	0.0007	0.0000	0.0000	0.0615	0.0000
30	0.0000	0.0000	0.0000	0.0000	0.0000	-0.0022	0.0015	0.0038

Table 3.A.10: TS site CE coefficients for the $Pd_{96}Ag_4$, $Pd_{96}Al_4$, $Pd_{96}Au_4$, and $Pd_{96}Cd_4$ alloys. O site parameter contributions identified as O 1- O 20 and T site parameter contribution identified as T 1 – T 30 as described in Table 3.A.2 and Table 3.A.3. Coefficients for the CE model for E_b are listed separately from the coefficients of the ZPE for each individual alloy. All coefficients have units of eV.

	$Pd_{96}Ag_4$		$Pd_{96}Al_4$		$Pd_{96}Au_4$		$Pd_{96}Cd_4$	
	E_b	ZPE	E_b	ZPE	E_b	ZPE	E_b	ZPE
E_0	-0.8336	0.1954	0.3728	0.1296	1.4747	0.2027	0.3664	0.1855
O 1	0.1363	0.0005	0.0000	0.0000	0.0000	-0.0044	0.0000	0.0000
O 2	0.0000	0.0000	0.0000	0.0000	0.0000	0.0000	0.0000	0.0000
O 3	0.0000	0.0000	0.0000	0.0000	0.0000	0.0000	0.0000	0.0000
O 4	0.0000	0.0000	0.0000	0.0000	0.0000	0.0000	0.0000	0.0000
O 5	0.0000	0.0000	0.0000	0.0000	0.0000	0.0000	0.0000	0.0000
O 6	0.0000	0.0000	0.0000	0.0000	0.0000	0.0000	0.0000	0.0000
O 7	0.0000	0.0000	0.0000	0.0000	0.0000	0.0000	0.0000	-0.0020
O 8	0.0000	0.0026	0.0000	0.0000	0.0000	0.0000	0.0000	0.0000
O 9	0.0000	0.0000	0.0000	0.0000	0.0000	0.0000	0.0000	-0.0002
O 10	0.0000	0.0000	0.0049	0.0010	0.0000	0.0000	0.0000	0.0000
O 11	0.0000	0.0000	0.0000	0.0000	0.0000	0.0000	0.0000	0.0000
O 12	0.0000	0.0000	0.0000	0.0000	-0.0081	0.0000	0.0000	0.0000
O 13	0.0000	0.0000	0.0312	-0.0001	0.0000	0.0000	-0.0023	0.0000
O 14	0.0000	0.0000	0.0000	0.0000	0.0000	0.0000	0.0000	0.0000
O 15	0.0000	0.0000	0.0000	0.0000	0.0000	0.0000	0.0000	0.0000
O 16	0.0000	0.0000	0.0000	0.0000	0.0000	0.0000	0.0000	0.0000
O 17	0.0939	0.0000	0.0000	0.0000	0.0000	0.0000	0.0000	0.0014
O 18	0.0000	0.0000	0.0000	0.0000	0.0000	0.0000	0.0000	0.0000
O 19	0.0000	0.0000	0.0000	0.0000	0.0000	0.0000	0.0000	0.0000
O 20	0.0000	0.0000	0.0186	-0.0080	0.0000	0.0000	0.0241	0.0000
T 1	0.0000	0.0207	0.0000	0.0000	0.4336	0.0170	0.0000	0.0000
T 2	-0.5356	0.0000	0.0000	0.0000	0.0000	0.0070	0.0000	0.0000
T 3	0.0000	0.0000	0.0000	0.0000	0.0000	0.0000	0.0000	0.0000
T 4	0.0000	0.0000	0.0000	0.0000	0.0000	0.0000	0.0000	0.0000
T 5	0.0000	0.0000	0.0000	0.0000	0.0000	0.0000	0.0000	0.0000
T 6	0.0000	0.0000	0.0000	0.0000	0.0000	0.0000	0.0000	0.0000
T 7	0.0000	0.0000	0.0000	0.0000	0.0000	0.0000	0.0000	0.0000
T 8	-0.0360	0.0000	0.0000	0.0000	0.0000	-0.0009	0.0000	0.0000
T 9	0.0000	0.0000	0.0000	0.0000	-0.0360	0.0000	0.0000	0.0000
T 10	0.0000	0.0000	0.0000	0.0000	0.0000	0.0024	0.0000	0.0000
T 11	0.0000	0.0000	0.0000	0.0000	0.0000	0.0000	0.0000	0.0000
T 12	0.0144	0.0015	0.0000	0.0000	0.0000	0.0009	0.0000	0.0000
T 13	-0.0558	0.0000	0.0000	0.0000	0.0000	0.0000	0.0000	0.0000
T 14	-0.0844	0.0000	0.0000	0.0000	0.0000	0.0022	0.0000	0.0000
T 15	-0.1223	0.0000	0.0000	0.0000	0.2455	0.0013	0.0000	0.0000
T 16	0.0000	0.0000	0.0000	0.0000	0.0000	0.0000	0.0000	0.0000
T 17	0.0000	0.0000	0.0000	0.0000	0.0000	0.0000	0.0000	0.0000
T 18	0.0000	0.0000	0.0000	0.0000	0.0000	0.0000	0.0000	0.0000
T 19	-0.0302	0.0000	0.0000	0.0000	0.0000	0.0000	0.0000	0.0000
T 20	0.0000	0.0000	0.0000	0.0000	0.0665	0.0000	0.0000	0.0000
T 21	0.0000	0.0000	0.0000	0.0000	0.0000	0.0000	0.0000	0.0000
T 22	0.0000	0.0000	0.0000	0.0000	0.0000	0.0000	0.0000	0.0000
T 23	0.0000	0.0000	0.0000	0.0000	0.0000	0.0000	0.0000	0.0000
T 24	0.0000	0.0000	0.1156	0.0026	0.0000	0.0000	0.1773	0.0000
T 25	0.0000	0.0000	0.0000	0.0000	0.0000	0.0000	0.0000	0.0000
T 26	0.0000	0.0000	0.0000	0.0000	0.0000	0.0000	0.0000	0.0000
T 27	0.0000	0.0000	0.0000	0.0000	0.0000	0.0000	0.0000	0.0008
T 28	0.0000	0.0000	0.0000	0.0000	0.0000	0.0000	0.0000	0.0000
T 29	0.0000	0.0000	0.0000	0.0000	0.0000	0.0000	0.0000	0.0000
T 30	0.0000	0.0000	0.0000	0.0000	0.0000	0.0000	0.0000	0.0000

Table 3.A.11: TS site CE coefficients for the $Pd_{96}Ir_4$, $Pd_{96}Mg_4$, $Pd_{96}Ni_4$, and $Pd_{96}Rh_4$ alloys. O site parameter contributions identified as O 1- O 20 and T site parameter contribution identified as T 1 – T 30 as described in Table 3.A.2 and Table 3.A.3. Coefficients for the CE model for E_b are listed separately from the coefficients of the ZPE for each individual alloy. All coefficients have units of eV.

	$Pd_{96}Ir_4$		$Pd_{96}Mg_4$		$Pd_{96}Ni_4$		$Pd_{96}Rh_4$	
	E_b	ZPE	E_b	ZPE	E_b	ZPE	E_b	ZPE
E_0	0.8046	0.0477	0.3035	0.1897	0.0776	-0.0987	0.7408	0.1718
O 1	0.0000	-0.0062	0.0000	0.0000	0.0000	0.0000	0.0000	-0.0028
O 2	0.0000	0.0000	0.0000	0.0000	0.0000	0.0000	0.0000	-0.0018
O 3	0.0485	0.1949	0.0000	0.0000	0.0000	0.0000	0.0000	0.0000
O 4	0.0000	0.0000	0.0000	0.0000	0.0000	0.0000	0.0000	0.0000
O 5	0.0000	0.0000	0.0000	0.0000	0.0000	0.0000	0.0000	0.0000
O 6	0.0000	0.0000	0.0000	0.0000	0.0000	0.0000	0.0000	0.0000
O 7	0.0000	0.0015	0.0000	0.0000	0.0148	0.0000	0.0058	0.0000
O 8	0.0000	0.1460	0.0000	0.0000	0.0000	0.0000	0.0000	0.0000
O 9	-0.4113	-0.0194	0.0000	0.0000	0.0000	-0.0048	0.0000	0.0000
O 10	0.0000	0.0091	0.0094	-0.0017	0.0000	-0.0053	0.0000	0.0000
O 11	0.0000	0.0000	0.0000	0.0000	0.0000	0.0000	0.0000	0.0000
O 12	0.0000	0.0017	0.0000	0.0000	0.0000	0.0056	0.0000	-0.0004
O 13	0.0000	0.0000	-0.0043	0.0012	0.0000	0.0000	0.0000	0.0000
O 14	0.0000	0.0000	0.0000	0.0000	0.0000	0.0000	0.0000	0.0000
O 15	0.0000	0.0000	0.0000	0.0000	0.0000	0.0000	0.0000	0.0000
O 16	0.3540	0.0000	0.0000	0.0000	0.0000	0.0000	0.0000	0.0000
O 17	0.0000	0.0000	0.0000	0.0000	0.0000	0.0000	0.0000	0.0000
O 18	-0.0183	0.0228	0.0000	0.0000	0.0000	0.0000	0.0000	0.0000
O 19	0.0000	0.0000	0.0000	0.0000	0.0000	0.0000	0.0000	0.0000
O 20	0.0000	0.0000	0.0106	0.0028	0.0000	0.0000	0.0000	0.0000
T 1	0.0000	0.0000	0.0000	0.0000	0.0000	-0.1200	0.1568	0.0000
T 2	0.0000	0.0000	0.0000	0.0000	0.0000	0.0000	0.1359	0.0059
T 3	0.0000	0.0000	0.0000	0.0000	0.0000	0.1494	0.0000	0.0000
T 4	0.0000	0.0000	0.0000	0.0000	0.0000	0.0000	0.0000	0.0000
T 5	0.0000	0.0000	0.0000	0.0000	0.0000	0.0000	0.0000	0.0000
T 6	0.0000	0.0000	0.0000	0.0000	0.0000	0.0000	0.0000	0.0000
T 7	0.0000	0.0000	0.0000	0.0000	0.0082	0.0000	0.0157	0.0000
T 8	0.0000	0.0000	0.0000	0.0000	0.0146	0.0000	0.0095	0.0005
T 9	0.0000	0.0000	0.0000	0.0000	0.0000	0.0000	0.0076	0.0000
T 10	0.0000	0.0000	0.0000	0.0000	-0.0771	0.0000	-0.0419	0.0000
T 11	0.0000	0.0000	0.0000	0.0000	0.0000	0.0000	0.0000	0.0000
T 12	0.0000	0.0000	0.0000	0.0000	-0.0092	0.0000	0.0000	-0.0003
T 13	-0.0489	-0.0020	0.0000	0.0000	0.0000	0.0156	0.0000	0.0000
T 14	0.0000	0.0000	0.0000	0.0000	0.0341	0.0000	0.0257	0.0000
T 15	0.0000	0.0000	0.0000	0.0000	0.0000	0.0000	0.0000	0.0000
T 16	0.0000	0.0000	0.0000	0.0000	0.0000	0.0000	0.0000	0.0000
T 17	0.0000	0.0000	0.0000	0.0000	0.0000	0.0000	0.0000	0.0000
T 18	0.0000	0.0000	0.0000	0.0000	0.0121	0.0010	0.0000	0.0000
T 19	0.0000	0.0000	-0.0111	0.0006	0.0112	0.0000	0.0132	0.0009
T 20	0.0000	0.0000	0.0000	0.0000	-0.0230	0.0000	-0.0137	-0.0007
T 21	0.0000	0.0000	0.0000	0.0000	0.0000	0.0000	0.0000	0.0000
T 22	0.0000	0.0000	0.0000	0.0000	0.0000	0.0000	0.0000	0.0000
T 23	0.0000	0.0000	0.0000	0.0000	0.0000	0.0000	0.0000	0.0000
T 24	0.0000	0.0000	0.1197	0.0083	0.0000	-0.0020	0.0000	0.0000
T 25	0.0000	0.0000	0.0000	0.0000	0.0000	0.0000	0.0000	0.0000
T 26	0.0000	0.0000	0.0000	0.0000	0.0000	0.0000	0.0000	0.0000
T 27	0.0000	0.0000	0.0000	0.0000	0.0000	0.0000	0.0000	0.0000
T 28	0.0000	0.0000	0.0000	0.0000	0.0000	0.0000	0.0000	0.0000
T 29	0.0000	0.0000	0.0000	0.0000	0.0000	0.0000	0.0000	0.0000
T 30	-0.0056	-0.0046	0.0000	0.0000	0.0000	0.0000	0.0000	0.0000

Table 3.A.12: TS site CE coefficients for the $Pd_{96}Ru_4$, $Pd_{96}Sc_4$, $Pd_{96}Ti_4$, and $Pd_{96}Tm_4$ alloys. O site parameter contributions identified as O 1- O 20 and T site parameter contribution identified as T 1 – T 30 as described in Table 3.A.2 and Table 3.A.3. Coefficients for the CE model for E_b are listed separately from the coefficients of the ZPE for each individual alloy. All coefficients have units of eV.

	$Pd_{96}Ru_4$		$Pd_{96}Sc_4$		$Pd_{96}Ti_4$		$Pd_{96}Tm_4$	
	E_b	ZPE	E_b	ZPE	E_b	ZPE	E_b	ZPE
E_0	0.2453	0.1352	0.3055	0.2033	-0.3588	0.8587	0.5075	0.1816
O 1	0.0494	-0.0035	0.0000	0.0000	0.0570	0.0301	0.0000	0.0000
O 2	0.0000	0.0000	0.0000	0.0000	0.0000	0.0000	0.0000	0.0000
O 3	0.0000	0.0000	0.0000	0.0000	0.0000	0.0000	0.0182	0.0073
O 4	0.0000	0.0000	0.0000	0.0000	0.0000	0.0000	0.0000	0.0000
O 5	0.0000	0.0000	0.0000	0.0000	0.0000	0.0000	0.0000	0.0000
O 6	0.0000	0.0000	0.0000	0.0000	0.0000	0.0000	0.0000	0.0000
O 7	0.0000	0.0000	0.0000	0.0000	0.0000	0.0000	0.0000	0.0000
O 8	0.0000	0.0000	0.0000	0.0000	-0.0072	0.0212	0.0000	0.0000
O 9	0.0000	0.0000	0.0000	0.0000	0.0000	0.0000	0.0000	0.0000
O 10	0.0000	0.0000	0.0056	-0.0014	0.0000	0.0000	0.0000	0.0000
O 11	0.0000	0.0000	0.0000	0.0000	0.0672	-0.0048	0.0000	0.0000
O 12	0.0000	0.0000	0.0000	0.0000	0.0000	0.0000	0.0000	0.0000
O 13	0.0000	0.0000	-0.0045	0.0013	0.0000	0.0000	0.0000	0.0000
O 14	0.0000	0.0000	0.0000	0.0000	0.0000	0.0000	0.0000	0.0000
O 15	0.0000	0.0000	0.0000	0.0000	0.0000	0.0000	0.0006	0.0011
O 16	0.0000	0.0000	0.0000	0.0000	0.0000	0.0000	0.0000	0.0000
O 17	-0.0093	-0.0027	0.0000	0.0000	0.0000	0.0000	0.0000	0.0000
O 18	0.0000	0.0000	0.0000	0.0000	0.0000	0.0000	0.0000	0.0000
O 19	0.0000	0.0000	0.0000	0.0000	0.0000	0.0000	0.0000	0.0000
O 20	0.0000	0.0000	0.0267	0.0040	0.0000	0.0000	0.0878	0.0017
T 1	0.0000	0.0000	0.0000	0.0000	-0.4235	0.4324	0.0000	0.0000
T 2	0.0000	0.0000	0.0000	0.0000	0.0000	0.0000	0.0000	0.0000
T 3	0.0000	0.0000	0.0000	0.0000	0.5741	0.0693	0.0000	0.0000
T 4	0.0000	0.0000	0.0000	0.0000	0.0000	0.0000	0.0000	0.0000
T 5	0.0000	0.0000	0.0000	0.0000	0.0000	0.0000	0.0000	0.0000
T 6	0.0000	0.0000	0.0000	0.0000	0.0000	0.0000	0.0000	0.0000
T 7	0.0000	0.0000	0.0000	0.0000	-0.0785	0.1119	0.0000	0.0000
T 8	0.0000	0.0000	0.0000	0.0000	0.0000	0.0000	0.0000	0.0000
T 9	0.0000	0.0000	0.0000	0.0000	0.0000	0.0000	0.0000	0.0000
T 10	0.0000	0.0000	0.0000	0.0000	0.0000	0.0000	0.0000	0.0000
T 11	0.0000	0.0000	0.0000	0.0000	0.0000	0.0000	0.0000	0.0000
T 12	0.0000	0.0000	0.0000	0.0000	0.0000	0.0000	0.0000	0.0000
T 13	-0.0363	-0.0002	0.0000	0.0000	0.0000	0.0000	0.0000	0.0000
T 14	0.0000	0.0000	0.0000	0.0000	0.0000	0.0000	0.0000	0.0000
T 15	0.0000	0.0000	0.0000	0.0000	0.0000	0.0000	0.0000	0.0000
T 16	0.0000	0.0000	0.0000	0.0000	0.0000	0.0000	0.0000	0.0000
T 17	0.0000	0.0000	0.0000	0.0000	0.0000	0.0000	0.0000	0.0000
T 18	0.0000	0.0000	0.0000	0.0000	0.0000	0.0000	-0.0310	-0.0009
T 19	0.0000	0.0000	0.0000	0.0000	-0.0162	0.0014	0.0000	0.0000
T 20	0.0000	0.0000	0.0000	0.0000	0.0000	0.0000	0.0000	0.0000
T 21	0.0000	0.0000	0.0000	0.0000	0.0000	0.0000	0.0000	0.0000
T 22	0.0000	0.0000	0.0000	0.0000	0.0000	0.0000	0.0000	0.0000
T 23	0.0000	0.0000	0.0000	0.0000	0.0000	0.0000	0.0000	0.0000
T 24	0.0000	0.0000	0.1283	0.0118	0.0000	0.0000	0.0000	0.0000
T 25	0.0000	0.0000	0.0000	0.0000	0.0000	0.0000	0.0000	0.0000
T 26	0.0000	0.0000	0.0000	0.0000	0.0000	0.0000	0.0000	0.0000
T 27	0.0000	0.0000	0.0000	0.0000	0.0000	0.0000	0.0000	0.0000
T 28	0.0000	0.0000	0.0000	0.0000	0.0000	0.0000	0.0000	0.0000
T 29	0.0038	-0.0019	0.0000	0.0000	0.0000	0.0000	0.0000	0.0000
T 30	0.0000	0.0000	0.0000	0.0000	0.0000	0.0000	0.0000	0.0000

Table 3.A.13: The parameters for solubility for the simplified DFT-based models for the 50 elements tabulated.

	Ag	Al	Au	Bi	Cd	Ce	Co	Cr
E_2	0.0338	0.1546	0.1054	0.3242	0.1231	0.1481	-0.0755	0.0729
E_3	-0.0100	0.0200	-0.0036	0.0473	0.0110	0.0382	-0.0086	0.0126
E_4	-0.0009	-0.0284	0.0033	0.0096	-0.0185	0.0008	0.0014	0.0081
E_2^{ZPE}	0.0235	0.0325	0.0324	0.0577	0.0423	0.0661	0.0281	0.0117
E_3^{ZPE}	0.0028	0.0097	-0.0008	0.0032	0.0056	0.0207	0.0004	-0.0013
E_4^{ZPE}	-0.0386	-0.0386	-0.0342	-0.0362	-0.0388	-0.0496	-0.0304	-0.0280

	Cu	Dy	Er	Eu	Fe	Ga	Gd	Hf
E_2	-0.0120	0.0878	0.0890	0.0259	0.0588	0.1698	0.0900	0.1365
E_3	-0.0151	0.0239	0.0254	-0.0077	-0.0009	0.0134	0.0225	0.0339
E_4	-0.0038	-0.0099	-0.0118	-0.0041	0.0175	-0.0218	-0.0072	-0.0146
E_2^{ZPE}	0.0047	0.0610	0.0511	0.0322	0.0111	0.0249	0.0531	0.0310
E_3^{ZPE}	-0.0003	0.0052	0.0126	0.0225	-0.0020	0.0012	0.0042	0.0051
E_4^{ZPE}	-0.0317	-0.0525	-0.0565	-0.0338	-0.0289	-0.0291	-0.0530	-0.0331

	Ho	In	Ir	Li	Lu	Mg	Mn	Mo
E_2	0.0913	0.2084	0.0527	-0.1174	0.0938	0.0412	0.0331	0.1644
E_3	0.0249	0.0232	0.0144	-0.0153	0.0234	0.0068	-0.0545	0.0251
E_4	-0.0110	-0.0269	0.0079	-0.0088	-0.0152	-0.0179	0.0088	0.0196
E_2^{ZPE}	0.0183	0.0290	0.0438	0.0297	0.0340	0.0240	0.0106	0.0285
E_3^{ZPE}	-0.0103	0.0028	0.0042	0.0015	0.0119	0.0022	0.0045	0.0061
E_4^{ZPE}	-0.0215	-0.0320	-0.0339	-0.0346	-0.0238	-0.0330	-0.0309	-0.0267

	Na	Nb	Ni	Os	Pb	Pt	Re	Rh
E_2	-0.0794	0.1479	-0.2147	0.1291	0.2879	0.0957	0.2233	-0.0298
E_3	-0.0242	0.0307	-0.2149	0.0231	0.0360	0.0110	0.0330	0.0027
E_4	-0.0083	-0.0016	0.2411	0.0169	-0.0041	-0.0018	0.0192	0.0058
E_2^{ZPE}	0.0295	0.0319	-0.0021	0.0429	0.0388	-0.0027	0.0203	0.0270
E_3^{ZPE}	0.0211	0.0087	0.0016	0.0052	0.0044	-0.0003	0.0081	0.0020
E_4^{ZPE}	-0.0387	-0.0293	-0.0331	-0.0280	-0.0375	-0.0320	-0.0261	-0.0346

	Ru	Sb	Sc	Sm	Sn	Ta	Tb	Tc
E_2	0.0397	0.3389	0.0528	0.0974	0.2848	0.1844	0.0887	0.1331
E_3	0.0277	0.0397	0.0191	0.0213	0.0323	0.0319	0.0232	0.0250
E_4	0.0028	0.0104	-0.0151	-0.0052	-0.0121	-0.0084	-0.0087	0.0207
E_2^{ZPE}	0.0372	0.0322	0.0355	0.0332	0.0319	0.0313	0.0568	0.0111
E_3^{ZPE}	0.0012	0.0039	0.0063	-0.0201	-0.0002	0.0091	0.0052	0.0070
E_4^{ZPE}	-0.0358	-0.0309	-0.0380	-0.0276	-0.0286	-0.0282	-0.0524	-0.0287

Table 3.A.13 continued

	Te	Ti	Tl	Tm	V	W	Y	Yb
E_2	0.2842	0.0803	0.2455	0.0935	0.0923	0.2211	0.0634	0.0129
E_3	0.0327	0.0218	0.0308	0.0259	0.0154	0.0315	0.0103	-0.0017
E_4	0.0126	-0.0092	-0.0222	-0.0162	0.0067	0.0050	-0.0082	-0.0082
E_2^{ZPE}	0.0389	0.0314	0.0386	0.0386	0.0255	0.0294	0.0472	0.0596
E_3^{ZPE}	0.0030	0.0020	0.0051	0.0207	0.0012	0.0119	0.0118	0.0145
E_4^{ZPE}	-0.0316	-0.0298	-0.0393	-0.0339	-0.0272	-0.0265	-0.0486	-0.0579

	Zn	Zr
E_2	0.0901	0.1113
E_3	0.0045	0.0332
E_4	-0.0118	-0.0119
E_2^{ZPE}	0.0219	0.0343
E_3^{ZPE}	0.0010	0.0061
E_4^{ZPE}	-0.0303	-0.0356

Table 3.A.14: The parameters for diffusivity for the simplified DFT-based models for the 50 elements tabulated. Because the ZPE are generally insensitive to the chemical effect due to the presence of M atoms, the ZPE for all interstitial sites are modeled as being independent of the number of M atoms near the TS.

	Ag	Al	Au	Bi	Cd	Ce	Co	Cr
$E_2(O)$	0.0342	0.1414	0.1160	0.2903	0.1019	0.1088	-0.0717	0.0532
$E_3(O)$	-0.0095	-0.0082	0.0054	0.0133	-0.0102	-0.0011	-0.0048	-0.0071
$E_4(O)$	-0.0013	-0.0053	0.0007	0.0435	0.0027	0.0402	-0.0024	0.0278
$E_2^{ZPE}(O)$	0.0216	0.0302	0.0182	0.0424	0.0367	0.0288	0.0347	0.0149
$E_3^{ZPE}(O)$	0.0010	0.0048	-0.0035	-0.0120	0.0000	-0.0166	0.0071	0.0018
$E_4^{ZPE}(O)$	-0.0368	-0.0318	-0.0272	-0.0210	-0.0331	-0.0123	-0.0371	-0.0312
$E_2(T)$	0.0928	0.2751	0.1923	0.0000	0.0000	0.0000	-0.0688	0.0938
$E_3(T)$	-0.0229	0.0041	-0.0166	-0.0687	-0.0476	-0.0865	0.0356	0.0165
$E_4(T)$	0.0069	-0.0056	0.0178	0.1096	0.0396	0.1072	-0.0343	0.0131
$E_2^{ZPE}(T)$	0.0027	0.0153	-0.0077	0.0000	0.0000	0.0000	-0.0043	0.0127
$E_3^{ZPE}(T)$	-0.0015	0.0048	-0.0025	-0.0030	-0.0026	-0.0032	0.0056	0.0072
$E_4^{ZPE}(T)$	0.0027	-0.0016	0.0029	0.0074	0.0048	0.0179	-0.0038	-0.0051
E_5	-0.0144	0.0689	0.0119	0.0838	-0.0002	0.0036	0.0374	0.0670
E_6	-0.0067	0.0276	0.0029	0.0271	0.0020	0.0288	0.0125	0.0284
E_7	0.1818	0.2542	0.2244	0.4197	0.3119	0.2241	-0.1445	-0.0215
E_8	-0.0179	-0.0374	-0.0189	-0.1218	-0.0638	-0.1677	0.0223	-0.0392
E_9	0.0027	0.0135	0.0149	0.1538	0.0539	0.1840	-0.0423	0.0384

	Cu	Dy	Er	Eu	Fe	Ga	Gd	Hf
$E_2(O)$	-0.0035	0.0443	0.0440	-0.0021	0.0548	0.1521	0.0480	0.0904
$E_3(O)$	-0.0066	-0.0196	-0.0196	-0.0357	-0.0049	-0.0042	-0.0194	-0.0122
$E_4(O)$	-0.0123	0.0336	0.0331	0.0239	0.0215	-0.0042	0.0348	0.0315
$E_2^{ZPE}(O)$	0.0121	0.0350	0.0048	0.0168	0.0249	0.0295	0.0133	0.0145
$E_3^{ZPE}(O)$	0.0058	-0.0209	-0.0338	0.0071	0.0117	0.0059	-0.0356	-0.0114
$E_4^{ZPE}(O)$	-0.0363	-0.0264	-0.0101	-0.0184	-0.0426	-0.0337	-0.0132	-0.0166
$E_2(T)$	0.0019	0.0000	0.0000	0.0000	-0.0209	0.3079	0.0000	0.1536
$E_3(T)$	0.0279	-0.0911	-0.0849	-0.0997	-0.0258	0.0063	-0.0981	-0.0348
$E_4(T)$	-0.0442	0.0879	0.0831	0.0720	0.0463	-0.0072	0.0940	0.0637
$E_2^{ZPE}(T)$	0.0023	0.0000	0.0000	0.0000	0.0004	0.0238	0.0000	-0.0021
$E_3^{ZPE}(T)$	0.0046	-0.0032	-0.0018	-0.0026	0.0047	0.0050	-0.0036	0.0008
$E_4^{ZPE}(T)$	-0.0027	0.0178	0.0182	0.0166	-0.0030	-0.0017	0.0184	0.0035
E_5	0.0169	-0.0276	-0.0222	-0.0557	0.0695	0.0676	-0.0320	0.0455
E_6	0.0066	0.0011	0.0025	-0.0162	0.0172	0.0274	-0.0001	0.0265
E_7	0.0015	0.1927	0.1981	0.2175	-0.0955	0.2869	0.1723	0.2132
E_8	0.0337	-0.1500	-0.1433	-0.1241	0.0013	-0.0246	-0.1559	-0.1170
E_9	-0.0637	0.1545	0.1477	0.1162	0.0000	0.0020	0.1617	0.1278

Table 3.A.14 continued

	Ho	In	Ir	Li	Lu	Mg	Mn	Mo
$E_2(O)$	0.0456	0.1798	0.0527	-0.1272	0.0460	0.0139	0.0245	0.1388
$E_3(O)$	-0.0208	-0.0054	0.0142	-0.0251	-0.0244	-0.0205	-0.0631	-0.0004
$E_4(O)$	0.0346	0.0017	0.0080	0.0010	0.0326	0.0095	0.0174	0.0451
$E_2^{ZPE}(O)$	0.0259	0.0257	0.0427	0.0362	0.0161	0.0226	0.0163	0.0151
$E_3^{ZPE}(O)$	-0.0028	-0.0005	0.0051	0.0080	-0.0060	0.0008	0.0102	-0.0074
$E_4^{ZPE}(O)$	-0.0291	-0.0287	-0.0339	-0.0411	-0.0059	-0.0316	-0.0366	-0.0133
$E_2(T)$	0.0000	0.0000	0.1357	-0.0965	0.0000	0.0659	0.0576	0.2496
$E_3(T)$	-0.0888	-0.0407	0.0291	0.0050	-0.0757	-0.0279	-0.0357	-0.0031
$E_4(T)$	0.0862	0.0419	-0.0003	-0.0293	0.0740	0.0218	-0.0027	0.0615
$E_2^{ZPE}(T)$	0.0000	0.0000	0.0028	0.0183	0.0000	0.0163	0.0060	0.0198
$E_3^{ZPE}(T)$	0.0039	-0.0005	0.0019	0.0066	0.0025	0.0024	0.0056	0.0041
$E_4^{ZPE}(T)$	0.0164	0.0041	0.0002	-0.0046	0.0237	0.0003	-0.0032	-0.0007
E_5	-0.0256	0.0176	0.0623	-0.0198	-0.0135	-0.0024	0.0564	0.1869
E_6	0.0020	0.0347	0.0212	-0.0014	0.0065	0.0040	0.0239	0.1305
E_7	0.1996	0.4220	0.0155	-0.0137	0.2099	0.1851	-0.0185	0.0674
E_8	-0.1459	-0.0967	-0.0033	0.0098	-0.1357	-0.0528	-0.0251	-0.1819
E_9	0.1505	0.0750	0.0079	-0.0399	0.1373	0.0404	-0.0389	0.1158

	Na	Nb	Ni	Os	Pb	Pt	Re	Rh
$E_2(O)$	-0.0961	0.1571	-0.0056	0.1152	0.2566	0.0870	0.1961	-0.0282
$E_3(O)$	-0.0409	0.0400	-0.0059	0.0112	0.0047	0.0022	0.0058	0.0043
$E_4(O)$	0.0084	-0.0109	0.0320	0.0262	0.0273	0.0069	0.0464	0.0042
$E_2^{ZPE}(O)$	0.0309	0.0332	0.0023	0.0490	0.0336	-0.0008	0.0204	0.0263
$E_3^{ZPE}(O)$	0.0224	0.0088	0.0061	0.0111	-0.0009	0.0016	0.0082	0.0014
$E_4^{ZPE}(O)$	-0.0400	-0.0298	-0.0375	-0.0346	-0.0322	-0.0339	-0.0262	-0.0340
$E_2(T)$	-0.0764	0.2632	-0.0232	0.2053	0.0000	0.1076	0.3263	0.0144
$E_3(T)$	-0.0442	0.0347	0.0289	0.0137	-0.0726	0.0096	0.0197	0.0178
$E_4(T)$	0.0129	0.0077	-0.0006	0.1327	0.0842	-0.0003	0.0487	-0.0066
$E_2^{ZPE}(T)$	0.0202	0.0166	-0.0047	0.0020	0.0000	-0.0016	0.0119	0.0020
$E_3^{ZPE}(T)$	0.0014	0.0013	0.0055	0.0032	-0.0021	-0.0010	0.0045	0.0013
$E_4^{ZPE}(T)$	0.0004	0.0027	-0.0029	-0.0017	0.0070	0.0026	-0.0012	0.0006
E_5	-0.0575	0.0736	0.0272	0.0982	0.0511	0.0315	0.1243	0.0242
E_6	-0.0206	0.0358	0.0104	0.0341	0.0110	0.0106	0.0456	0.0086
E_7	0.1265	0.3111	-0.0671	0.0516	0.3817	0.0508	0.1441	-0.0435
E_8	-0.0354	0.0115	0.0213	-0.0242	-0.0966	-0.0026	-0.0627	-0.0018
E_9	0.0158	0.0038	-0.0099	0.0359	0.1115	-0.0024	0.0924	-0.0028

Table 3.A.14 continued

	Ru	Sb	Sc	Sm	Sn	Ta	Tb	Tc
$E_2(O)$	0.0397	0.3077	0.0136	0.0565	0.2561	0.1457	0.0461	0.1120
$E_3(O)$	0.0277	0.0085	-0.0201	-0.0197	0.0036	-0.0068	-0.0194	0.0040
$E_4(O)$	0.0028	0.0417	0.0242	0.0357	0.0166	0.0303	0.0339	0.0418
$E_2^{ZPE}(O)$	0.0372	0.0252	0.0215	0.0223	0.0284	0.0211	0.0272	0.0068
$E_3^{ZPE}(O)$	0.0012	-0.0031	-0.0077	-0.0309	-0.0037	-0.0011	-0.0244	0.0027
$E_4^{ZPE}(O)$	-0.0358	-0.0239	-0.0240	-0.0168	-0.0251	-0.0180	-0.0228	-0.0244
$E_2(T)$	0.0999	0.0000	0.0476	0.0000	0.0000	0.2645	0.0000	0.2066
$E_3(T)$	0.0224	-0.0376	-0.0461	-0.1070	-0.0368	-0.0100	-0.0946	0.0138
$E_4(T)$	0.0125	0.0842	0.0511	0.1018	0.0580	0.0526	0.0907	0.0425
$E_2^{ZPE}(T)$	0.0049	0.0000	0.0129	0.0000	0.0000	0.0162	0.0000	0.0113
$E_3^{ZPE}(T)$	0.0021	-0.0007	-0.0004	-0.0035	-0.0007	0.0024	-0.0027	0.0040
$E_4^{ZPE}(T)$	-0.0004	0.0050	0.0024	0.0175	0.0050	0.0016	0.0177	-0.0014
E_5	0.0520	0.1023	0.0015	-0.0381	0.0849	0.0910	-0.0292	0.0843
E_6	0.0199	0.0342	0.0106	-0.0034	0.0274	0.0388	0.0014	0.0323
E_7	-0.0062	0.4524	0.1694	0.1781	0.4255	0.2202	0.1739	0.0677
E_8	-0.0168	-0.0955	-0.1016	-0.1640	-0.0886	-0.1047	-0.1525	-0.0515
E_9	0.0283	0.1235	0.0979	0.1706	0.0944	0.1172	0.1577	0.0748

	Te	Ti	Tl	Tm	V	W	Y	Yb
$E_2(O)$	0.2665	0.0803	0.2144	0.0471	0.0686	0.1880	0.0253	-0.0182
$E_3(O)$	0.0150	0.0213	-0.0003	-0.0205	-0.0083	-0.0016	-0.0277	-0.0328
$E_4(O)$	0.0303	-0.0091	0.0089	0.0301	0.0303	0.0382	0.0298	0.0228
$E_2^{ZPE}(O)$	0.0302	0.0319	0.0312	0.0039	0.0220	0.0215	0.0183	0.0307
$E_3^{ZPE}(O)$	-0.0057	0.0024	-0.0022	-0.0141	-0.0023	0.0041	-0.0171	-0.0144
$E_4^{ZPE}(O)$	-0.0229	-0.0298	-0.0319	0.0008	-0.0237	-0.0186	-0.0197	-0.0290
$E_2(T)$	0.0000	0.1705	0.0000	0.0000	0.1386	0.3279	0.0000	0.0000
$E_3(T)$	-0.0510	0.0247	-0.0636	-0.0822	0.0054	0.0059	-0.0900	-0.0769
$E_4(T)$	0.0868	-0.0024	0.0667	0.0776	0.0287	0.0516	0.0858	0.0506
$E_2^{ZPE}(T)$	0.0000	0.0236	0.0000	0.0000	0.0177	0.0200	0.0000	0.0000
$E_3^{ZPE}(T)$	-0.0013	0.0014	-0.0031	-0.0021	0.0053	0.0038	-0.0029	-0.0005
$E_4^{ZPE}(T)$	0.0060	0.0018	0.0067	0.0232	-0.0017	0.0004	0.0065	0.0154
E_5	0.0897	0.0518	0.0401	-0.0189	0.0710	0.1223	-0.0267	-0.0453
E_6	0.0306	0.0290	0.0134	0.0040	0.0331	0.0470	-0.0076	-0.0077
E_7	0.3969	0.1289	0.3899	0.1993	0.0745	0.2013	0.1633	0.2017
E_8	-0.0971	-0.0816	-0.0970	-0.1401	-0.0670	-0.0935	-0.1291	-0.1096
E_9	0.1170	0.0793	0.0962	0.1404	0.0712	0.1129	0.1350	0.0954

Table 3.A.14 continued

	Zn	Zr
$E_2(O)$	0.0756	0.0672
$E_3(O)$	-0.0101	-0.0109
$E_4(O)$	0.0028	0.0322
$E_2^{ZPE}(O)$	0.0280	0.0186
$E_3^{ZPE}(O)$	0.0071	-0.0096
$E_4^{ZPE}(O)$	-0.0364	-0.0199
$E_2(T)$	0.1888	0.1008
$E_3(T)$	0.0018	-0.0435
$E_4(T)$	-0.0024	0.0698
$E_2^{ZPE}(T)$	0.0124	-0.0066
$E_3^{ZPE}(T)$	0.0050	-0.0005
$E_4^{ZPE}(T)$	-0.0022	0.0048
E_5	0.0288	0.0282
E_6	0.0135	0.0219
E_7	0.2197	0.2043
E_8	-0.0121	-0.1257
E_9	-0.0022	0.1372

CHAPTER 4

B-SITE DOPED BARIUM ZIRCONATE

4.1   Introduction

Perovskite-type oxides are candidates for proton-conducting electrolytic materials in applications such as fuel cells, gas sensors, ceramic membranes and steam electrolysers.[1, 2] Doped ABO_3 perovskites are especially interesting in this context as ceramic proton conductors when they can be developed with high proton conductivity.[3] Protons are introduced in the perovskite oxides by acceptor doping and are known to form a covalent bond with the oxygen lattice in perovskite oxides.[3, 4] Proton migration in doped perovskites occurs through two elementary steps, including transfer of protons between adjacent oxide ions and rotation.[5] Kreuer noted that proton diffusion can be affected by symmetry reduction and chemical alteration due to the presence of dopants.[3]

One potential problem with ceramic proton conductors with basic components such as Sr and Ba is that they are susceptible to carbonate and hydroxide formation in environments containing CO_2 and H_2O, respectively.[6] In considering ceramics for proton-conducting applications, chemical stability and proton conductivity are both important. Cerates and zirconates both exhibit significant proton conductivity.[7] Iwahara *et al*. found high proton conduction in $SrCeO_3$ and $BaCeO_3$.[1, 8, 9] However, unlike cerates, which have poor stability with respect to carbonate formation, zirconates are proton conductors with good chemical stability.[7, 10] Acceptor-doped $BaZrO_3$, in which Zr^{4+} is substituted with a trivalent dopant, has attracted considerable attention as an example of materials with these properties.[10] Y-doped $BaZrO_3$ is one such promising material providing excellent

chemical stability and high proton conductivity.[11]

There are a large number of possible trivalent dopants that can be used in $BaZrO_3$. Therefore, it is interesting to ask how stability with respect to carbonate and hydroxide formation and the overall proton conductivity vary among these dopants. In this chapter, we examine this question using first-principles Density Functional Theory (DFT) calculations. DFT calculations have become a useful complement to experimental studies of perovskites and have been used to study a wide range of questions related to defect formation and mobility.[4, 12-21] In many cases, these computational studies have focused on a single doped material. In this chapter, we aim to use efficient methods to examine a wide range of possible dopants: Y, In, Ga, Sc, Nd, Al, Tl, Sm, Dy, La, Pm, Er, and Ho.

After describing our computational methods in section 4.2, we begin in section 4.3 by examining the stability of doped $BaZrO_3$ with respect to carbonate and hydroxide formation. Our results are based on DFT calculations of reaction free energies at finite temperatures, which allow us to predict the phase stability of oxide and carbonate and hydroxide phases as functions of temperature and partial pressures of CO_2 and H_2O. We then consider the mobility of protons in each material. Proton diffusion is described by using extensive DFT calculations to determine the activation energies and hopping prefactors for local hops by protons and then incorporating this information within a lattice model for the doped material to determine net proton mobilities. Our calculations identify the small number of dopants that are known from prior experiments and simulations to enhance diffusivity relative to pure $BaZrO_3$,[3, 10, 13, 15, 22] and also identify several new dopants with this property. Because of the large number of dopants included

in our calculations, our results create a useful opportunity to explore the physical origins of the trends in chemical stability and proton mobility among different dopants. We explore several possible physical descriptors that can be used for this purpose.

One of the main conclusions from our calculations is that there is a simple tradeoff between chemical stability and proton conductivity in doped $BaZrO_3$: improvements in one property are strongly correlated with a decreased performance in the other. This outcome is unfortunate in the sense that there does not appear to be an ideal dopant for $BaZrO_3$ that enhances both properties of interest. Understanding this tradeoff, however, is useful because it will allow appropriate dopants to be chosen by weighing the relative importance of the two properties in any specific application of interest.

4.2   Calculation methods

The 0 K total energies of each solid compound considered are calculated using plane wave Density Functional Theory calculations.[23] We perform the DFT calculations using the Vienna *ab initio* Simulation Package (VASP) with the PW91 generalized gradient approximation (GGA) functional.[24-27] The projector augmented wave (PAW) method is used to describe the core electrons of each atom.[28] An energy cutoff of 500 eV is used for the plane wave basis set. *k*-points are obtained using the Monkhorst–Pack method[29] with the number of *k*-points chosen to give a spacing of about 0.028 Å^{-1} along the axes of the reciprocal unit cells.

For each compound we consider in the carbonate and hydroxide formation reaction, the lattice parameters and atomic positions are optimized using DFT

calculations with a single primitive cell starting from the experimental structures listed in the Inorganic Crystal Structure Database (ICSD).[30] The structural optimization of all materials is performed via a conjugate gradient method until the forces on all atoms are less than 0.03 eV/Å.

In our examination of chemical stability, we perform additional calculations to assess the temperature-dependent free energy of reaction. This requires calculation of the phonon density of states and the resulting vibrational contributions to the free energy for each material involved in a reaction.[31, 32] For solid materials, these calculations are performed using the PHONON code developed by Parlinski[33] using the same exchange-correlation functional and energy cutoff as for our total energy calculations. A displacement magnitude of 0.03 Å is applied. The vibrational density of states (VDOS) is used to compute the free energy of reaction at finite temperature, ΔG(T), within the harmonic approximation.[34] Pressure-volume (PV) contributions for solids are ignored, assuming that the difference between the chemical potential of solid phases can be approximated by the difference in their electronic energy and the vibrational free energy of the phonons.[31] Gas phase CO_2 and H_2O are treated as ideal gases. The free energies of CO_2 and H_2O are obtained from standard statistical mechanics as [35]

$$G_{CO2} = \frac{7}{2}RT + \sum_{i=1}^{4} \frac{N_a h v_i}{e^{h v_i / kT} - 1} - T S_{CO2}(T) \,, \tag{4.1}$$

$$G_{H2O} = 4RT + \sum_{j=1}^{3} \frac{N_a h v_j}{e^{h v_j / kT} - 1} - T S_{H2O}(T) \,,$$

where N_a is Avogadro's constant, R is the universal gas constant, T is temperature, v_i are the vibrational frequencies of CO_2 in G_{CO2}, and v_j are the vibrational frequencies of H_2O in G_{H2O}. The entropy of CO_2 and H_2O is calculated by the Shomate equation.[36]

We employ an efficient method to calculate transition states that relies on local optimization. Other theoretical studies of this kind have used the Nudged Elastic Band (NEB) method to find the transition states for proton transfer and rotation[13, 14]. Unfortunately, this approach is computationally expensive and significantly limits the number of transition states that can be examined. Our efficient approach is based on the observation that when an initial configuration is close enough to a true transition state, a quasi-Newton optimization leads to the saddle point.[37] This idea has been used previously to find hundreds of distinct transition states in studies of interstitial H in amorphous metals[38, 39]. Using the more efficient method described above makes it possible to examine large numbers of transition states. This method is useful because it is relatively straightforward to generate reasonable approximations for the geometries of transition states for proton hopping. NEB calculations can be applied to rigorously locate transition states for cases where the simpler approach is not successful. We do not have to use NEB calculations for any of the transition states described below.

4.2.1   DFT calculated results of geometry optimization

The optimized lattice constants for each compound considered in this work are presented in Table 4.1 along with the corresponding experimental data. Predicted values agree to within 3% of experimental lattice constants and angles, indicating good agreement. Calculated lattice constants by GGA functional are slightly larger than experimental lattice constants apart from La_2O_3, Pm_2O_3, Dy_2O_3, Ho_2O_3, and Er_2O_3.

Table 4.1. Comparison of the experimental[30] and the DFT calculated structural parameters for the 18 crystalline compounds considered in our calculations, with all lengths in Å and angles in degrees.

Compound	Space group	Structural Parameters (Å, degree)	
		Experimental	Calculated
ZrO_2	$P12_1/c1$	$a = 5.143$ $b = 5.204$ $c = 5.310$ $\beta = 99.166$	$a = 5.212$ $b = 5.286$ $c = 5.386$ $\beta = 99.574$
CeO_2	Fm-$3m$	$a = 5.414$	$a = 5.546$
Y_2O_3	Ia-3	$a = 10.611$	$a = 10.694$
Ga_2O_3	R-$3cH$	$a = 4.983$ $c = 13.433$ $\gamma = 120$	$a = 5.070$ $c = 13.627$ $\gamma = 120$
In_2O_3	Ia-3	$a = 10.117$	$a = 10.334$
Sc_2O_3	Ia-3	$a = 9.849$	$a = 9.901$
Nd_2O_3	P-$3m1$	$a = 3.827$ $c = 5.991$ $\gamma = 120$	$a = 3.860$ $c = 6.070$ $\gamma = 120$
Al_2O_3	R-$3cH$	$a = 4.762$ $c = 12.999$ $\gamma = 120$	$a = 4.804$ $c = 13.106$ $\gamma = 120$
Tl_2O_3	Ia-3	$a = 10.543$	$a = 10.890$
La_2O_3	P-$3m1$	$a = 3.940$ $c = 6.130$ $\gamma = 120$	$a = 3.939$ $c = 6.149$ $\gamma = 120$
Pm_2O_3	Ia-3	$a = 11.065$	$a = 11.065$
Sm_2O_3	Ia-3	$a = 10.920$	$a = 10.990$
Dy_2O_3	Ia-3	$a = 10.67$	$a = 10.660$
Ho_2O_3	Ia-3	$a = 10.606$	$a = 10.600$
Er_2O_3	Ia-3	$a = 10.548$	$a = 10.533$
$BaZrO_3$	Pm-$3m$	$a = 4.188$	$a = 4.252$
$BaCO_3$	$Pnma$	$a = 6.434$ $b = 5.315$ $c = 8.904$	$a = 6.582$ $b = 5.364$ $c = 9.003$
$Ba(OH)_2$	$Pnma$	$a = 11.033$ $b = 16.564$ $c = 7.112$	$a = 11.135$ $b = 16.759$ $c = 7.094$

4.3 Chemical stability

The carbonate formation reactions of doped $BaZrO_3$ in the presence of CO_2 and the hydroxide formation reactions in the presence of H_2O can be expressed as

$$BaZr_{0.75}\,M_{0.25}\,O_{3-\delta} + CO_2 \leftrightarrow BaCO_3 + 0.75\,ZrO_2 + 0.25\,M_2O_3 \,, \qquad (4.2)$$

$$BaZr_{0.75}\,M_{0.25}\,O_{3-\delta} + H_2O \leftrightarrow Ba(OH)_2 + 0.75\,ZrO_2 + 0.25\,M_2O_3 \,,$$
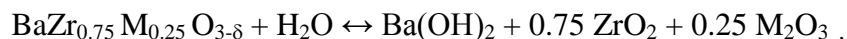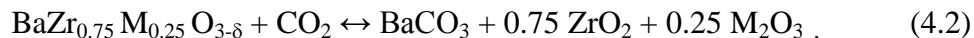
where M is a trivalent dopant such as Y, In, Ga, Sc, Nd, Al, Tl, Sm, Dy, La, Pm, Er, or Ho. We initially perform our calculations with the dopant-free system and find that at 323 K the free energy for the reaction ($BaZrO_3 + CO_2 \rightarrow BaCO_3 + ZrO_2$) is -70.8 kJ/mol. The experimental result at the same temperature is -83.6 kJ/mol.[40] This level of agreement between DFT-calculated and experimental free energies is similar to what has been observed for a variety of metal hydride decomposition reactions by Kim *et al.*[41]

After we investigate the stability of $BaZrO_3$, we extend our calculations to materials doped with M^{3+}, at the Zr site. Initially we examine the chemical stability of the common dopants, Y, In, Ga, and Sc, in $BaZrO_3$. When the dopants are present, oxygen vacancies are created to maintain overall charge neutrality.[42] Our calculations use a dopant concentration of 2/8 (25%), so the net stoichiometry of the doped materials is $Ba_8Zr_6M_2O_{23}$. Our calculations for doped $BaZrO_3$ use 2×2×2 unit cells in the computational supercell, so each supercell contained two (one) dopant atoms (O vacancy). After creating the O vacancy in the supercell, calculations are performed with various placements of the dopant atoms. The arrangement with the lowest energy is used for calculation of the VDOS. For Y, In, Ga, Sc, Al, Tl, Dy, Er and Ho, this state has two dopant atoms placed next to each other, whereas the two dopants in the lowest energy state for Nd, Sm, La and Pm are separated by 7.62, 7.60, 7.65 and 7.60 Å, respectively.

In computing the free energy for the doped materials, it is necessary to include the configurational entropy associated with disordered M^{3+} and oxygen vacancy.[43] The configurational entropy can be directly obtained from the Boltzmann definition of

entropy, $S = k\ln\Omega$, where Ω is the number of configurations of dopants and vacancies possible.[44] For simplicity, we estimate the configurational entropy by assuming that all orderings of the dopants and vacancies are equally likely. This gives a configurational entropy for $BaZr_{0.75}M_{0.25}O_{3-\delta}$ of 54.1 J K^{-1} mol^{-1}. This value is likely to overestimate the true configurational entropy because of the small differences in energy that exist between various configurations of the vacancies and defects, but we do not attempt to quantify this effect further.

The equilibrium condition for carbonate formation and hydroxide formation follows a van't Hoff relation:

$$\frac{P_{CO2}}{P_0} = \exp\left(\frac{\Delta G}{RT}\right) , \tag{4.3}$$

$$\frac{P_{H2O}}{P_0} = \exp\left(\frac{\Delta G}{RT}\right) , \tag{4.4}$$

$$\Delta G(T) = \Delta E_0 - n_1 G_{CO2}(T) + \Delta F^{solids}(T) , \tag{4.5}$$

$$\Delta G(T) = \Delta E_0 - n_1 G_{H2O}(T) + \Delta F^{solids}(T) , \tag{4.6}$$

where ΔE_0 is the difference of ground state total energy determined using DFT between the reactants and products, ΔG is Gibbs free energy difference between the reactants and products, n_1 is the number of moles of CO_2 involved in the reaction in Equation (4.5) and the number of moles of H_2O involved in the reaction in Equation (4.6), G_{CO2} is a free energy of CO_2, G_{H2O} is a free energy of H_2O. ΔF^{solids} is the vibrational free energy change between the solids of products and reactants, and P_0 is the standard state reference pressure. The equilibrium CO_2 pressure associated with carbonate formation of undoped $BaZrO_3$ as predicted by our calculations is shown in Figure 4.1, using $P_0 = 1$ bar. We denote the temperature at which carbonate formation becomes favorable as T*. As the

CO_2 pressure is increased, the critical temperature increases. For CO_2 pressures of 0.01, 0.1, 1.0, and 10.0 bar, T* of the undoped material is calculated to be 576, 627, 688 and 763 K, respectively. Among a set of materials, perovskites with higher critical temperatures are more susceptible to carbonate formation and are less chemically stable. Because every material we consider depends on CO_2 pressure in the same way, we only report results with a CO_2 pressure of 1 bar below.
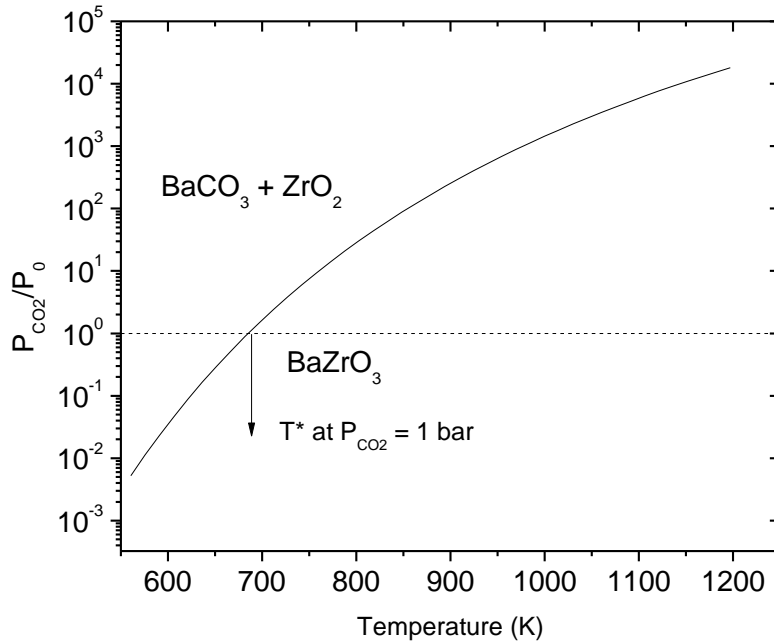
Figure 4.1: van't Hoff plot for the carbonate formation reaction of undoped $BaZrO_3$, $BaZrO_3 + CO_2 \leftrightarrow BaCO_3 + ZrO_2$. The horizontal dashed line refers to $P_{CO2}/P_0 = 1$.

Similar to the carbonate formation reaction, as the H_2O pressure is increased, the critical temperature increases in hydroxide formation reaction. Given the previously stated assumption of H_2O as an ideal gas, T* of the undoped material is calculated to be 120, 130, 143 and 159 K for corresponding H_2O pressures of 0.01, 0.1, 1.0, and 10.0 bar. $BaZrO_3$ is more stable against water than against CO_2.[45] Among a set of materials,

perovskites with higher critical temperatures are more susceptible to hydroxide formation and are less chemically stable. Because the methods we use for carbonate formation reaction and hydroxide formation reaction are the same, we only report the method with carbonate formation reaction.
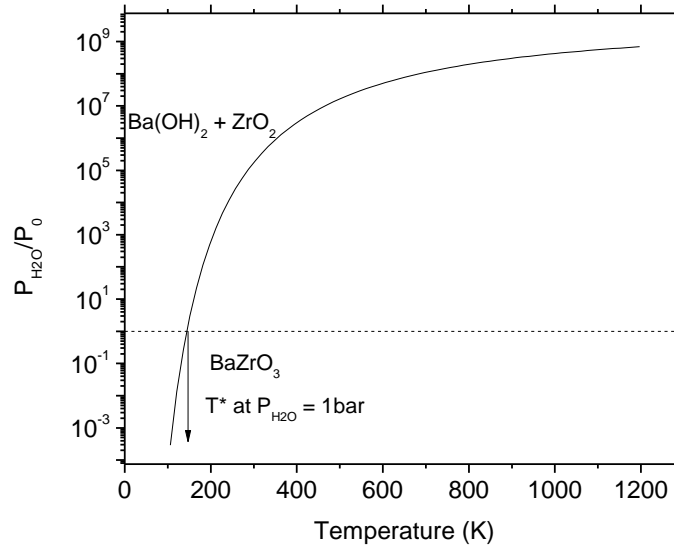
Figure 4.2: van't Hoff plot for the hydroxide formation reaction of undoped $BaZrO_3$, $BaZrO_3 + H_2O \leftrightarrow Ba(OH)_2 + ZrO_2$. The horizontal dashed line refers to $P_{CO2}/P_0 = 1$.
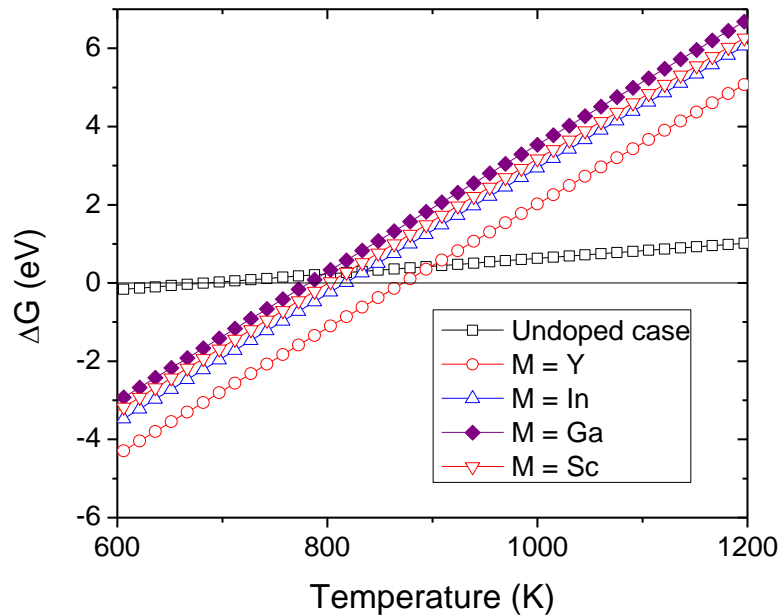
Figure 4.3: Free energy of reaction, ΔG, as a function of temperature for carbonate formation reactions. The undoped material is shown using unfilled squares for the reaction $BaZrO_3 + CO_2 \leftrightarrow BaCO_3 + ZrO_2$. The results for the doped materials correspond to the reaction $Ba_8Zr_6M_2O_{23} + 8CO_2 \leftrightarrow 8BaCO_3 + 6ZrO_2 + M_2O_3$ for M = Y, In, Ga, or Sc.

A stability diagram for the doped materials investigated is shown in Figure 4.3 for a CO_2 pressure of 1 bar. Figure 4.3 shows that the rank of the chemical stability of M-doped $BaZrO_3$ with respect to CO_2 is Ga (T* = 786 K) > Sc (T* = 805 K) > In (T* = 821 K) > Y (T* = 875 K). In the same way for a H_2O pressure of 1 bar, the rank of the chemical stability of M-doped $BaZrO_3$ with respect to H_2O is Ga (T* = 253 K) > Sc (T* = 266 K) > In (T* = 288 K) > Y (T* = 335 K). The same ranking of chemical stabilities with respect to the hydroxide and carbonate formation reaction is observed; although each doped $BaZrO_3$ is more stable with respect to H_2O than to CO_2.

Although yttrium is known to be a useful dopant to improve proton conductivity[3], it is not favorable in terms of the chemical stability compared to the other

dopants we examine. This is consistent with an experimental study that found increasing Y dopants in $BaIn_{0.3-x}Y_xCe_{0.7}O_{3-d}$ lower the CO_2 tolerance.[46] For undoped $BaZrO_3$, the calculated value of T* is 688 K when P_{CO2} is 1 bar, and the calculated value of T* is 143 K when P_{H2O} is 1 bar; each of the doped materials we study show a higher critical temperature than the undoped material.

Computing the VDOS of a solid is much more time consuming than a DFT total energy calculation. In the calculations above, each doped material requires 117 displacement calculations due to the broken symmetry associated with the dopants and oxygen vacancy, whereas undoped material only needs 4 displacement calculations. Because of the computational expense of these calculations, it is useful to have a simplified model to efficiently screen materials. This concept has proved useful, for example, in extensive computational studies of light metal hydrides for hydrogen storage[31, 43, 47]. We develop a similar approach, noting that the VDOS are very similar for materials described above with the same stoichiometries. Since calculating thermodynamic properties involves integration of the VDOS,[34] the contributions of these vibrational effects to doped $BaZrO_3$ materials are quite similar. Figure 4.4 shows that the temperature-dependent vibrational free energies of the solids are comparable for Y, In, Ga, and Sc doped $BaZrO_3$. This implies that a far simpler calculation can be performed including DFT total energies and finite temperature thermodynamics reliably estimated using a correction factor based on the detailed calculations in Figure 4.4. We define the correction factor as the average of the ΔF^{solids} for the four doped materials shown in Figure 4.4.
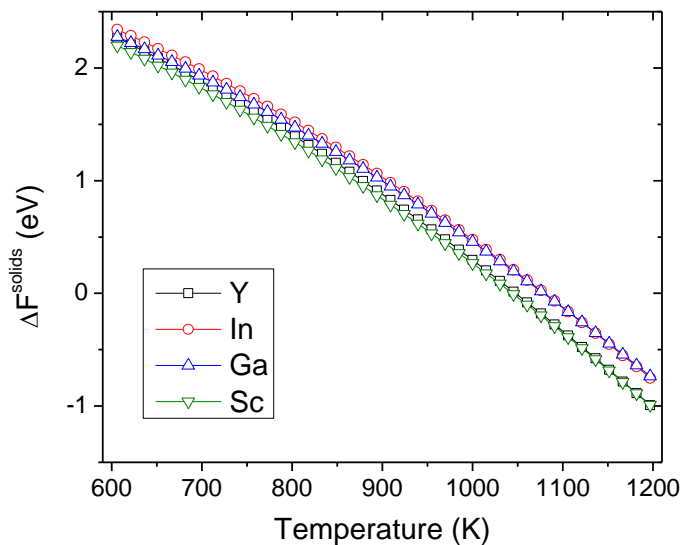
Figure 4.4: ΔF^{solids} as a function of temperature for carbonate formation reaction of $BaZrMO_{3-\delta}$, where M = Y, In, Ga, or Sc, with energy in eV and temperature in K.
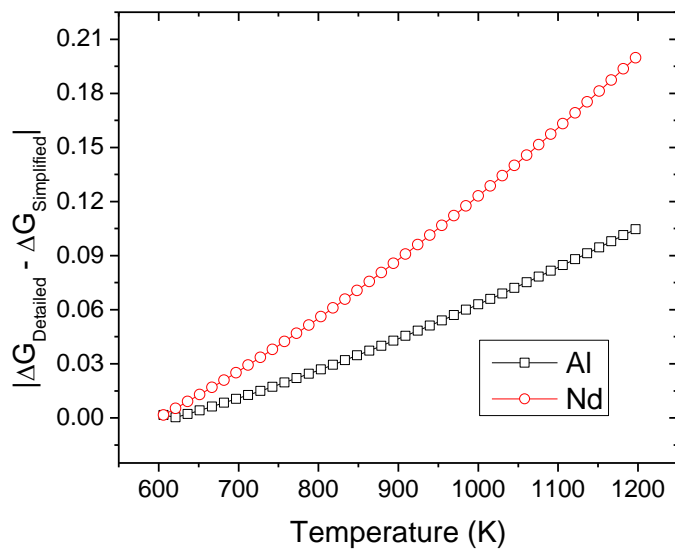
Figure 4.5: Absolute difference in free energy between the simplified and detailed models of Al and Nd doped $BaZrO_3$.

To test the predictive power of this simplified approach, we perform calculations for two additional dopants, Al and Nd, in $BaZrO_3$. For each dopant, we calculate the reaction free energy using the DFT-calculated VDOS as described above. We also estimate the reaction free energy from the DFT total energies and a correction factor determined from an average of the set of four materials in Figure 4.4. The agreement between these two kinds of calculations is shown in Figure 4.5. The simplified calculation predicts T^* for Al (Nd) doped $BaZrO_3$ to be 832 (914) K, while the detailed calculations give $T^* = 830$ (920) K. These results indicate that the simplified method introduced above can accurately predict the stability of doped $BaZrO_3$ materials.

After we validate our simplified model, we rapidly examine a large number of potential dopants using DFT total energy calculations at 0 K with the correction factor to predict the temperature dependent free energy. Data from this approach is shown in Table 4.2. From these results, we can rank the CO_2 and H_2O-stability of the trivalent dopants in $BaZrO_3$. Among the other rare earth dopants, Dy, Er, and Ho show better chemical stability with respect to CO_2 and H_2O than Y.

Table 4.2: Predicted critical temperature of $Ba_8Zr_6M_2O_{23}$ from the simplified model described in the text, with dopants ordered by increasing T* in both carbonate and hydroxide formation reaction.

Dopant (M)	T* (K) (Carbonate)	T* (K) (Hydroxide)
Ga	789	255
Sc	799	266
In	826	290
Al	832	307
Er	857	321
Ho	863	327
Tl	867	331
Dy	870	334
Y	872	336
Sm	903	368
Pm	911	375
Nd	914	379
La	932	397

4.4   Proton conductivity

To complement the information we report above regarding the CO_2 and H_2O stability of doped materials, it is important to also understand the impact of these dopants on proton conductivity. Undoped $BaZrO_3$ has been found to be chemically stable, but the material shows poor proton conductivity.[48] To keep the stability and improve proton conductivity, acceptor doped $BaZrO_3$ can be considered. Kreuer pointed out that Y doped $BaZrO_3$ has slightly higher conductivity and far better chemical stability than $BaCeO_3$-based oxides.[3] Björketun *et al.* studied the effect of dopants on proton mobility in $BaZrO_3$ using first-principles calculations and found that proton mobility is strongly related to the ionic radius of the dopant.[15] They used a jump-diffusion model to find the energy barrier for proton diffusion. Gomez *et al.* investigated the energy barrier of the proton in Y-doped $BaZrO_3$ using vertex coding methods and identified the pathways important to proton conduction.[13]

In this section, we investigate the implications for proton conductivity of a broad range of dopants not examined previously in $BaZrO_3$. For each material, we first perform DFT calculations to determine the relevant energy barriers for proton hopping in each doped material and then subsequently perform Kinetic Monte Carlo (KMC) simulations to assess the overall diffusivity of protons.

In our DFT calculations, one Zr^{4+} ion in a simulation volume of $2\times2\times2$ unit cells is replaced by a trivalent dopant M^{3+}. The dopant concentration in our system is therefore 1/8 (12.5%), which is comparable to the dopant concentration (10%) in an experiment.[13] The doped simulation box becomes charge neutral after a proton is introduced.[13] Within this volume, we identify seven (three) representative environments that define different energy barriers for proton transfer (proton rotation). These hops are listed in Table 4.3. This classification assumes that the environments associated with each hop is defined using only the nearest neighbors of the proton in its initial and final site. More involved methods exist to relax this assumption and develop more precise models for specific materials of interest.[49, 50]

We determine the energy barriers for the 10 proton hops using DFT for each of the 13 dopants doped $BaZrO_3$ we consider. These energy barriers are listed in Table 4.A.1 in Appendix 4.A. At each transition state, there are two real frequencies and one imaginary frequency when it is assumed that all atoms are fixed except the proton.

Table 4.3: Summary of the distinct transition states where a dopant is a nearest neighbor of the initial or final proton, where M = Ga, Sc, In, Al, Er, Ho, Tl, Dy, Y, Sm, Pm, Nd, or La.

	Nearest Neighbor of Initial Proton	Nearest Neighbor of Final Proton
Transfer 1	M, M	M, M
Transfer 2	M, Zr	M, Zr
Transfer 3	Zr, M	M, M
Transfer 4	M, M	M, Zr
Transfer 5	M, Zr	Zr, Zr
Transfer 6	Zr, Zr	Zr, M
Transfer 7	Zr, Zr	Zr, Zr
Rotation 1	M, M	M, M
Rotation 2	Zr, M	Zr, M
Rotation 3	Zr, Zr	Zr, Zr

The proton vibrational frequencies are used to define the hopping rate for each event of proton's movement using Harmonic Transition State Theory[23]. Here we define the prefactor (k_0) for the hopping rate as[15]

$$k_0 = \frac{1}{2\pi} \frac{v_1 \times v_2 \times v_3}{v_1^{\dagger} \times v_2^{\dagger}} \tag{4.7}$$

where v ($v^{\dagger}$) are the real vibrational frequencies related to the energy minimum (transition state).

Once the proton hopping rates are defined, we perform KMC to obtain the diffusivity of the proton in doped $BaZrO_3$. In our KMC simulations, we define a simulation volume consisting of randomly arranged atoms of the oxide at the desired composition of a trivalent dopant. The simulation volume size includes 5×5×5 unit cells. The hopping dynamics of protons are then simulated using a simple algorithm that correctly reproduces the local hopping rates.[23] At each time step a proton is randomly selected from all the protons in the simulation volume and a move direction is chosen

randomly from the two (two) possible directions available for a transfer (rotation). Hops are accepted with a probability defined by the ratio of the attempted rate and the maximum rate possible in the simulation volume. Time is incremented by $(4\ k_{fast}N_{H+})^{-1}$ regardless of the success of the attempted hop, where N_{H+} is the number of protons in the simulation volume and k_{fast} is the fastest hopping rate of all possible hops in the volume. The overall proton self diffusivity is determined using an Einstein expression relating the diffusivity to the mean square displacement.[49-51] The mean squared displacement increases linearly with time, and a diffusion coefficient is obtained from the slope.[52]

To obtain the effective activation energy for proton diffusion, we fit proton diffusivities for each dopant to

$$D = A \exp\left[-\left(\frac{E_d}{kT}\right)\right], \tag{4.8}$$

where A is a pre-exponential factor, E_d is the effective activation energy, and k is the Boltzmann constant. The effective activation energy and pre-exponential factor for proton diffusion in each doped material are listed in Table 4.4.

Table 4.4: Pre-exponential factor, effective activation energy, and ionic radius for each dopant. The materials are listed in order of increasing ionic radius.

Dopant	A $(cm^2 s^{-1})$	E_d (eV)	Effective Ionic Radius[53] (pm)
Al	1.10×10^{-5}	0.583	53.5
Ga	9.46×10^{-6}	0.522	62
Sc	6.08×10^{-5}	0.588	74.5
In	7.79×10^{-5}	0.439	80
Tl	1.48×10^{-5}	0.276	88.5
Er	2.82×10^{-5}	0.325	89
Y	1.91×10^{-5}	0.285	90
Ho	3.50×10^{-5}	0.33	90.1
Dy	2.12×10^{-5}	0.302	91.2
Sm	2.21×10^{-5}	0.29	95.8
Pm	1.56×10^{-5}	0.264	97
Nd	1.97×10^{-5}	0.282	98.3
La	1.99×10^{-5}	0.283	103.2

We find that a number of the dopants, including La, Pm, Nd, and Tl, have lower effective diffusion energy barriers than Y. Islam *et al*. pointed out that smaller dopants form stronger hydrogen bonds so that the hydroxyl-dopant association makes the diffusion of a proton more difficult.[54] This trend is followed qualitatively by our results, where dopants with larger ionic radii tend to have smaller effective diffusion activation energies.

In order to discuss proton conductivity, we need to consider not only the diffusion activation energy of protons, but also the proton concentration. The proton concentration at thermodynamic equilibrium can be expressed as[55]

$$C = N \exp\left(-\frac{E_f}{kT}\right), \tag{4.9}$$

where E_f is the formation energy of a proton and N is the number of possible proton binding sites. The proton formation energy can be defined as

$$E_f = E_M - E_{dopant-free} + Q, \tag{4.10}$$

where E_M is the lowest energy of the doped $BaZrO_3$ with a proton in the most favorable

proton binding site, and $E_{dopant-free}$ is the lowest energy of undoped BaZrO$_3$ with a proton. Q is a correction to normalize the chemical difference between the computational supercells of the two materials, defined as the difference in total energy of doped and undoped BaZrO$_3$ with a proton at a site far away from the dopant. The proton formation energy relative to the formation energy in Y-doped BaZrO$_3$ can be defined as

$$\Delta E_f = E_1 - E_2 + Q',$$ (4.11)

where E_1 is the lowest energy of a proton in Y-doped BaZrO$_3$, E_2 is the lowest energy of a proton in a M-doped BaZrO$_3$, and Q' is a correction to normalize the chemical difference between the computational supercells of the two materials defined by taking the difference of the total energy of proton between the Y- and M-doped materials in a site far away from the dopant.

Proton conductivity is the product of the proton charge (z), the Faraday constant (F, C mol^{-1}), the concentration of protons (C_{H^+}, mol cm^{-3}), and the proton mobility (μ_{H^+}, cm^{2}s^{-1}V^{-1}),[56]

$$\sigma_{H^+} = zFC_{H^+}\mu_{H^+}$$ (4.12)

If proton mobility is described by the Nernst-Einstein relationship,[57]

$$\mu_{H^+} = \frac{zFD}{RT},$$ (4.13)

where D is proton diffusivity, then the proton conductivity can be defined by

$$\sigma_{H^+} = \frac{z^2F^2}{RT}DC_{H^+}.$$ (4.14)

In comparing a variety of materials, it is convenient to focus on the ratio of proton conductivities rather than the absolute quantity. The ratio of the proton conductivities for two materials is

$$\frac{\sigma_1}{\sigma_2} = \frac{C_1}{C_2}\frac{D_1}{D_2} = \frac{N_1}{N_2}\frac{A_1}{A_2}\exp\left[-\frac{(\Delta E_f + \Delta E_d)}{kT}\right]. \tag{4.15}$$

Since stoichiometries of the materials with different dopants are the same, $N_1/N_2 = 1$. Equation (4.15) defines the relative proton conductivities of all the doped materials we consider expressed directly in terms of quantities that we determine from our DFT-based calculations. With the convention that the subscript 1 refers to the Y-doped material, when σ_1/σ_2 is larger (smaller) than 1, using Y as a dopant yields a higher (lower) conductivity than material 2. Our results for the full set of doped materials we consider are summarized in Table 4.5. A striking observation from Table 4.5 is that the relative proton conductivities among the doped materials vary by several orders of magnitude relative to the Y-doped material at 600 K. The variation in σ_1/σ_2 diminishes at higher temperatures. For example, at 1000 K, σ_1/σ_2 is 0.003 for La and 1155 for Sc.

Table 4.5: Summary of the proton conductivity of M-doped materials relative to Y-doped $BaZrO_3$ (σ_1/σ_2) at T = 600 K. All energies are shown in eV.

M	ΔE_f	ΔE_d	A_1/A_2	σ_1/σ_2
La	0.487	0.002	0.956	7.5×10^{-5}
Nd	0.320	0.002	0.970	0.002
Pm	0.255	0.021	1.225	0.006
Sm	0.206	-0.005	0.862	0.017
Tl	0.087	0.008	1.290	0.202
Dy	0.008	-0.017	0.900	1.072
Ho	-0.033	-0.046	0.544	2.496
Er	-0.076	-0.040	0.676	6.376
Al	0.209	-0.299	1.740	9.823
In	-0.315	-0.154	0.245	2134
Ga	-0.220	-0.237	2.015	13816
Sc	-0.405	-0.303	0.314	2.8×10^{5}

Our results in Tables 4.2 and 4.5 rank the chemical stabilities of the doped

materials as Ga > Sc > In > Al > Er > Ho > Tl > Dy > Y > Sm > Pm > Nd > La while the rank for proton conductivity at 600 K is La > Nd > Pm > Sm > Tl > Y > Dy > Ho > Er > Al > In > Ga > Sc, respectively. The ranking changes slightly at higher temperatures due to variations in the diffusion prefactors, but these changes are minor. Since the ratio of the diffusion prefactors varies only moderately, we focus on the diffusion energy barrier and relative formation energy to characterize the contributions of mobility and concentration to the overall conductivity.

To describe the relative contributions of the formation and diffusion energies, we define the following quantities for the data in Table 4.5:

$$Formation\ Energy\ Contribution: \frac{|E_f|}{|E_d|+|E_f|} \times 100\ (\%) \qquad (4.16)$$

$$Diffusion\ Contribution: 100 - Formation\ Energy\ Contribution\ (\%) \qquad (4.17)$$

These quantities are listed in Table 4.6 using the undoped material as the reference material. Table 4.6 shows that proton formation energy plays a larger role than the proton diffusion except the materials doped with In or Sc. Interestingly, the five materials that have larger formation energy contributions than Y are the only doped materials that are predicted to have better proton conductivity than Y in Table 4.5.

Table 4.6: The contribution of formation energy and diffusion to the results in Table 4.5, using undoped $BaZrO_3$ as the reference material.

Dopant	Diffusion (%)	Formation (%)
Al	38	62
Dy	28	72
Er	32	68
Ga	49	51
Ho	31	69
In	50	50
La	18	82
Nd	21	79
Pm	21	79
Sc	62	38
Sm	23	77
Tl	25	75
Y	27	73

It is useful to explore the physical origin of the trends seen in our calculations. Previously, Kreuer *et al*. proposed that the ionic radius of a dopant, the electronegativities of the cations, and the corresponding acid or base properties are important for the mobility of protons in perovskites.[10, 54] To examine the physical background behind the net energy barrier for proton conductivity and the critical temperature for carbonate formation, we investigate the relationships between these properties and the Pauling electronegativity of the dopant and the ionic radius of the dopant. These relationships are shown in Figures 4.6 and 4.7, respectively.
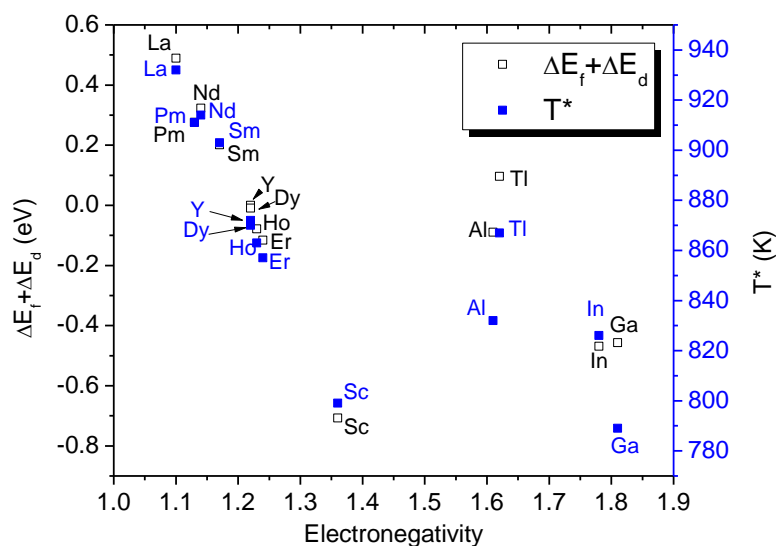
Figure 4.6: The relationships between $\Delta E_f + \Delta E_d$ (eV), critical temperature, and the Pauling electronegativity[58] of the dopants we studied.

Laidoudi *et al*. found that proton conductivity decreases in Er, Ho, Tm, Yb, and Y doped materials as the electronegativity increases up to the electronegativity of 1.4.[59] The decrease of the difference in electronegativity between A- and B-site cations in ABO_3–type perovskites increases the proton concentration since the hydration enthalpy becomes more negative.[59] Ba (the A-site cation) has a Pauling electronegativity of 0.89, and Zr (the B-site cation) has a Pauling electronegativity of 1.33. This suggests that dopants that are closer in electronegativity to Ba have better proton conductivity due to increased proton concentration. The results in Figure 4.6 agree with this description since $\Delta E_f + \Delta E_d$ decreases as the dopant electronegativity increases for dopants less electronegative than Zr. Four of the five dopants with the highest proton conductivities, Sm, Nd, La, and Pm, fall into this category. Kreuer *et al.* found that higher dopant electronegativity leads to the high stability.[3] Liu *et al*. found that there was no carbonate

formation reaction in their XRD studies after they introduced 10% of Nb in BaCe$_{0.8}$Sm$_{0.2}$O$_{3-\delta}$.[60] They concluded that the higher electronegativity of Nb decreases the basicity of BaCe$_{0.8}$Sm$_{0.2}$O$_{3-\delta}$ and restrains the reaction with CO$_2$. In other words, after the system has the adequate acidity, it enhances the chemical stability with respect to the carbonate formation reaction. This trend can also be seen in our results for dopants with electronegativities less than Zr in Figure 4.6. Thus, the materials with smaller electronegativity than Zr show a relatively simple relationship between electronegativity and both proton conductivity and chemical stability. The results in Figure 4.6, however, show that no such simple relationship exists for dopants whose electronegativities are higher than Zr.
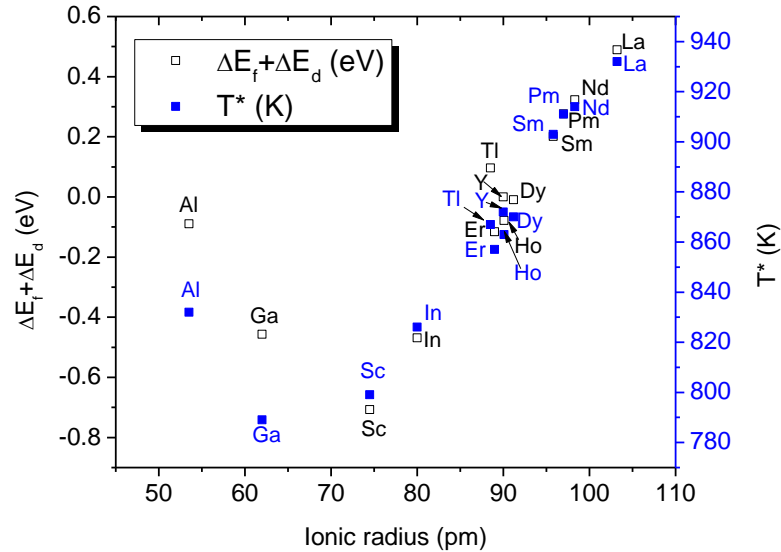
Figure 4.7: Critical temperature T* (K) and $\Delta E_f + \Delta E_d$ (eV) as a function of the ionic radius (pm) of dopants in doped BaZrO$_3$.

The critical temperature for carbonate formation and the net energy associated with proton mobility, $\Delta E_f + \Delta E_d$, is shown as a function of the dopant ionic radius in

Figure 4.7.[53] Apart from Al- and Ga-doped materials, both quantities increase as the ionic radius of the dopant increases. This means proton conductivity increases as ionic radius increases but this also results in reduced chemical stability. This observation is consistent with previous experimental observations. Islam *et al.* found that larger dopants have weaker binding energy for hydroxyl-dopant pairs. Specifically, they found a stronger dopant-OH association in Sc-doped $BaZrO_3$ (small ionic radius dopant case) than in In or Y doped $BaZrO_3$ (large ionic radius dopant case).[61] Matsumoto *et al.* examined the chemical stability of $BaCeO_3$ with various trivalent dopants with thermogravimetry (TG) and found that the critical temperature decreases with decreasing ionic size of the dopants and emphasized that chemical stability is affected by the size of the dopants.[62]
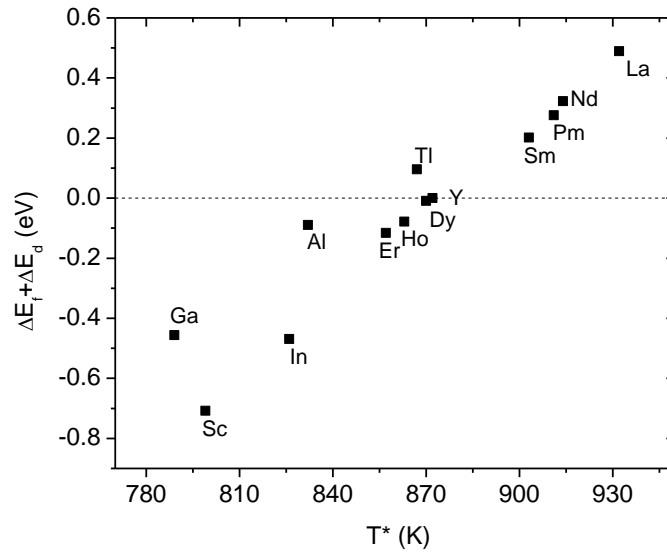
Figure 4.8: $\Delta E_f + \Delta E_d$ (eV) as a function of critical temperature T* (K) of dopants in doped $BaZrO_3$.

A central goal of our calculations is to examine whether there are dopants for $BaZrO_3$ that enhance both its chemical stability and proton conductivity. This issue can

be examined using Figure 4.8, which plots $\Delta E_f + \Delta E_d$ as a function of T* for the complete set of materials we examine. For almost all of the materials, a simple tradeoff is evident in which improvements in chemical stability (lower T*) corresponds to lower proton conductivity as characterized by $\Delta E_f + \Delta E_d$. The only exceptions to this trend are Ga or Al-doped $BaZrO_3$. The existence of the simple tradeoff depicted in Figure 4.8 indicates that the choice of dopant for a particular application should be dictated by the relative importance given to chemical stability and proton conductivity.

4.5   Conclusion

We use efficient DFT-based modeling to systematically investigate potentially promising dopants in terms of their chemical stability and proton conductivity in $BaZrO_3$. Our work expands the range of materials for which information on chemical stability with respect to carbonate and hydroxide formation reaction and comparison of proton conductivity of the various dopants is available.

Our models identify the small number of dopants that are known from prior experiments and simulations to enhance proton conductivity relative to the other dopants and also identify several new dopants with this property. Since we examine many dopants in our calculations, our results may be utilized to explore the physical origins of the trends in chemical stability and proton mobility among different dopants. We explore physical relationships between chemical stability and proton conductivity and how these are correlated with the ionic radius and electronegativity of each of dopant. One major conclusion is that there is a simple tradeoff between chemical stability and proton conductivity in doped $BaZrO_3$. Improvements in one property cause a decreased

performance in the other. This indicates that choice of an appropriate dopant must be

made based on the relative importance of the two properties for a given application.

4.6 References

1. Iwahara, H., Esaka, T., Uchida, H., Maeda, N., *Solid State Ionics* **1981**, 3-4, 359.
2. Iwahara, H., *Solid State Ionics* **1992**, 575-586.
3. Kreuer, K. D., *Annu. Rev. Mater. Res.* **2003**, 33, 333.
4. Gomez, M.A., Jindal, S., Fletcher, K. M., Foster, L. S., Addo, N. D. A., Valentin, D., Ghenoiu, C., Hamilton. A., *J. Chem. Phys.* **2007**, 126, 19.
5. Kreuer, K. D., Dippel, T., Hainovsky, N. G., Maier, J., *Ber. Bunsen. Phys. Chem.* **1992**, 96, 1736.
6. Norby, T., Proton conductivity in perovskite oxides, in Perovskite oxide for solid oxide fuel cells, Springer, 2009, 217.
7. Kreuer, K. D., *Solid State Ionics* **1999**, 125, 285.
8. Uchida, H., Ogaki, K., Iwahara, H., *J. Electrochem. Soc.* **1987**, 134, C522.
9. Iwahara, H., Uchida, H., Yamasaki, I., *Int. J. Hydrogen Energy* **1987**, 12, 73.
10. Kreuer, K. D., Adams, S., Munch, W., Fuchs, A., Klock, U., Maier, J., *Solid State Ionics* **2001**, 145, 295.
11. van Duin, A. C. T., Merinov, B. V., Han, S. S., Dorso, C. O., Goddard, W. A., *J. Phys. Chem. A* **2008**, 112, 11414.
12. Bork, N., Bonanos, N., Rossmeisl, J., Vegge, T., *Phys. Rev. B* **2010**, 82, 1.
13. Gomez, M. A., Chunduru, M., Chigweshe, L., Foster, L., Fensin, S. J., Fletcher, K. M., Fernandez, L. E., *J. Chem. Phys.* **2010**, 132, 21.
14. Gomez, M. A., Chunduru, M., Chigweshe, L., Fletcher, K. M., *J. Chem. Phys.* **2010**, 133, 6.
15. Bjorketun, M. E., Sundell, P. G., Wahnstrom, G., *Phys. Rev. B* **2007**, 76, 054307.
16. Sundell, P. G., Bjorketun, M. E., Wahnstrom, G., *Phys. Rev. B* **2007**, 76, 094301.
17. Bjorketun, M. E., Sundell, P. G., Wahnstrom, G., *Faraday Discuss.* **2007**, 134, 247.
18. Islam, M. S., Davies, R. A., Gale, J. D., *Chem. Commun.* **2001**, 7, 661.
19. Islam, M. S., Davies, R. A., Gales, J. D., *Chem. Mater.* **2001**, 13, 2049.
20. Shimojo, F., Hoshino, K., *Solid State Ionics* **2001**, 145, 421.
21. Zhang, Q. F., Wahnstrom, G., Bjorketun, M. E., Gao, S. W., Wang, E. G., *Phys. Rev. Lett.* **2008**, 101, 215902.
22. Ryu, K. H., Haile, S. M., *Solid State Ionics* **1999**, 125, 355.
23. Sholl, D. S., Steckel, J. A., Density Functional Theory: A Practical Introduction (Wiley, Hoboken, NJ, 2009).
24. Perdew, J. P., Chevary, J. A., Vosko, S. H., Jackson, K. A., Pederson, M. R., Singh, D. J., Fiolhais, C., *Phys. Rev. B* **1992**, 46, 6671.
25. Kresse, G., Hafner, J., *Phys. Rev. B* **1993**, 47, 558.
26. Kresse, G., Furthmüller, J., J., *Phys. Rev. B* **1996**, 54, 11169.
27. Vanderbilt, D., *Phys. Rev. B* **1990**, 41, 7892.

28. Kresse, G., Joubert, D., *Phys. Rev. B* **1999**, 59, 1758.
29. Monkhorst, H. J., Pack, J. D., *Phys. Rev. B* **1976**, 13, 5188.
30. The Inorganic Crystal Structure Database (ICSD). The Inorganic Crystal Structure Database (ICSD) http://www.fiz-informationsdienste.de/en/DB/icsd/.
31. Alapati, S. V., Johnson, J. K., Sholl, D. S., *J. Phys. Chem. C* **2008**, 112, 5258.
32. Akbarzadeh, A. R., Wolverton, C., Ozolins, V., *Phys. Rev. B* **2009**, 79, 184102
33. Parlinski, K. Software PHONON, 2005.
34. Ackland, G. J., *J. Phys.: Condens. Matter* **2002**, 14, 2975.
35. Mortimer, R. G., Physical Chemistry. 2nd ed., (Academic Press, New York, 2000).
36. Chase, M. J. W., *J. Phys. Chem. Ref. Data Monogr.* **1998**, 9, 1.
37. Hao, S. Q., Sholl, D. S., *Energy Environ. Sci.* **2008**, 1, 175.
38. Hao, S. Q., Widom, M., Sholl, D. S., *J. Phys.: Condens. Matter* **2009**, 21, 11.
39. Hao, S. Q., Sholl, D. S., *J. Membr. Sci.* **2011**, 381, 192.
40. Jacob, K. T., Waseda, Y., *Metall. Mater. Trans. B* **1995**, 26, 775.
41. Alapati, S. V., Johnson, J. K., Sholl, D. S., *J. Alloys Compd.* **2007**, 446, 23.
42. Kreuer, K. D., Munch, W., Ise, M., He, T., Fuchs, A., Traub, U., Maier, J., *Ber. Bunsen. Phys. Chem.* **1997**, 101, 1344.
43. Kim, K. C., Sholl, D. S., *J. Phys. Chem. C* **2010**, 114, 678.
44. Chamberlain, J. W., Hunten, D. M., Theory of Planetary Atmospheres: An Introduction to Their Physics and Chemistry (Academic Press, San Diego, 1987).
45. Uda, T., Babilo, P., Haile, S. M., "Thermodynamic Analysis and Conductivity of Yttrium Doped Barium Zirconate"; Ninth International Symposium on Solid Oxide Fuel Cells, The Electrochemical Society 207th Meeting, Quebec City, Canada, 2005.
46. Zhao, F., Liu, Q., Wang, S. W., Brinkman, K., Chen, F. L., *Int. J. Hydrogen Energy* **2010**, 35, 4258.
47. Alapati, S. V., Johnson, J. K., Sholl, D. S., *Phys. Rev. B* **2007**, 76, 104108.
48. Zhong, Z. M., *Solid State Ionics* **2007**, 178, 213-220.
49. Kang, S. G., Coulter, K. E., Gade, S. K., Way, J. D., Sholl, D. S., *J. Phys. Chem. Lett.* **2011**, 2, 3040.
50. Semidey-Flecha, L., Sholl, D. S., *J. Chem. Phys.* **2008**, 128, 144701.
51. Kamakoti, P., Sholl, D. S., *Phys. Rev. B* **2005**, 71, 014301.
52. Frenkel, D., Smit, B., Understanding Molecular Simulation: From Algorithms to Applications (Academic Press, San Diego, 2002).
53. Shannon, R. D., *Acta Crystallogr., Sect. A* **1976**, 32, 751.
54. Munch, W., Kreuer, K. D., Adams, S., Seifert, G., Maier, J., *Phase Transitions* **1999**, 68, 567.
55. Janotti, A., Van de Walle, C. G., Phys. Rev. B 2007, 76, 165202.
56. Norby, T., Larring, Y., *Curr Opin Solid State Mater Sci.***1997**, 2, 593.
57. Bard, A. J., Inzelt, G., Scholz, F., Electrochemical Dictionary (Springer, Heidelberg, 2012).
58. http://www.webelements.com.
59. Laidoudi, M., Talib, I. A., Omar, R., *J. Phys. D: Appl. Phys.* **2002**, 35, 397.
60. K Xie, K., Yan, R. Q., Chen, X. R., Dong, D. H., Wang, S. L., Liu, X. Q., Meng, G. Y., *J. Alloys Compd.* **2009**, 472, 551.

61. Islam, M. S., Stokes, S. J., *J. Mater. Chem.* **2010**, 20, 6258.
62. Matsumoto, H., Kawasaki, Y., Ito, N., Enoki, M., Ishihara, T., Electrochem. *Solid-State Lett.* **2007**, 10, B77.

Table 4.A.1 shows the energy barriers determined using DFT for all 10 proton hops in B-site doped $BaZrO_3$ for each of the 13 dopants we consider.

Table 4.A.1: Energy barriers (in eV) of the proton in the case where a dopant is a nearest neighbor of the initial or final proton, where M = Y, Er, Ho, Al, Ga, Dy, In, Sc, La, Nd, Pm, Sm, or Tl.

	Y	Er	Ho	Al	Ga	Dy	In	Sc	La	Nd	Pm	Sm	Tl
Transfer 1	0.98	0.74	0.84	0.64	0.41	0.95	0.56	0.28	2.18	1.94	1.72	1.58	1.46
Transfer 2	0.35	0.32	0.33	0.18	0.21	0.34	0.30	0.22	0.53	0.48	0.45	0.40	0.40
Transfer 3	0.55	0.44	0.48	0.45	0.08	0.53	0.34	0.13	1.57	1.31	1.13	0.77	0.89
Transfer 4	0.59	0.52	0.55	0.69	0.37	0.57	0.49	0.39	1.11	1.04	0.92	0.70	0.90
Transfer 5	0.40	0.40	0.40	0.80	0.72	0.40	0.45	0.57	0.61	0.54	0.46	0.45	0.49
Transfer 6	0.39	0.33	0.36	0.06	0.12	0.38	0.28	0.18	0.77	0.65	0.56	0.53	0.51
Transfer 7	0.29	0.29	0.29	0.29	0.29	0.29	0.29	0.29	0.29	0.29	0.29	0.29	0.29
Rotation 1	0.84	0.68	0.75	0.30	0.16	0.84	0.46	0.13	2.48	2.10	1.31	1.23	1.38
Rotation 2	0.11	0.12	0.11	0.17	0.17	0.47	0.14	0.17	0.08	0.07	0.07	0.07	0.61
Rotation 3	0.15	0.15	0.15	0.15	0.15	0.15	0.15	0.15	0.15	0.15	0.15	0.15	0.15

CHAPTER 5

A-SITE DOPED AND

(A, B)-SITE DOPED BARIUM ZIRCONATE

5.1   Introduction

Ceramic materials are important for applications as electrolytes in Solid Oxide Fuel Cells (SOFC) and high temperature proton conductors (HTPCs) for tritium separation.[1-5] Solid oxide proton-conducting electrolytes have been considered for SOFCs. These electrolytes can decrease the operation temperature to 500-700 °C from 800-1000 °C, the temperature required for oxygen ion conductors.[1-4] In the tritium separation application, sequestration of trace levels of tritium from Next Generation Nuclear Plant (NGNP) cooling systems is a significant challenge, since tritium is a radioactive fission product.[5] One potential way for separating tritium from exhaust gas streams is to use a proton conductor as a membrane.[6]

Basicity has been considered as an important factor influencing proton conductivity, since this is related to the affinity for protons.[7] Doping a monovalent alkali metal on the A-site in $BaZrO_3$ causes the creation of oxygen vacancies for charge neutrality.[7] Additionally, this kind of alkali doping increases the basicity of the perovskite, enhancing the H_2O uptake capacity of the material, and indirectly the proton conductivity.[8] The key objective of this study is to investigate the effect of alkali metal doping on the stability and proton conductivity in $BaZrO_3$. The results of chemical stability and proton conductivity are compared with those of Y-doped $BaZrO_3$.

In this chapter, we use efficient computational methods to examine possible A-site monovalent dopants (K, Rb, and Cs), and the combination of these A-site monovalent dopants and B-site trivalent dopants. We choose Y as a representative of a trivalent dopant. The chemical stability of K-doped $BaZrO_3$ is reduced due to the presence of Y. However, the introduction of Y improved proton conductivity. One of the main conclusions from our calculations is that there is a simple linear relationship between chemical stability and proton conductivity in A-site doped $BaZrO_3$. Chemical stability becomes lower and proton conductivity becomes higher due to the addition of Y dopant in A-site doped $BaZrO_3$.

We find that K-doped $BaZrO_3$ shows the highest proton conductivity and chemical stability among the other A-site doped $BaZrO_3$ we investigate. Because the formation energy is an important component for proton conductivity, we study the relative formation energy for a wide range of pairs of K and B-site dopants (M_2, where M_2 = In, Ga, Sc, Nd, Al, Tl, Sm, Dy, La, Pm, Er, or Ho) to find the promising dopant pairs that may give high proton conductivity. The chemical stability of these pairs should also be considered for dopants to be attractive. However, the dopant pairs introduce more chemical instability than one dopant (at either A-site or B-site) in $BaZrO_3$.

5.2 Calculation methods

Plane wave DFT calculations are performed for 0 K total energies of each compound with the Vienna *ab initio* Simulation Package (VASP).[9, 10] For calculating the DFT total energy of each material we use the projector augmented wave (PAW) method to describe the core electrons of each atom. Electron exchange and correlation effects are

described using the generalized gradient approximation (GGA) with the Perdew-Wang 91 (PW91) functional.[9-12]

The energy cutoff for total energy calculations is 500 eV for all compounds. *k*-points are obtained using the Monkhorst–Pack method[13] with the number of *k*-points chosen to give a spacing of about 0.028 Å^{-1} along the axes of the reciprocal unit cells.

Experimental structures reported in the Inorganic Crystal Structure Database (ICSD) are used to start geometry optimization (the lattice parameters and atomic positions) in DFT calculations.[14] Geometry relaxations are done using a Conjugate Gradient algorithm until the forces on all unconstrained atoms are less than 0.03 eV/Å.

Additionally, we compute the temperature-dependent free energy of each solid for our studies of chemical stability. Calculations of the phonon density of states and the resulting vibrational contributions to the free energy for each material involved in a reaction are performed using the PHONON code implemented by Parlinski.[15] A displacement magnitude of 0.03 Å is chosen. The free energy of reaction at finite temperature, $\Delta G(T)$, can be computed within the harmonic approximation once the vibrational density of states for the material is known.[16] It is assumed that $\Delta(PV)_{solids} \ll (PV)_{CO_2}$. We treat gaseous CO_2 as an ideal gas. The free energies of CO_2 are taken from standard statistical mechanics as[17]

$$G_{CO2} = \frac{7}{2}RT + \sum_{i=1}^{4} \frac{N_a h v_i}{e^{h v_i/kT}-1} - TS_{CO2}(T) \,, \tag{5.1}$$

where N_a is Avogadro's constant, R is the universal gas constant, T is temperature, and v_i are the vibrational frequencies of CO_2 in G_{CO2}. The entropy of CO_2 is accurately obtained by the Shomate equation.[18]

Instead of performing Nudged Elastic Band (NEB) calculations, which were used in other theoretical studies to find the transition states for proton transfer and rotation, an efficient way to find the transition states is used. When the initial estimated proton position at a transition state is close enough to its true value, this position tends toward the saddle point during a quasi-Newton optimization. Vibrational frequency calculations of proton are performed to determine whether the geometry optimization converges to a correct transition state instead of a local minima site on the energy surface. A saddle point of the energy surface gives two real frequencies and one imaginary frequency, when only the proton's degrees of freedom are considered.

5.2.1 DFT calculated results of geometry optimization

For each compound we considered, the lattice parameters and atomic positions are optimized using DFT calculations with a single unit cell starting from the experimental structures listed in the ICSD.[14] We study a single step decomposition mechanism for perovskites in the presence of CO_2. By assuming that the increase of partial pressure of CO_2 is low during the process, we are able to neglect subsequent decomposition reactions. The optimized lattice constants for each compound considered in this work are presented in Table 5.1 along with the corresponding experimental data. Predicted values agree to experimental lattice constants and angles, apart from Cs_2O, although calculated lattice constants by GGA functional are slightly larger than experimental lattice constants.

Table 5.1. Comparison of the experimental[14] and the DFT calculated structural parameters for the 7 crystalline compounds considered in our calculations, with all lengths in Å and angles in degrees.

Compound	Space group	Structural Parameters (Å, degree)	
		Experimental	Calculated
ZrO_2	$P12_1/c1$	$a = 5.143$ $b = 5.204$ $c = 5.310$ $\beta = 99.166$	$a = 5.212$ $b = 5.286$ $c = 5.386$ $\beta = 99.574$
K_2O	$Fm\text{-}3m$	$a = 6.436$	$a = 6.450$
Rb_2O	$Fm\text{-}3m$	$a = 6.756$	$a = 6.849$
Cs_2O	$R\text{-}3mH$	$a = 4.256$ $c = 18.990$ $\gamma = 120$	$a = 4.246$ $c = 21.650$ $\gamma = 120$
Y_2O_3	$Ia\text{-}3$	$a = 10.611$	$a = 10.694$
$BaZrO_3$	$Pm\text{-}3m$	$a = 4.188$	$a = 4.252$
$BaCO_3$	$Pnma$	$a = 6.434$ $b = 5.315$ $c = 8.904$	$a = 6.582$ $b = 5.364$ $c = 9.003$

5.3   Chemical stability

The carbonate formation reactions of M_1-doped and (M_1,M_2)-doped $BaZrO_3$ in the presence of CO_2 can be described as

$$Ba_{0.75} (M_1)_{0.25}Zr\, O_{3-\delta} + CO_2 \leftrightarrow 0.75\, BaCO_3 + ZrO_2 + 0.125\, (M_1)_2O \, , \quad (5.2)$$

$$Ba_{0.75} (M_1)_{0.25}Zr_{0.75}(M_2)_{0.25}O_{3-\delta} + CO_2 \leftrightarrow 0.75\, BaCO_3 + 0.75\, ZrO_2 + 0.125\, (M_1)_2O +$$
$$0.125\, (M_2)_2O_{3,}$$
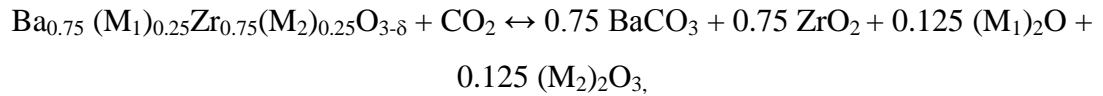
where M_1 is a monovalent dopant, either K, Rb, or Cs, and M_2 is a trivalent dopant such as Y.

We examine the chemical stability of three alkali dopants, K, Rb, and Cs, in $BaZrO_3$. With the introduction of dopants, oxygen vacancies are formed to ensure charge neutrality.[19] The net stoichiometry of the doped materials is $Ba_6(M_1)_2Zr_8O_{23}$, corresponding to a dopant concentration of 2/8 (25%). Our calculations for doped $BaZrO_3$ employ $2\times2\times2$ unit cells in the computational supercell, so each supercell

contains two dopant atoms and O vacancy. Upon creating O vacancies in the supercell, subsequent calculations consider various placements of the dopant atoms. For K, Rb, and Cs, the lowest energy state has two dopant atoms placed next to each other. We extend our calculations to materials doped with M_2^{3+} at the Zr site and doped with M_1^{3+} at the Ba site. Our calculations use a M_1 dopant concentration of 2/8 (25%), and M_2 dopant concentration of 2/8 (25%) so the net stoichiometry of the doped materials is $Ba_6(M_1)_2Zr_6(M_2)_2O_{22}$. Each supercell contains two M_1 dopants, two M_2 dopants, and two oxygen vacancies. Likewise, the lowest energy arrangement is employed in the VDOS calculation.

It is required to consider the configurational entropy of disordered M^{3+} and oxygen vacancies to compute the free energy of doped materials.[20] The configurational entropy comes from the Boltzmann definition of entropy, $S = k\ln\Omega$, where Ω is the number of configurations of dopants and vacancies possible.[21] We assume all orderings of dopants and vacancies are equally likely. This offers a configurational entropy for $Ba_{0.75}(M_1)_{0.25}ZrO_{3-\delta}$ of 54.1 J K^{-1} mol^{-1} and for $Ba_{0.75}(M_1)_{0.25} Zr_{0.75}(M_2)_{0.25}O_{3-\delta}$ of 102.1 J K^{-1} mol^{-1}. Small energy differences between many configurations lead to an overestimation of the true configurational entropy, but this effect is not explored further. The equilibrium CO_2 pressure related to carbonate formation of undoped and doped $BaZrO_3$, as predicted by our calculations, is shown in Figure 5.1, using $P_0 = 1$ bar. We refer to the temperature at which carbonate formation becomes favorable as T*. We provide results at a CO_2 pressure of 1 bar, as every material examined depends on CO_2 pressure in an identical manner.
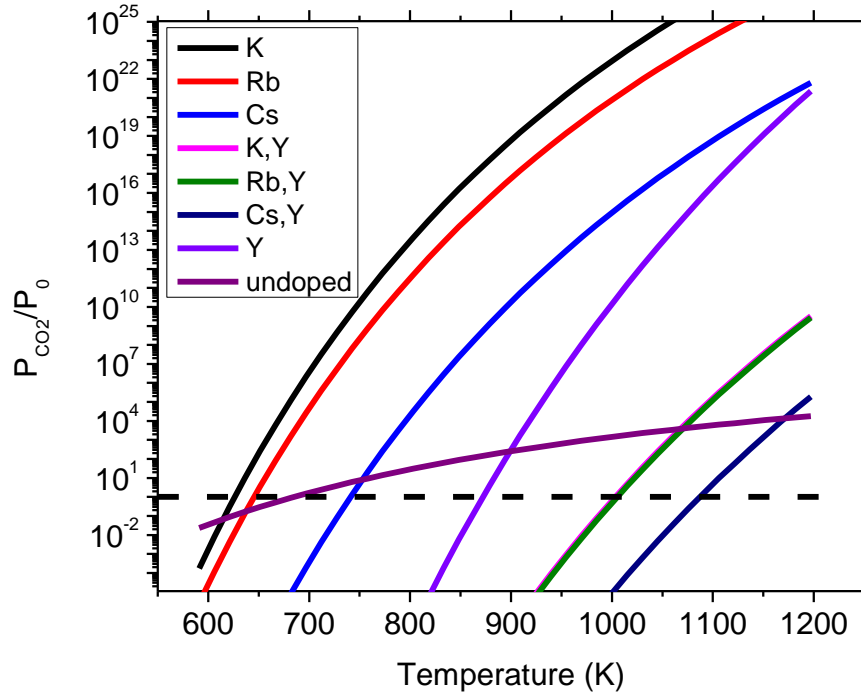
Figure 5.1: van't Hoff plot for the carbonate formation reaction of undoped $BaZrO_3$, $BaZrO_3 + CO_2 \leftrightarrow BaCO_3 + ZrO_2$ and doped materials, $Ba_6(M_1)_2Zr_8O_{23} + 6CO_2 \leftrightarrow 6BaCO_3 + 8ZrO_2 + (M_1)_2O$ for M_1 = K, Rb, or Cs. Also shown are results for $Ba_8Zr_6Y_2O_{23} + 8CO_2 \leftrightarrow 8BaCO_3 + 6ZrO_2 + Y_2O_3$, and $Ba_6(M_1)_2Zr_6Y_2O_{22} + 6CO_2 \leftrightarrow 6BaCO_3 + 6ZrO_2 + (M_1)_2O + Y_2O_3$ for M_1 = K, Rb, or Cs. The horizontal dashed line refers to $P_{CO2}/P_0 = 1$.
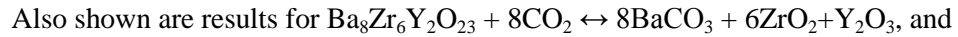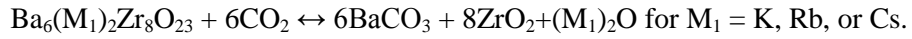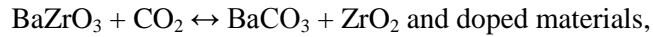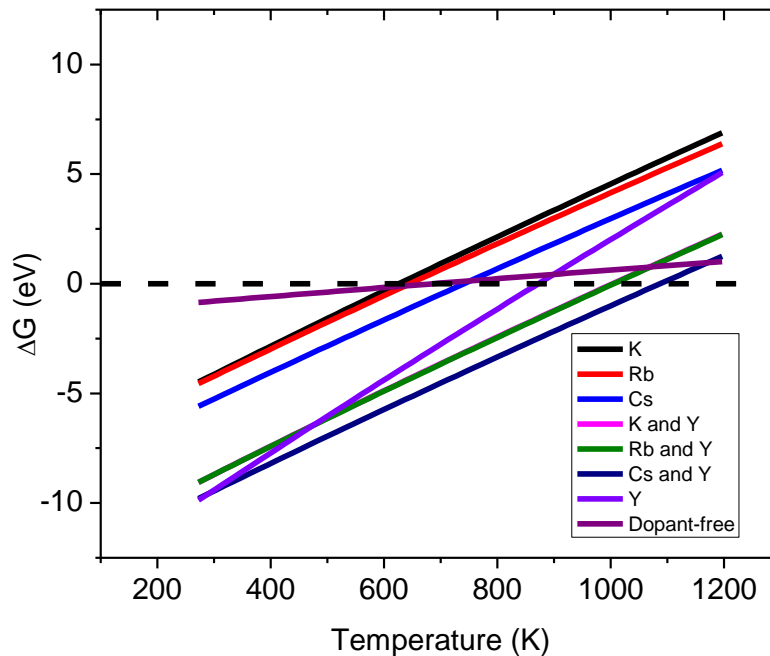
Figure 5.2: Free energy of reaction, ΔG, as a function of temperature for carbonate formation reactions. The undoped material is shown using diamonds for the reaction $BaZrO_3 + CO_2 \leftrightarrow BaCO_3 + ZrO_2$. The results for the doped materials correspond to the reaction $Ba_6(M_1)_2Zr_8O_{23} + 6CO_2 \leftrightarrow 6BaCO_3 + 8ZrO_2 + (M_1)_2O$ for M_1 = K, Rb, or Cs. Also shown are results for $Ba_8Zr_6Y_2O_{23} + 8CO_2 \leftrightarrow 8BaCO_3 + 6ZrO_2 + Y_2O_3$, and the reaction $Ba_6(M_1)_2Zr_6Y_2O_{22} + 6CO_2 \leftrightarrow 6BaCO_3 + 6ZrO_2 + (M_1)_2O + Y_2O_3$ for M_1 = K, Rb, or Cs.

Figure 5.2 shows a stability diagram for the doped materials we examine at a CO_2 pressure of 1 bar. The rank of chemical stability of M_1-doped $BaZrO_3$ and (M_1,Y)-doped $BaZrO_3$ with respect to CO_2 is K ($T^* = 630$ K) > Rb ($T^* = 646$ K) > Cs ($T^* = 741$ K) > Y ($T^* = 875$ K) > (K,Y) ($T^* = 1003$ K) > (Rb,Y) ($T^* = 1005$ K) > (Cs,Y) ($T^* = 1084$ K). For undoped $BaZrO_3$, the calculated value of T^* is 688 K when P_{CO2} is 1 bar. Only K and Rb-doped materials show a lower critical temperature (that is, higher chemical stability) than the undoped material.

Table 5.2: Critical temperature for each dopant. The materials are listed in order of increasing critical temperature. The differences of critical temperature between (M_1,Y)-doped $BaZrO_3$ and M_1-doped $BaZrO_3$ for M_1 = K, Rb, or Cs.

Dopant (M_1)	T* (K)	Dopant (M_1,Y)	T* (K)	Δ (T*(M_1,Y) - T*(M_1)) (K)
K	630	(K,Y)	1003	373
Rb	646	(Rb,Y)	1005	359
Cs	741	(Cs,Y)	1084	343

Table 5.3: Critical temperature for undoped and doped $BaZrO_3$.

Dopant (M_1)	T* (K)
Undoped	688
K	630
Y	872
(K,Y)	1003

The differences of critical temperature between (K,Y)-doped $BaZrO_3$ and K-doped $BaZrO_3$, between (Rb,Y)-doped $BaZrO_3$ and Rb-doped $BaZrO_3$, and between (Cs,Y)-doped $BaZrO_3$ and Cs-doped $BaZrO_3$ are 373, 359, and 343 K, respectively, as seen in Table 5.2. When we introduce Y in M_1-doped $BaZrO_3$, the chemical stability with respect to carbonate formation reaction becomes lower than M_1-doped $BaZrO_3$. Although K-doped and Rb-doped $BaZrO_3$ show better chemical stability than undoped $BaZrO_3$, (K,Y)-doped and (Rb,Y)-doped $BaZrO_3$ show lower chemical stability than Y-doped $BaZrO_3$. As shown in Table 5.3, we find that the critical temperature of (K,Y)-doped $BaZrO_3$ cannot be extrapolated from the critical temperature of K-doped $BaZrO_3$ and Y-doped $BaZrO_3$, because the critical temperature of (K,Y)-doped $BaZrO_3$ is not between the critical temperatures of K- and Y-doped $BaZrO_3$.

5.4 Proton conductivity

Proton conductivity is highly dependent upon dopant types. Undoped $BaZrO_3$ is

chemically stable, but exhibits low proton conductivity.[22] To maintain chemical stability and enhance proton conductivity, acceptor doped $BaZrO_3$ has to be considered. Patnaik and Virkar pointed out that addition of alkali ions increases the basicity of the perovskite, affecting proton conductivity.[7] Thangadurai *et al.* studied the effect of K dopants on proton conductivity in the double perovskite $Ba_{3-x}K_xCaNb_2O_{9-\delta}$ (BKCN) and found that K dopants improve proton conductivity relative to $BaCaNb_2O_{9-\delta}$ (BCN).[8]

We examine proton conductivity's dependence on alkali dopants and the combination of alkali dopants with Y as a representative B-site dopant in $BaZrO_3$. DFT calculations are used to find the energy barriers for proton hopping and are followed by Kinetic Monte Carlo (KMC) simulations to determine the overall proton diffusivity.

In our DFT calculations, one Ba^{2+} ion in a simulation volume of $2\times2\times2$ unit cells is doped by a monovalent dopant, M_1^+, and one Zr^{4+} ion is replaced by a trivalent dopant, M_2^{3+}. Each of the M_1 and M_2 dopant concentrations in our system is therefore 1/8 (12.5%). Once a proton is introduced, the doped simulation volume becomes charge neutral.[23] In this volume, we outline three (seven) representative environments that specify different energy barriers for proton transfer (proton rotation) for M_1-doped $BaZrO_3$. For (M_1,M_2)-doped $BaZrO_3$, we report 21 (21) environments that represent different energy barriers for proton transfer (proton rotation). These hops and the energy barriers for M_1-doped and (M_1,M_2)-doped $BaZrO_3$ are included in Table 5.4 and Table 5.5, respectively. It is assumed that the environment related to each proton hopping is described using the nearest neighbors of the initial and final sites of the proton.

Using DFT, we ascertain the energy barriers for the 10 proton hops for each of the 3 alkali doped $BaZrO_3$, and establish the energy barriers for the 42 proton hops for

each of the 3 combinations of alkali dopants with Y-doped $BaZrO_3$ we consider. There are two real vibrational frequencies and one imaginary vibrational frequency at the transition state, when only the proton is not fixed.

Table 5.4: Energy barriers of the proton diffusion in the case where a dopant is a nearest neighbor of the initial or final proton, where M_1 = K, Rb, or Cs.

	Nearest Neighbor of Initial Proton	Nearest Neighbor of Final Proton	E_a (eV)		
			K	Rb	Cs
Transfer 1	Ba, Ba	Ba, Ba	0.29	0.29	0.29
Transfer 2	Ba, M_1	Ba, M_1	0.36	0.34	0.38
Transfer 3	M_1, M_1	M_1, M_1	0.46	0.45	0.55
Rotation 1	Ba, Ba	Ba, M_1	0.19	0.21	0.23
Rotation 2	Ba, M_1	Ba, Ba	0.33	0.25	0.22
Rotation 3	Ba, M_1	Ba, M_1	0.31	0.32	0.35
Rotation 4	Ba, M_1	M_1, M_1	0.07	0.10	0.09
Rotation 5	M_1, M_1	Ba, M_1	0.24	0.20	0.13
Rotation 6	M_1, M_1	M_1, M_1	0.29	0.21	0.18
Rotation 7	Ba, Ba	Ba, Ba	0.15	0.15	0.15

Table 5.5: Energy barriers of the proton diffusion in the case where a dopant is a nearest neighbor of the initial or final proton, where M_1 = K, Rb, or Cs, and M_2 = Y.

	Nearest Neighbor (A) of Initial Proton	Nearest Neighbor (A) of Final Proton	Nearest Neighbor (B) of Initial Proton	Nearest Neighbor (B) of Final Proton	E_a (eV)		
					(K,Y)	(Rb,Y)	(Cs,Y)
Transfer 1	Ba, Ba	Ba, Ba	M_2, M_2	M_2, M_2	0.98	0.98	0.98
Transfer 2	Ba, Ba	Ba, Ba	M_2, M_2	M_2, Zr	0.59	0.59	0.59
Transfer 3	Ba, Ba	Ba, Ba	Zr, M_2	M_2, M_2	0.55	0.55	0.55
Transfer 4	Ba, Ba	Ba, Ba	M_2, Zr	M_2, Zr	0.35	0.35	0.35
Transfer 5	Ba, Ba	Ba, Ba	M_2, Zr	Zr, Zr	0.40	0.40	0.40
Transfer 6	Ba, Ba	Ba, Ba	Zr, Zr	Zr, M_2	0.39	0.39	0.39
Transfer 7	Ba, Ba	Ba, Ba	Zr, Zr	Zr, Zr	0.29	0.29	0.29
Transfer 8	Ba, M_1	Ba, M_1	M_2, M_2	M_2, M_2	1.03	0.93	0.80
Transfer 9	Ba, M_1	Ba, M_1	M_2, M_2	M_2, Zr	0.68	0.64	0.62
Transfer 10	Ba, M_1	Ba, M_1	Zr, M_2	M_2, M_2	0.56	0.49	0.51
Transfer 11	Ba, M_1	Ba, M_1	M_2, Zr	M_2, Zr	0.39	0.38	0.38
Transfer 12	Ba, M_1	Ba, M_1	M_2, Zr	Zr, Zr	0.37	0.39	0.37
Transfer 13	Ba, M_1	Ba, M_1	Zr, Zr	Zr, M_2	0.36	0.33	0.34
Transfer 14	Ba, M_1	Ba, M_1	Zr, Zr	Zr, Zr	0.36	0.34	0.38
Transfer 15	M_1, M_1	M_1, M_1	M_2, M_2	M_2, M_2	1.38	1.16	0.91
Transfer 16	M_1, M_1	M_1, M_1	M_2, M_2	M_2, Zr	0.98	0.81	0.70
Transfer 17	M_1, M_1	M_1, M_1	Zr, M_2	M_2, M_2	0.81	0.67	0.60
Transfer 18	M_1, M_1	M_1, M_1	M_2, Zr	M_2, Zr	0.63	0.55	0.60
Transfer 19	M_1, M_1	M_1, M_1	M_2, Zr	Zr, Zr	0.62	0.53	0.45
Transfer 20	M_1, M_1	M_1, M_1	Zr, Zr	Zr, M_2	0.53	0.44	0.40
Transfer 21	M_1, M_1	M_1, M_1	Zr, Zr	Zr, Zr	0.46	0.45	0.55
Rotation 1	Ba, Ba	Ba, M_1	M_2, M_2	M_2, M_2	1.05	0.99	0.93
Rotation 2	Ba, Ba	Ba, M_1	Zr, M_2	Zr, M_2	0.58	0.56	0.54
Rotation 3	Ba, Ba	Ba, M_1	Zr, Zr	Zr, Zr	0.19	0.21	0.23
Rotation 4	Ba, M_1	Ba, Ba	M_2, M_2	M_2, M_2	1.04	0.90	0.76
Rotation 5	Ba, M_1	Ba, Ba	Zr, M_2	Zr, M_2	0.62	0.52	0.42
Rotation 6	Ba, M_1	Ba, Ba	Zr, Zr	Zr, Zr	0.33	0.25	0.22
Rotation 7	Ba, M_1	Ba, M_1	M_2, M_2	M_2, M_2	1.09	1.00	0.93
Rotation 8	Ba, M_1	Ba, M_1	Zr, M_2	Zr, M_2	0.64	0.58	0.55
Rotation 9	Ba, M_1	Ba, M_1	Zr, Zr	Zr, Zr	0.31	0.32	0.35
Rotation 10	Ba, M_1	M_1, M_1	M_2, M_2	M_2, M_2	0.85	0.73	0.56
Rotation 11	Ba, M_1	M_1, M_1	Zr, M_2	Zr, M_2	0.39	0.33	0.25
Rotation 12	Ba, M_1	M_1, M_1	Zr, Zr	Zr, Zr	0.07	0.10	0.09
Rotation 13	M_1, M_1	Ba, M_1	M_2, M_2	M_2, M_2	1.14	0.87	0.53
Rotation 14	M_1, M_1	Ba, M_1	Zr, M_2	Zr, M_2	0.62	0.45	0.25
Rotation 15	M_1, M_1	Ba, M_1	Zr, Zr	Zr, Zr	0.24	0.20	0.13
Rotation 16	M_1, M_1	M_1, M_1	M_2, M_2	M_2, M_2	1.24	0.87	0.48
Rotation 17	M_1, M_1	M_1, M_1	Zr, M_2	Zr, M_2	0.64	0.41	0.25
Rotation 18	M_1, M_1	M_1, M_1	Zr, Zr	Zr, Zr	0.29	0.21	0.18
Rotation 19	Ba, Ba	Ba, Ba	M_2, M_2	M_2, M_2	0.84	0.84	0.84
Rotation 20	Ba, Ba	Ba, Ba	Zr, M_2	Zr, M_2	0.11	0.11	0.11
Rotation 21	Ba, Ba	Ba, Ba	Zr, Zr	Zr, Zr	0.15	0.15	0.15

Using Harmonic Transition State Theory, we determine the hopping rate for each event of proton's movement with proton vibrational frequencies.[24] After the proton hopping rates are defined, diffusivity of proton in M_1-doped and (M_1, M_2)-doped $BaZrO_3$ are obtained with KMC. In the KMC simulations, we specify a simulation volume as containing randomly arranged atoms at the desired composition of monovalent dopants at the A-site in the M_1-doped case, and monovalent and trivalent dopants at the corresponding A and B-sites in (M_1, M_2)-doped case. The size of our simulation volume is 5×5×5 unit cells. A simple algorithm describing the hopping dynamics of protons correctly reproduces the local hopping rates.[24] At each time step a proton and its move direction are randomly selected. Acceptance of a proton hop is determined by a probability given by the ratio of the attempted proton hopping rate to the maximum proton hopping rate. Time increments by $(4\ k_{fast}N_{H+})^{-1}$, where N_{H+} is the number of protons in the simulation volume and k_{fast} is the fastest hopping rate. An Einstein expression relating diffusivity to mean square displacement governs the overall proton self diffusivity.[25-27] Mean square displacement increases linearly with time and the slope describes the diffusion coefficient. Table 5.6 lists effective activation energies and pre-exponential factors for proton diffusivity in the doped materials considered.

Table 5.6: Pre-exponential factor, effective activation energy, and ionic radius for each dopant. The materials are listed in order of decreasing ionic radius.

Dopant	A ($cm^2\,s^{-1}$)	E_d (eV)	Effective Ionic Radius[28] (pm)
Cs	1.93×10^{-5}	0.284	167
Rb	2.48×10^{-5}	0.310	152
K	5.23×10^{-5}	0.429	138

The activation energy decreases with increasing cation radius, whereby Cs^+ provides the lowest energy barrier, followed by Rb^+ and K^+. In our previous studies of B-site doped $BaZrO_3$ in Chapter 4, we also find a correlation between ionic radius and effective diffusion energy barriers where the larger dopant ions have smaller effective energy barriers. This observation is consistent with the larger dopant forming weaker bonds with protons in the material.

Table 5.7: Pre-exponential factor and effective activation energy for each dopant. The materials are listed in order of increasing effective activation energy. Δ (E_d (M_1,Y) - E_d (M_1)) is the difference of effective activation energy between (M_1,Y)-doped $BaZrO_3$ and M_1-doped $BaZrO_3$ for M_1 = K, Rb, or Cs.

Dopant	A ($cm^2\,s^{-1}$)	E_d (eV) (M_1, Y)	Δ (E_d (M_1,Y) - E_d (M_1)) (eV)
(Cs,Y)	8.62×10^{-5}	0.346	0.062
(Rb,Y)	4.79×10^{-5}	0.384	0.074
(K,Y)	6.36×10^{-5}	0.478	0.049

When we introduce Y into K, Rb, or Cs-doped $BaZrO_3$, the effective activation energy barrier increases, as seen in Table 5.7. This indicates that (K,Y)-doped $BaZrO_3$ gives high barrier for proton diffusion compared to (Rb,Y)-doped and (Cs,Y)-doped $BaZrO_3$. However the increase of energy barrier for proton diffusion after the introduction of Y in K-doped $BaZrO_3$ is relatively smaller than in other two's.

The activation energy for proton diffusion and the proton concentration have to

be considered to model proton conductivity. We use the same methods for this purpose as were defined in Chapter 4, setting Y-doped $BaZrO_3$ as the reference material.

Table 5.8: Relative formation energy and Pauling electronegativity for each dopant. The materials are listed in order of decreasing electronegativity.

Dopant	ΔE_f (eV)	Pauling Electronegativity[29]
K	-0.526	0.82
Rb	-0.646	0.82
Cs	-0.716	0.79

Every A-site cation we study shows a negative value of ΔE_f, leading to a lower concentration of protons than the standard material, Y. Among the A-site cations we examine, K shows the highest value of ΔE_f. This can be understood by the relative electronegativity of the A and B-site cations in ABO_3–type perovskites in Figure 5.3. As the difference in electronegativity between A- and B-site cations decreases, the proton concentration increases due to increasingly negative hydration enthalpy values.[30] The Pauling electronegativity[31] of Ba (the A-site cation), Zr (the B-site cation), Y (standard material; B-site dopant), K (A-site dopant), Rb (A-site dopant), and Cs (A-site dopant) is shown on a "Ruler" of Pauling electronegativity in Figure 5.3. The "Δ" in Figure 5.3 indicates the difference in electronegativity between A- and B-site cations.
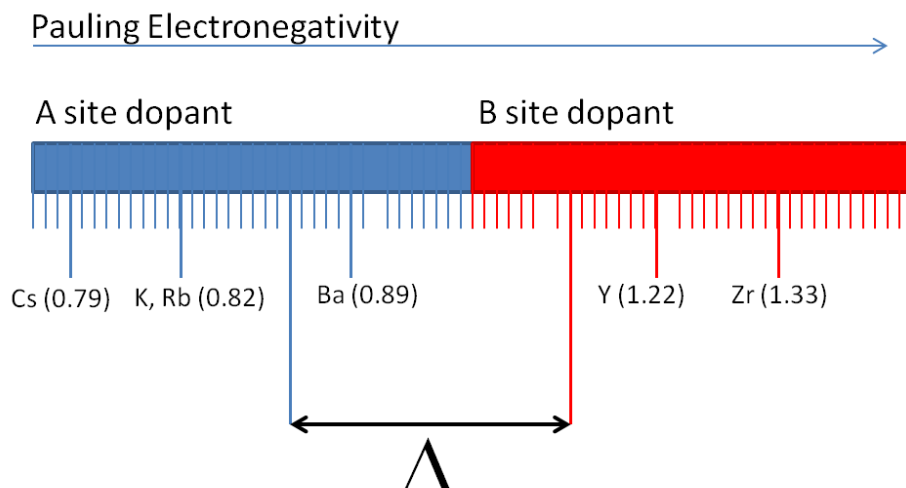
Figure 5.3: "Ruler" of Pauling electronegativity.

Table 5.9: Relative formation energy for each dopant. The materials are listed in order of decreasing relative formation energy. The differences of relative formation energy between (M_1,Y)-doped $BaZrO_3$ and M_1-doped $BaZrO_3$ for M_1 = K, Rb, or Cs.

Dopant	ΔE_f (eV) (M_1,Y)	Δ (ΔE_f (M_1,Y)- ΔE_f (M_1)) (eV)
(K,Y)	0.271	0.797
(Rb,Y)	0.133	0.779
(Cs,Y)	-0.286	0.430

As shown in Table 5.9, the differences of relative formation energy between M_1-doped $BaZrO_3$ and (M_1,Y)-doped $BaZrO_3$ are similar to each other in (K,Y)-doped case and (Rb,Y)-doped case as 0.80 and 0.78 eV, respectively. The increase of proton concentration observed for Y in K-doped $BaZrO_3$ and Y in Rb-doped $BaZrO_3$ was larger than the corresponding value for Y in Cs-doped $BaZrO_3$.

Table 5.10: The difference of electronegativity between A- and B-site in ABO_3 perovskite.

A	B	Difference of Electronegativity between A and B: $|X(A) - X(B)|$
Ba	Zr	0.44
Ba	Y	0.33
K	Zr	0.51
Rb	Zr	0.51
Cs	Zr	0.54

The (Ba,Y) pair shows the smallest difference in electronegativity, as seen in Table 5.10. The (K,Zr) and (Rb,Zr) pairs showed smaller differences than the (Cs,Zr) pair. From Table 5.10, we can see A-site dopants reduce the concentration of protons more dramatically than B-site dopants.

As discussed in our previous studies, in comparing a variety of materials, it is convenient to focus on the ratio of proton conductivities rather than the absolute quantity. The ratio of the proton conductivities for two materials is

$$\frac{\sigma_1}{\sigma_2} = \frac{C_1}{C_2}\frac{D_1}{D_2} = \frac{N_1}{N_2}\frac{A_1}{A_2}\exp\left[-\frac{(\Delta E_f + \Delta E_d)}{kT}\right], \tag{5.3}$$

where N is the number of possible proton binding sites, A is a pre-exponential factor, E_f is the formation energy of a proton, E_d is the effective activation energy, and k is the Boltzmann constant. Equation (5.3) describes the relative proton conductivities, and the subscript 1 denotes to the Y-doped material. The Y-doped material has a higher proton conductivity than material 2 if σ_1/σ_2 is larger than 1. Our results for all doped materials we consider are shown in Table 5.11.

Table 5.11: Summary of the proton conductivity of M_1-doped and (M_1,Y)-doped materials relative to Y-doped $BaZrO_3$ (σ_1/σ_2) at T = 600 K.

M_1	σ_1/σ_2	(M_1,Y)	σ_1/σ_2
K	4.26×10^5	(K,Y)	1.18×10^{-3}
Rb	4.34×10^5	(Rb,Y)	3.71×10^{-3}
Cs	1.01×10^6	(Cs,Y)	3.26

Our results in Table 5.2 rank the chemical stabilities of the doped materials as K > Rb > Cs > (K,Y) > (Rb,Y) > (Cs,Y) while the rank for proton conductivity at 600 K is (K,Y) > (Rb,Y) > (Cs,Y) > K > Rb > Cs, respectively. Although (K,Y)-doped $BaZrO_3$ shows a higher effective energy barrier for proton diffusion than the other two perovskites, it still shows higher proton conductivity than the other two because of contributions from the formation energy. Similar effects of formation energy are observed in our previous studies on B-site doped $BaZrO_3$ in Chapter 4.

Table 5.12: The summation of the relative diffusion energy barrier and relative formation energy for each dopant. The materials are listed in order of decreasing $\Delta E_f + \Delta E_d$ (eV). The differences of $\Delta E_f + \Delta E_d$ (eV) between (M_1,Y)-doped $BaZrO_3$ and M_1-doped $BaZrO_3$ for M_1 = K, Rb, or Cs.

Dopant	$\Delta E_f + \Delta E_d$ (eV)	Dopant	$\Delta E_f + \Delta E_d$ (eV)	$\Delta ((\Delta E_f + \Delta E_d) (M_1,Y) - (\Delta E_f + \Delta E_d) (M_1))$ (eV)
K	-0.097	(K,Y)	0.749	0.846
Rb	-0.336	(Rb,Y)	0.517	0.853
Cs	-0.432	(Cs,Y)	0.060	0.492

Because the ratio of the diffusion prefactors fluctuates only slightly, we characterize the overall conductivity with the diffusion energy barrier and relative formation energy. As shown in Table 5.12, the differences of summation of the diffusion energy barrier and relative formation energy between M_1-doped $BaZrO_3$ and (M_1,Y)-

doped $BaZrO_3$ are similar to each other for K and Rb within 0.007 eV. The increase of the proton conductivity observed for Y in K-doped $BaZrO_3$ and Y in Rb-doped $BaZrO_3$ was larger than the corresponding value for Y in Cs-doped $BaZrO_3$.

In our previous studies on B-site doped $BaZrO_3$ in Chapter 4, we conclude that higher dopant electronegativity leads to high chemical stability as we also find in the literature.[4, 32] This trend can also be seen in our results for dopants with K, Rb, and Cs. K which has higher electronegativity than Rb and Cs showed higher chemical stability than Rb and Cs with respect to carbonate formation reaction as shown.
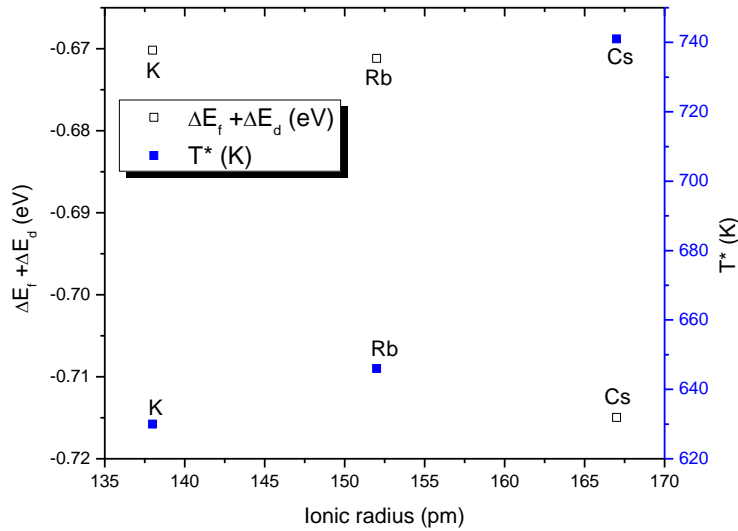
Figure 5.4: Critical temperature T* (K) and $\Delta E_f + \Delta E_d$ (eV) as a function of the ionic radius (pm) of dopants in M_1-doped $BaZrO_3$ for M_1 = K, Rb, or Cs.

The critical temperature for carbonate formation and the net energy associated with proton conductivity, $\Delta E_f + \Delta E_d$, is shown as a function of the dopant ionic radius in Figure 5.4. As the ionic radius increases, the proton conductivity decreases and the chemical stability is also reduced.
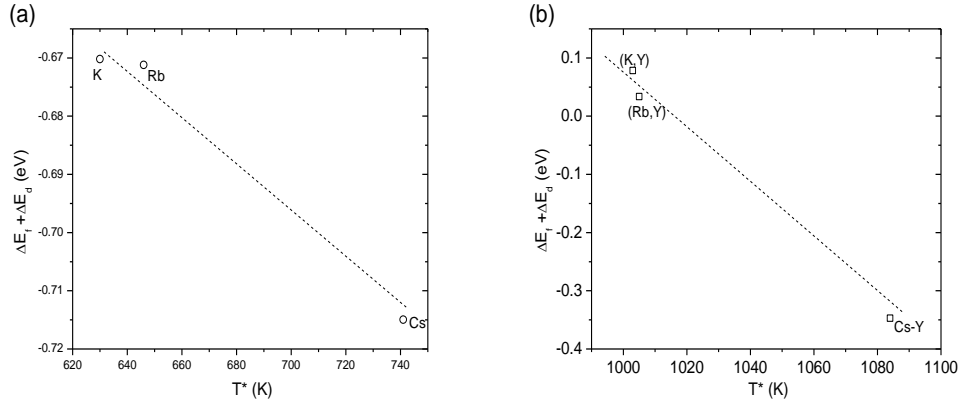
Figure 5.5: $\Delta E_f + \Delta E_d$ (eV) as a function of critical temperature T* (K) of dopants in (a) M_1-doped $BaZrO_3$ and (b) (M_1,Y)-doped $BaZrO_3$, for M_1 = K, Rb, or Cs. The dashed line shows the trend of $\Delta E_f + \Delta E_d$ (eV) as a function of T*.

Previously, for almost all of the dopants in B-site cations, a simple tradeoff is evident in which improvements in chemical stability (lower T*) correspond to lower proton conductivity, as characterized by $\Delta E_f + \Delta E_d$. However, for A-site cations, the opposite result is seen. The materials that show higher chemical stability also have higher proton conductivity. This is shown in Figure 5.5 (a). K-doped $BaZrO_3$ shows the highest chemical stability (the lowest critical temperature) and highest proton conductivity among the other alkali monovalent ion doped $BaZrO_3$ we examined.

In the case of (M_1,Y)-doped $BaZrO_3$, (K,Y)-doped materials show both higher chemical stability and proton conductivity than (Rb,Y)-doped and (Cs,Y)-doped materials as shown in Figure 5.5 (b). Liu *et al.* found that (K,Y)-doped $BaZrCeO_3$ shows the higher total ionic conductivity than Y-doped $BaZrCeO_3$.[33] We also find that (K,Y)-doped $BaZrO_3$ has higher proton conductivity than Y-doped $BaZrO_3$, as shown in Table 5.12.

Among the A-site dopants, K shows the highest proton conductivity and

chemical stability with respect to carbonate formation reaction. With this motivation, we examine the relative proton formation energy in (K,M_2)-doped $BaZrO_3$, for $M_2 \neq Y$, since proton formation energies have a more dominant role than proton diffusion in proton conductivity. The same methods defined in Chapter 4 are employed to predict the relative formation energy of a wide range of pairs of (K,M_2), using Y-doped $BaZrO_3$ as the reference material. This relative formation energy of (K,M_2) is shown in Table 5.13.

Table 5.13: Summary of the relative formation energy of (K,M_2)-doped materials, and the differences of the relative formation energy between (K,M_2)-doped $BaZrO_3$ and M_2-doped $BaZrO_3$ for M_2 = In, Ga, Sc, Nd, Al, Tl, Sm, Dy, La, Pm, Er, or Ho. The materials are listed in order of increasing ΔE_f (eV)**.**

M	ΔE_f (eV)	$\Delta\Delta E_f$ (eV)
(K,Tl)	-0.231	-0.318
(K,Sc)	-0.135	0.27
(K,In)	-0.102	0.213
(K,Al)	0.002	-0.207
(K,La)	0.045	-0.442
(K,Ga)	0.098	0.318
(K,Er)	0.173	0.249
(K,Ho)	0.223	0.256
(K,Dy)	0.274	0.266
(K,Sm)	0.417	0.211
(K,Nd)	0.422	0.102
(K,Pm)	0.423	0.168

$\Delta\Delta E_f$ is the difference of ΔE_f between (K,M_2)-doped $BaZrO_3$ and M_2-doped $BaZrO_3$. A positive value of $\Delta\Delta E_f$ implies an increase of proton concentration due to the addition of K to M_2-doped $BaZrO_3$. Our results show that addition of K to M_2-doped $BaZrO_3$ increases the proton concentration for all M_2 species we considered apart from Al, La, and Tl. Surprisingly, ΔE_f of (K,La)-doped $BaZrO_3$ is smaller than ΔE_f of La-doped $BaZrO_3$. K affects Ga- (La)-doped $BaZrO_3$ the most to increase (decrease) the

proton concentration.

Based on the "Ruler" of Pauling electronegativity, there is a smaller difference in electronegativity between K and Sm, Nd, Pm, and La than between K and Y. Hence, higher proton concentrations in the dopant pairs (K,Sm), (K,Nd), (K,Pm), and (K,La) than in (K,Y) lead to a correspondingly higher ΔE_f. Remarkably, except for (K,La), the dopant pairs (K,Sm), (K,Nd), and (K,Pm) are predicted to have the highest proton formation energies (even higher than the ΔE_f of (K,Y)) in our calculations. These pairs will be the most promising to study experimentally.

However, it is still important to consider chemical stability of these dopants. Previously, when we introduce Y in M_1-doped $BaZrO_3$ in Table 5.2, we find that the rank of the chemical stability is the same in M_1-doped $BaZrO_3$, although the critical temperature increases due to the presence of Y. Likewise, the stability of (K,M_2)-doped $BaZrO_3$ follows the same trend of rank as M_2-doped $BaZrO_3$. In Chapter 4, we find that the chemical stability of Sm, Pm, and Nd-doped $BaZrO_3$ were poor with the poorest being La-doped $BaZrO_3$ in the study of M_2-doped $BaZrO_3$. Therefore, (K,Sm), (K,Nd), and (K,Pm) doping will provide less chemical stability than (K,Y) doping to $BaZrO_3$.

5.5   Conclusion

In this chapter, DFT-based modeling is employed to analyze potentially promising A-site monovalent dopants and pairs of A, B-site dopants in terms of their chemical stability and proton conductivity in $BaZrO_3$. In this study, we choose Y as a representative trivalent dopant in B-sites. We examine physical relationships between chemical stability and proton conductivity in M_1-doped and (M_1,M_2)-doped $BaZrO_3$. One

of the main conclusions from our calculations is that there is a simple linear relationship between chemical stability and proton conductivity in A-site doped $BaZrO_3$. Among the other A-site dopants we investigated, K-doped $BaZrO_3$ shows the highest proton conductivity and highest chemical stability with respect to carbonate formation reaction. (K,Y)-doped $BaZrO_3$ also shows the highest proton conductivity and highest chemical stability among the other (M_1,Y)-doped $BaZrO_3$, although chemical stability is lower and proton conductivity is higher due to the addition of Y dopant in K-doped $BaZrO_3$.

We focus on the formation energy of a wide range of pairs of K and other B-site dopants (M_2, where M_2 = In, Ga, Sc, Nd, Al, Tl, Sm, Dy, La, Pm, Er, or Ho), and find that (K,Sm), (K,Nd), and (K,Pm)-doped $BaZrO_3$ show the highest ΔE_f, increasing the proton conductivity. We also find that the addition of K affects Ga- (La)-doped $BaZrO_3$ the most to enhance (reduce) proton concentration.

In short, (M_1,Y)-doped $BaZrO_3$ shows lower chemical stability than both M_1-doped $BaZrO_3$ and Y-doped $BaZrO_3$. This indicates that (M_1,M_2) doping reduces chemical stability of $BaZrO_3$. In other words, co-doping is not desirable in terms of chemical stability of perovskites. However, some dopant pairs, such as (K,Nd), (K,Sm), and (K,Pm) are predicted to improve proton conductivity. Therefore, it is necessary to select the dopants (or dopant pairs) depending on applications.

5.6 References

1. Iwahara, H., Esaka, T., Uchida, H., Maeda, N., *Solid State Ionics* **1981**, 3-4, 359.
2. Iwahara, H., *Solid State Ionics* **1992**, 575-586.
3. Norby, T., Proton conductivity in perovskite oxides, in Perovskite oxide for solid oxide fuel cells, Springer, 2009, 217.
4. Kreuer, K. D., *Annu. Rev. Mater. Res.* **2003**, 33, 333.
5. Nicholson, K. M., Sholl, D. S., *Phys. Rev. B* **2012**, 86, 134113.
6. Mukundan, R., Brosha, E. L., Birdsell, S. A., Costello, A. L., Garzon, F. H., Willms, R. S., *J. Electrochem. Soc.* **1999**, 146, 2184.
7. Patnaik, A. S., Virkar, A. V., *J. Electrochem. Soc.* **2006**, 153, A1397-A1405.
8. Bhella, S. S., Thangadurai, V., *Solid State Ionics* **2011**, 192, 229-234.
9. Kresse, G., Hafner, J., *Phys. Rev. B* **1993**, 47, 558.
10. Kresse, G., Furthmüller, J., *Phys. Rev. B* **1996**, 54, 11169.
11. Perdew, J. P., Chevary, J. A., Vosko, S. H., Jackson, K. A., Pederson, M. R., Singh, D. J., Fiolhais, C., *Phys. Rev. B* **1992**, 46, 6671-6687.
12. Vanderbilt, D., *Phys. Rev. B* **1990**, 41, 7892-7895.
13. Monkhorst, H. J., Pack, J. D., *Phys. Rev. B* **1976**, 13, 5188-5192.
14. The Inorganic Crystal Structure Database (ICSD). The Inorganic Crystal Structure Database (ICSD) http://www.fiz-informationsdienste.de/en/DB/icsd/.
15. Parlinski, K. Software PHONON, 2005.
16. Ackland, G. J., *J. Phys.: Condens. Matter* **2002**, 14, 2975.
17. Mortimer, R. G., Physical Chemistry. 2nd ed., (Academic Press, New York, 2000).
18. Chase, M. J. W., *J. Phys. Chem. Ref. Data Monogr.* **1998**, 9, 1.
19. Kreuer, K. D., Munch, W., Ise, M., He, T., Fuchs, A., Traub, U., Maier, J., *Ber. Bunsen. Phys. Chem.* **1997**, 101, 1344.
20. Kim, K. C., Sholl, D. S., *J. Phys. Chem. C* **2010**, 114, 678.
21. Chamberlain, J. W., Hunten, D. M., Theory of Planetary Atmospheres: An Introduction to Their Physics and Chemistry (Academic Press, San Diego, 1987).
22. Zhong, Z. M., *Solid State Ionics* **2007**, 178, 213-220.
23. Gomez, M. A., Chunduru, M., Chigweshe, L., Foster, L., Fensin, S. J., Fletcher, K. M., Fernandez, L. E., *J. Chem. Phys.* **2010**, 132, 21.
24. Sholl, D. S., Steckel, J. A., Density Functional Theory: A Practical Introduction (Wiley, Hoboken, NJ, 2009).
25. Kamakoti, P., Sholl, D. S., *Phys. Rev. B* **2005**, 71, 014301.
26. Kang, S. G., Coulter, K. E., Gade, S. K., Way, J. D., Sholl, D. S., *J. Phys. Chem. Lett.* **2011**, 2, 3040.
27. Semidey-Flecha, L., Sholl, D. S., *J. Chem. Phys.* **2008**, 128, 144701.
28. Shannon, R. D., *Acta Crystallogr., Sect. A* **1976**, 32, 751.
29. Pauling, L., The Nature of the Chemical Bond. Third Edition ed. (Cornell University Press, Ithaca, NY, 1960).
30. Laidoudi, M., Talib, I. A., Omar, R., *J. Phys. D: Appl. Phys.* **2002**, 35, 397.
31. http://www.webelements.com.
32. Xie, K., Yan, R. Q., Chen, X. R., Dong, D. H., Wang, S. L., Liu, X. Q., Meng, G. Y., *J. Alloys Compd.* **2009**, 472, 551.

33. Zuo, C., Wang, J. H., Liu, M., Development of Novel Electrolyte Materials for a New Generation of Low-Temperature SOFCs. Final report. Nissan Research Center, Technology Research Laboratory No. 1; 2007 Feb. Project No. 103758.

CHAPTER 6

B-SITE DOPED BARIUM STANNATE AND BARIUM HAFNATE

6.1   Introduction

Proton-conducting perovskites are attractive as electrolytes and hydrogen sensors.[1-3] Protons are generated in the perovskites due to water vapor or dry hydrogen molecules in ambient gas being in equilibrium with defects in the oxide lattice.[3, 4]

Many questions about defect formation and mobility have been answered using DFT calculation. Furthermore, these DFT studies are useful for experiments with perovskites.[5-15] It is shown that Ga-doping has the highest chemical stability and La-doping has the highest proton conductivity in $BaZrO_3$ in Chapter 4. In this study, we examine the chemical stability and proton conductivity of Ga or La-doped barium stannate ($BaSnO_3$) and barium hafnate ($BaHfO_3$).

Barium stannate ($BaSnO_3$) has a cubic structure and it is stable up to 1273 K.[16] $BaSnO_3$ has been used as a proton conductor.[17-19] Proton conductivity in Y-doped $BaSnO_3$ and In-doped $BaSnO_3$ has been studied.[18, 19] In-doped $BaSnO_3$ shows high solubility of water for high temperature proton conductors, although it is unstable in hydrogen-rich atmospheres.[19] The proton migration energy barrier in In-doped $BaSnO_3$ was found to be 0.56 ± 0.03 eV.[19]   Bévillon *et al*. examined hydration properties of La-doped $BaSnO_3$ using DFT calculations and found that La dopants attract protons and oxygen vacancies.[20, 21] Proton conductivity in Y-doped barium hafnate ($BaHfO_3$) has also been examined.[22] It has slightly higher proton conductivity than Y-doped barium zirconates ($BaZrO_3$) at high temperatures.[22]

After describing our computational methods in section 6.2, we begin section 6.3 by examining the stability of doped $BaSnO_3$ and $BaHfO_3$ with respect to the carbonate formation reaction. We used DFT calculations of reaction free energies at finite temperatures, enabling us to predict the phase stability of oxide and carbonate phases as functions of temperature and CO_2 partial pressure. Then, the proton mobility through each material is investigated. Extensive DFT calculations are performed to elucidate the activation energies and hopping prefactors for local hops by protons, and this information is integrated into a lattice model for the doped material to determine net proton mobilities. This approach is also used in our study of proton diffusion in $BaZrO_3$ in Chapter 4.

6.2   Calculation methods

Plane-wave density functional (DFT) calculations are carried out with the Vienna *ab initio* Simulation Package (VASP).[23, 24] All calculations are performed using the generalized gradient approximation (GGA) to describe electron exchange-correlation effects using PW91 functional. The electron-ion interaction is described by the projector augmented wave (PAW) method.[23-26] A plane-wave expansion with a cutoff of 500 eV is used in all calculations. *k*-points are generated using the Monkhorst–Pack method[27] with the number of *k*-points chosen to give a spacing of around 0.028 Å^{-1} along the axes of the reciprocal unit cells.

Our calculations for each compound in this study are performed using experimental lattice constants from Inorganic Crystal Structure Database (ICSD).[28] The cell shape and ionic coordinates are relaxed until forces on each atom are less than 0.03

eV Å^{-1}. After the geometry optimization, the vibrational density of states (VDOS) of the crystalline compounds is computed to provide the temperature-dependent vibrational energies and thermal entropies of solid compounds for examination of the free energy of reaction at finite temperature, ΔG(T), within the harmonic approximation.[29] The PHONON code developed by Parlinski[30] is used to calculate the phonon density of states and the vibrational contribution to the free energy using the direct method. We choose a displacement magnitude of 0.03 Å. Pressure-volume (PV) term contributions for solid phases are neglected with the assumption that the difference between the chemical potential of solid phases can be modeled as the difference in their electronic energy and the vibrational free energy of phonons.[31] Gas phase CO_2 is treated like an ideal gas. The free energies of CO_2 are calculated from standard statistical mechanics as [32]

$$G_{CO2} = \frac{7}{2}RT + \sum_{i=1}^{4} \frac{N_a h v_i}{e^{hv_i/kT}-1} - TS_{CO2}(T) \ , \tag{6.1}$$

where N_a is Avogadro's constant, R is the universal gas constant, T is temperature, and v_i are the vibrational frequencies of CO_2 in G$_{CO2}$. The Shomate equation is used to calculate the temperature-dependent entropy of CO_2.[33]

$$S = A \ln(t) + Bt + \frac{Ct^2}{2} + \frac{Dt^3}{3} - \frac{E}{2t^2} + F, \tag{6.2}$$

where $t = T/1000$, and A to F are system dependent constants.

As in previous chapters, we utilize a quasi-Newton optimization method to find transition state based on initial configuration close to a true transition state. Our results for proton diffusivity of A-site doped, B-site doped, and (A,B)-site doped in $BaZrO_3$ in Chapters 4-5 are obtained using this approach, and we find that this method saves computational time and resources, since we do not need intermediate images

(coordinates), as required in the Nudged Elastic Band (NEB) method. Therefore, we do not have to use NEB calculations for any of the transition states described below.

### *6.2.1*   **DFT calculated results of geometry optimization**

The optimized lattice constants for each compound considered in this work are presented in Table 6.1 along with the corresponding experimental data. For $BaZrO_3$, Ga-doping gives the highest chemical stability, while La-doping provides the highest proton conductivity (see Chapter 4). These results, in turn, motivate the use of these dopants in two different proton-conducting perovskites, $BaSnO_3$ and $BaHfO_3$. Ga_2O_3 and La_2O_3 are the compounds from the decomposition of Ga-doped and La-doped perovskites by carbonate formation reactions. The initial structures for geometry relaxations are obtained from the experimental data available from the Inorganic Crystal Structure Database (ICSD).[28] The predicted values using the GGA functional are slightly larger than experimental lattice constants except for La_2O_3.

Table 6.1. Comparison of the experimental[28] and the DFT calculated structural parameters for the 6 crystalline compounds considered in our calculations, with all lengths in Å and angles in degrees.

Compound	Space group	Structural Parameters (Å, degree)	
		Experimental	Calculated
Ga_2O_3	*C12/m1*	$a = 12.230$ $b = 3.040$ $c = 5.800$ $\beta = 103.7$	$a = 12.464$ $b = 3.096$ $c = 5.905$ $\beta = 103.8$
La_2O_3	*P-3m1*	$a = 3.940$ $b = 3.940$ $c = 6.130$ $\gamma = 120$	$a = 3.939$ $b = 3.939$ $c = 6.149$ $\gamma = 120$
SnO_2	*P42/MNM*	$a = 4.733$ $c = 3.182$	$a = 4.820$ $c = 3.240$
HfO_2	*P12₁/c1*	$a = 5.113$ $b = 5.172$ $c = 5.295$ $\beta = 99.188$	$a = 5.123$ $b = 5.188$ $c = 5.294$ $\beta = 99.716$
$BaSnO_3$	*Pm-3m*	$a = 4.156$	$a = 4.181$
$BaHfO_3$	*Pm-3m*	$a = 4.171$	$a = 4.194$

6.3 Chemical stability

The carbonate formation reactions of doped $Ba(M_1)O_3$ in the presence of CO_2 can be written as

$$Ba(M_1)_{0.75} (M_2)_{0.25} O_{3-\delta} + CO_2 \leftrightarrow BaCO_3 + 0.75 (M_1)O_2 + 0.25 (M_2)_2O_3, \quad (6.3)$$
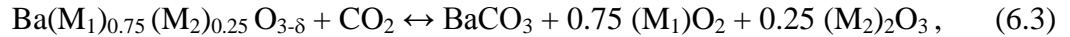
where M_1 is a B-site host species, such as Zr, Sn or Hf, and M_2 is a trivalent ion, such as Ga or La. We investigate the stability of undoped-BaM_1O_3, and extend our calculations to materials doped with M_2^{3+} at the B-site. Oxygen vacancies are generated for charge neutrality upon the introduction of dopants.[34] The dopant concentration used in our calculations is 2/8 (25%). Thus, the net stoichiometry of the doped materials is $Ba_8(M_1)_6(M_2)_2O_{23}$. The $2\times2\times2$ unit cells are used for doped $Ba(M_1)O_3$ in the computational supercell, so each supercell contain two (one) dopant atoms (O vacancy). Once the O vacancy is created in the supercell, we perform calculations with different

placements of the dopants. The arrangement with the lowest energy configuration is utilized in the VDOS calculation. For Ga, this state has two dopant atoms placed next to each other in three of the perovskites we investigate, whereas the two dopants in the lowest energy state are separated by 6.27, 7.65, and 7.53 Å for La in $BaHfO_3$, $BaZrO_3$, and $BaSnO_3$, respectively.

It is essential to include the configurational entropy of disordered $(M_2)^{3+}$ and oxygen vacancies in the calculation of free energy of the doped materials.[35] The configurational entropy is defined by the Boltzmann definition of entropy, $S = k\ln\Omega$, where Ω is the number of dopant-vacancy configurations possible.[36] All orderings of dopants and vacancies are assumed to be equally likely. This provides a configurational entropy for $BaSn_{0.75}(M_2)_{0.25}O_{3-\delta}$ and $BaHf_{0.75}(M_2)_{0.25}O_{3-\delta}$ of 54.1 J K^{-1} mol^{-1}. This value is likely to be greater than the true configurational entropy because of small energy differences between configurations. However, we do not attempt to study this effect further.

The van't Hoff relation gives the equilibrium condition for carbonate formation:

$$\frac{P_{CO2}}{P_0} = \exp\left(\frac{\Delta G}{RT}\right),$$
(6.4)

$$\Delta G(T) = \Delta E_0 - n_1 G_{CO2}(T) + \Delta F^{solids}(T),$$
(6.5)

where ΔE_0 is the difference of ground state electronic total energy determined using DFT between the reactants and products, ΔG is Gibbs free energy difference between the reactants and products, n_1 is the number of moles of CO_2 involved in the reaction, G_{CO2} is a free energy of CO_2, ΔF^{solids} is the vibrational free energy change between the solids of products and reactants, R is the gas constant, T is the temperature, and P_0 is the standard state reference pressure. Figure 6.1 and 6.2 show predicted calculations with P_0

126

= 1 bar for the equilibrium CO_2 pressure associated with carbonate formation of undoped and doped $Ba(M_1)O_3$. We let T* be the critical temperature at which carbonate formation becomes favorable. As the CO_2 pressure is increased, the critical temperature increases. Perovskites with higher T* are more prone to carbonate formation and are less chemically stable.
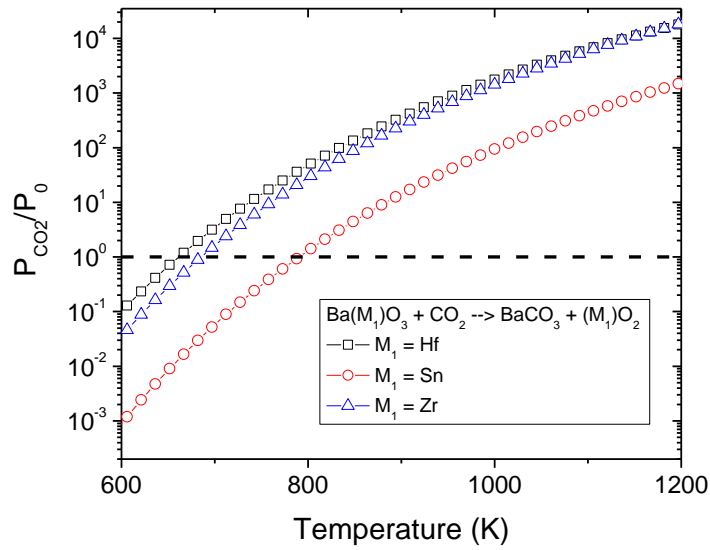

Figure 6.1: van't Hoff plot for the carbonate formation reaction of undoped $Ba(M_1)O_3$, $Ba(M_1)O_3 + CO_2 \leftrightarrow BaCO_3 + (M_1)O_2$ for M_1 = Hf, Sn, or Zr. The horizontal dashed line refers to $P_{CO2}/P_0 = 1$.
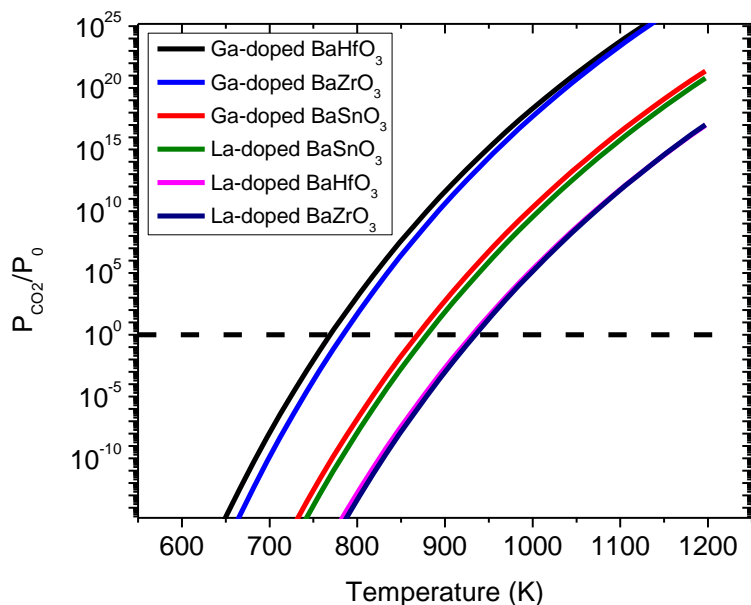
Figure 6.2: van't Hoff plot for the carbonate formation reaction of M_2-doped $Ba(M_1)O_3$, $Ba_8(M_1)_6(M_2)_2O_{23} + 8CO_2 \leftrightarrow 8BaCO_3 + 6(M_1)O_2+(M_2)O_3$ for M_1 = Hf, Sn, or Zr and M_2 = Ga or La. The horizontal dashed line refers to $P_{CO2}/P_0 = 1$.
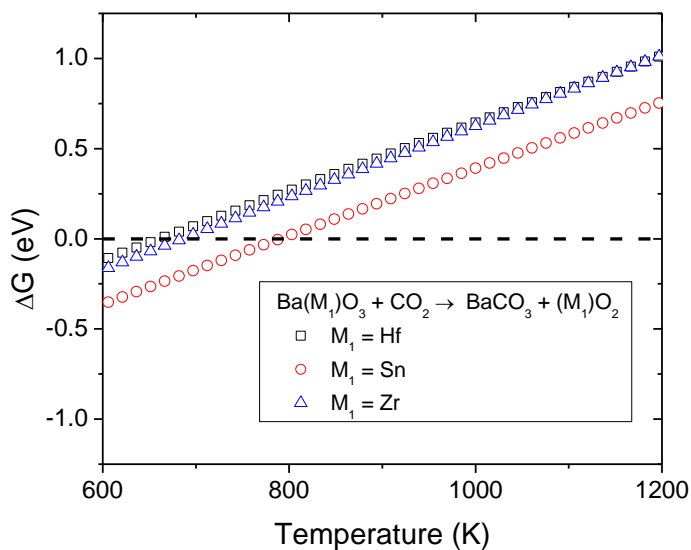

Figure 6.3: Free energy of reaction, ΔG, as a function of temperature for carbonate formation reactions. The undoped material is shown using unfilled squares for the reaction $Ba(M_1)O_3 + CO_2 \leftrightarrow BaCO_3 + (M_1)O_2$ for M_1 = Hf, Sn, or Zr.

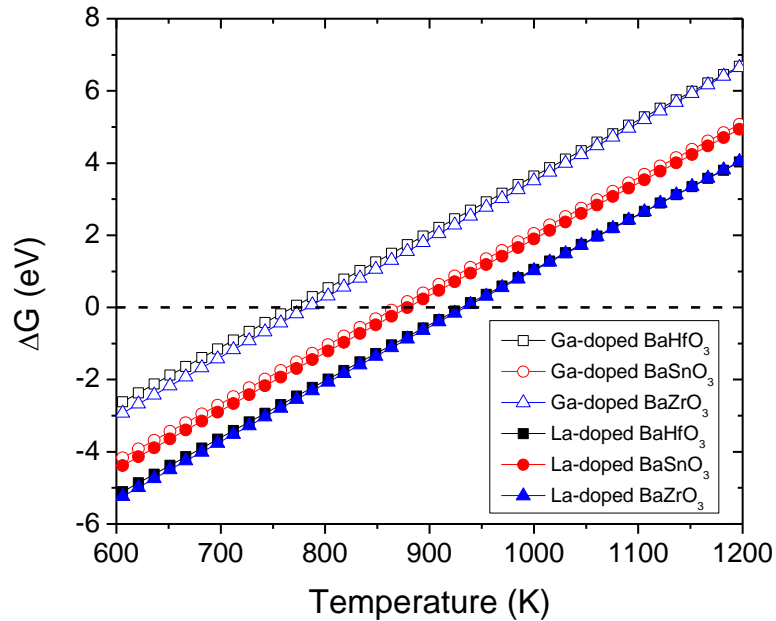**Figure 6.4:** Free energy of reaction, ΔG, as a function of temperature for carbonate formation reactions. The results for the doped materials correspond to the reaction $Ba_8(M_1)_6(M_2)_2O_{23} + 8CO_2 \leftrightarrow 8BaCO_3 + 6(M_1)O_2+(M_2)O_3$ for M_1 = Hf, Sn, or Zr and M_2 = Ga or La.

Figure 6.4 describes the stabilities of doped materials examined at a CO_2 pressure of 1 bar. The rank of chemical stabilities of undoped-$Ba(M_1)O_3$ against carbonate formation is M_1 = Hf (T* = 664 K) > Zr (T* = 688 K) > Sn (T* = 794 K), as seen in Figure 6.3. Among the materials, $BaHfO_3$ shows the highest chemical stability (i.e., the lowest critical temperature). Figure 6.4 shows that the rank of the chemical stability of M_2-doped $Ba(M_1)O_3$ with respect to CO_2 is Ga-doped $BaHfO_3$ > Ga-doped $BaZrO_3$ > Ga-doped $BaSnO_3$ > La-doped $BaSnO_3$ > La-doped $BaHfO_3$ > La-doped $BaZrO_3$. It is clear from these results that Ga-doped perovskite is more stable against carbonate formation reaction than La-doped perovskites.

Table 6.2: Predicted critical temperature of $Ba_8(M_1)_6(M_2)_2O_{23}$ for M_1 = Hf, Sn, or Zr, and M_2 = Ga or La.

Material	T* (K)	Material	T* (K)	Material	T* (K)
$BaHfO_3$	664	Ga-$BaHfO_3$	772	La-$BaHfO_3$	933
$BaSnO_3$	794	Ga-$BaSnO_3$	871	La-$BaSnO_3$	882
$BaZrO_3$	688	Ga-$BaZrO_3$	786	La-$BaZrO_3$	936

Table 6.3: The difference of critical temperature between M_2-$Ba(M_1)O_3$ and $Ba(M_1)O_3$ for M_1 = Hf, Sn, or Zr, and M_2 = Ga or La.

Dopant	Material	Δ T* (K)
Ga	$BaHfO_3$	108
Ga	$BaSnO_3$	77
Ga	$BaZrO_3$	98
La	$BaHfO_3$	269
La	$BaSnO_3$	88
La	$BaZrO_3$	248

Table 6.3 summarizes the change in critical temperature associated with the dopants we examine. $BaHfO_3$ and $BaZrO_3$ show comparable differences in critical temperature between doped and undoped cases, although the magnitude of this change is dependent on the dopant. The Ga dopant induces a smaller increase of critical temperature than the La dopant in all three materials we examine. The critical temperature of doped $BaSnO_3$ does not vary significantly with the presence of dopants. As such, the chemical stability of $BaSnO_3$ is not very sensitive to different dopants.

6.4 Proton conductivity

The impact of Ga and La dopants on proton conductivity is significant. In our previous studies of M_2-doped-$BaZrO_3$ in Chapter 4, La-doped $BaZrO_3$ shows the highest proton conductivity among the materials we investigate. From these previous studies, we find that the contribution of formation energy to proton conductivity is larger than the

contribution of proton diffusivity.

In this section, we study proton conductivity in Ga- or La-doped $BaSnO_3$ and $BaHfO_3$. In each material, DFT calculations are performed to obtain the relevant proton hopping energy barriers and then subsequently Kinetic Monte Carlo (KMC) simulations are employed to provide the overall diffusivity of protons.

According to our DFT calculations, one Sn^{4+} or Hf^{4+} ion in a simulation volume of $2\times2\times2$ unit cells is doped by a trivalent dopant $(M_2)^{3+}$. Therefore, the dopant concentration in our calculations is 1/8 (12.5%). The simulation volume with the dopants becomes charge neutral with the introduction of a proton.[7] In the volume, we designate seven (three) representative environments that possess different energy barriers for proton transfer (proton rotation). We assume that the nearest neighbors of the initial and final sites of the proton are used to define the environment of proton hopping.

The energy barriers for the 10 proton hops in Ga- or La-doped-$BaSnO_3$ and $BaHfO_3$ are obtained by DFT. These hops and energy barriers are listed in Table 6.4. Two real vibrational frequencies and one imaginary vibrational frequency are shown at the transition state, when only the proton is relaxed and the other atoms are fixed.

Table 6.4: Energy barriers of the proton in the case where a dopant is a nearest neighbor of the initial or final proton, where M_1 = Hf, Zr, or Sn, M_2 = Ga or La.

	Nearest Neighbor of Initial Proton	Nearest Neighbor of Final Proton	E_a (eV)					
			M_1 / M_2 Hf / Ga	M_1 / M_2 Hf / La	M_1 / M_2 Zr / Ga	M_1 / M_2 Zr / La	M_1 / M_2 Sn / Ga	M_1 / M_2 Sn / La
T 1	M_2, M_2	M_2, M_2	0.28	2.16	0.41	2.18	0.38	1.86
T 2	M_1, M_2	M_1, M_2	0.20	0.38	0.21	0.53	0.22	0.56
T 3	M_1, M_2	M_2, M_2	0.08	1.41	0.08	1.57	0.15	0.64
T 4	M_2, M_2	M_2, M_1	0.34	0.98	0.37	1.11	0.44	0.22
T 5	M_2, M_1	M_1, M_1	0.69	0.44	0.72	0.61	0.68	0.10
T 6	M_1, M_1	M_1, M_2	0.13	0.62	0.12	0.77	0.17	0.55
T 7	M_1, M_1	M_1, M_1	0.26	0.26	0.29	0.29	0.33	0.33
R 1	M_2, M_2	M_2, M_2	0.13	2.61	0.16	2.48	0.18	2.07
R 2	M_1, M_2	M_1, M_2	0.18	0.70	0.17	0.08	0.19	0.51
R 3	M_1, M_1	M_1, M_1	0.17	0.17	0.15	0.15	0.21	0.21

The rate of individual proton hops is computed using Harmonic Transition State Theory[33]. To define the hopping rate for proton movement events, proton vibrational frequencies are employed. Here we take the prefactor (k_0) for the hopping rate as[9]

$$k_0 = \frac{1}{2\pi} \frac{v_1 \times v_2 \times v_3}{v_1^{\dagger} \times v_2^{\dagger}} \ , \tag{6.6}$$

where v is the real vibrational frequency related to the energy minimum, and $v^{\dagger}$ is the real vibrational frequency associated with the transition state.

Upon defining hopping rates, we perform KMC to obtain the diffusivity of the proton in doped $BaHfO_3$, $BaSnO_3$, and $BaZrO_3$. In KMC simulations, we let a simulation volume of an alloy consist of randomly arranged atoms with the desired trivalent dopant composition. We use a simulation volume of 5×5×5 unit cells. An algorithm that reproduces the local hopping rates is employed to simulate the hopping dynamics of protons.[37] At each time step a proton is randomly chosen from the simulation volume and a move direction for proton hopping is randomly selected from the two (two) available directions for a transfer (rotation). Proton hopping is accepted based on a probability

defined by the ratio of the attempted hopping rate to the maximum hopping rate. Time increments are defined by $(4\ k_{fast}N_{H+})^{-1}$, where k_{fast} is the fastest proton hopping rate and N_{H+} is the number of protons in the volume we simulate. The overall proton self diffusivity is obtained using an Einstein expression that relates the diffusivity to the mean square displacement.[38-40]

The effective activation energy is obtained by fitting proton diffusivity for each dopant to

$$D = A \exp\left[-\left(\frac{E_d}{kT}\right)\right], \tag{6.7}$$

where A is a pre-exponential factor, E_d is the effective activation energy, and k is the Boltzmann constant. Table 6.5 shows calculated values for E_d and A.

Table 6.5: Effective activation energy and pre-exponential factor for each material.

Material	E_d (eV)	A $(cm^2\ s^{-1})$
$BaHfO_3$	0.233	1.48×10^{-5}
$BaSnO_3$	0.294	2.24×10^{-5}
$BaZrO_3$	0.28	2.47×10^{-5}
$Ga-BaHfO_3$	0.568	2.23×10^{-5}
$Ga-BaSnO_3$	0.58	2.13×10^{-5}
$Ga-BaZrO_3$	0.522	9.46×10^{-6}
$La-BaHfO_3$	0.244	1.33×10^{-5}
$La-BaSnO_3$	0.314	2.26×10^{-5}
$La-BaZrO_3$	0.283	1.99×10^{-5}

Using Ga, a small dopant, significantly increases the diffusion activation energy relative to the undoped materials. Using La, a large dopant, however, does not significantly impact the diffusion activation energy. This is consistent with the trend that we see in B-site doped in $BaZrO_3$ in Chapter 4, where the smaller dopants lead to higher energy barriers for proton diffusion due to the strong bonds with protons in the material.

To complement the information we report above regarding the proton diffusivity, it is also important to understand the proton concentration, which also contributes to the proton conductivity. For the comparison of materials, the methods described in Chapter 4 are used. We choose Y-doped $BaZrO_3$ as a reference state, because it is the most commonly used dopant. This allows us to clearly see the effects of different dopants (e.g., Ga and La) on proton conductivity. Additionally, this choice of reference state allows us to compare the ratio of proton conductivity of M_2-doped $Ba(M_1)O_3$ with the M_2-doped $BaZrO_3$ species discussed in Chapter 4.

Table 6.6: Summary of the proton conductivity of M_2-doped materials relative to Y-doped $BaZrO_3$ (σ_1/σ_2) at T = 600 K. All energies are shown in eV.

	ΔE_f	ΔE_d	A_1/A_2	σ_1/σ_2
La-BaHfO$_3$	0.638	0.041	1.44	2.90×10^{-6}
La-BaSnO$_3$	0.53	-0.03	0.843	5.20×10^{-5}
La-BaZrO$_3$	0.487	0.002	0.956	7.50×10^{-5}
Ga-BaZrO$_3$	-0.22	-0.237	2.015	13816
Ga-BaHfO$_3$	-0.232	-0.283	0.854	18105
Ga-BaSnO$_3$	-0.274	-0.295	0.895	53718

Our results in Tables 6.2 and 6.6 rank the chemical stabilities of the doped materials as Ga-doped $BaHfO_3$ > Ga-doped $BaZrO_3$ > Ga-doped $BaSnO_3$ > La-doped $BaSnO_3$ > La-doped $BaHfO_3$ > La-doped $BaZrO_3$ while the rank for proton conductivity at 600 K is La-doped $BaHfO_3$ > La-doped $BaSnO_3$ > La-doped $BaZrO_3$ > Ga-doped $BaZrO_3$ > Ga-doped $BaHfO_3$ > Ga-doped $BaSnO_3$, respectively. Ga-doping shows higher chemical stability while La-doping shows higher proton conductivity for all three perovskites, $BaHfO_3$, $BaZrO_3$, and $BaSnO_3$. Because the ratio of the diffusion prefactors varies only moderately, we focus on the diffusion energy barrier and relative formation energy to characterize the contributions of mobility and concentration to the overall

conductivity.

La dopants show lower electronegativity than Ga dopants, demonstrating that La-doping leads to unstable perovskites. The chemical stability of $BaSnO_3$ is not very susceptible to the dopants used, whereas the proton conductivity of $BaSnO_3$ is very sensitive to the dopants used. In other words, there is a clear difference of proton conductivity between Ga-doped $BaSnO_3$ and La-doped $BaSnO_3$. However, the difference of the critical temperature describing the chemical stability of the perovskites is smaller between Ga-doped $BaSnO_3$ and La-doped $BaSnO_3$ than between Ga-doped $BaZrO_3$ ($BaHfO_3$) and La-doped $BaZrO_3$ ($BaHfO_3$).
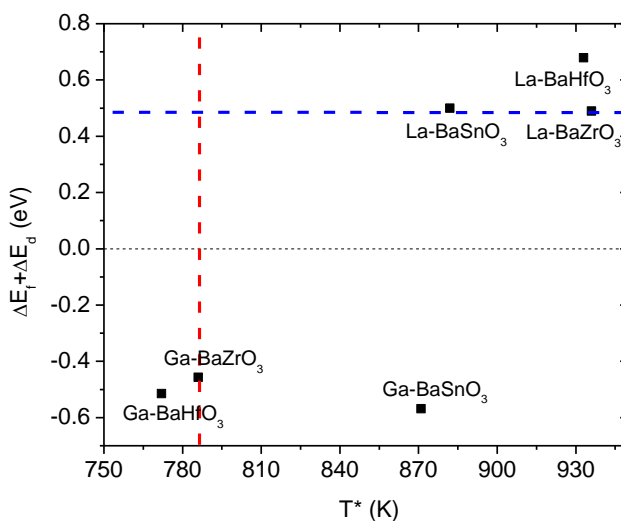
Figure 6.5: $\Delta E_f + \Delta E_d$ (eV) as a function of critical temperature T* (K) of dopants in doped M_2-doped $Ba(M_1)O_3$. The red line corresponds to the critical temperature of Ga-doped $BaZrO_3$, and the blue line refers to the $\Delta E_f + \Delta E_d$ value of La-doped $BaZrO_3$.

One of our major goals is to compare chemical stability and proton conductivity of Ga- or La-doped $BaSnO_3$ and Ga- or La-doped $BaHfO_3$ with Ga- or La-doped $BaZrO_3$. In Figure 6.5, there is a clear tradeoff between chemical stability and proton conductivity

in doped $BaHfO_3$, $BaSnO_3$, and $BaZrO_3$. However, the effects of doping on the chemical stability of $BaSnO_3$ are small. For conductivity, both La-doped $BaHfO_3$ and La-doped $BaSnO_3$ show higher proton conductivity than La-doped $BaZrO_3$. We find that doped-$BaHfO_3$ has both highest proton conductivity and chemical stability.

Ga-doped $BaHfO_3$ shows the highest chemical stability and La-doped $BaHfO_3$ shows the highest proton conductivity among the materials examined. $BaSnO_3$ is not sensitive to the dopants for chemical stability compared to the other two materials, $BaHfO_3$ and $BaZrO_3$.

6.5   Conclusion

In this chapter, we use promising dopants found in our previous studies on M_2-doped $BaZrO_3$ for chemical stability (Ga) and proton conductivity (La) using efficient DFT-based modeling in two different kinds of materials, $BaSnO_3$ and $BaHfO_3$.

Our models identify that Ga dopants induce less increase of critical temperature than La dopants in every case consider: $BaHfO_3$, $BaZrO_3$, and $BaSnO_3$. That is, Ga dopant leads higher chemical stability than La dopant. As seen in our prior studies in Chapter 4, La dopant enables perovskites to have high proton conductivity.

We conclude that there exists an inherent tradeoff between chemical stability and proton conductivity in both doped $BaSnO_3$ and $BaHfO_3$, although $BaSnO_3$ is not quite sensitive to the dopants used for its chemical stability. Improvements in one property cause a decreased performance in the other. We find that doped $BaHfO_3$ is promising to study further in a co-doped case, because it shows both higher proton conductivity and chemical stability than doped-$BaZrO_3$.

6.6   References

1.   Kreuer, K. D., *Annu. Rev. Mater. Res.* **2003**, 33, 333.
2.   Iwahara, H., *Solid State Ionics* **1992**, 575-586.
3.   Iwahara, H., *Solid State Ionics* **1996**, 86, 9-15.
4.   Kreuer, K. D., Paddison, S. J., Spohr, E., Schuster, M., *Chem. Rev.* **2004**, 104, 4637.
5.   Bork, N., Bonanos, N., Rossmeisl, J., Vegge, T., *Phys. Rev. B* **2010**, 82, 014103.
6.   Gomez, M. A., Jindal, S., Fletcher, K. M., Foster, L. S., Addo, N. D. A., Valentin, D., Ghenoiu, C., Hamilton, A., *J. Chem. Phys.* **2007**, 126, 194701.
7.   Gomez, M. A., Chunduru, M., Chigweshe, L., Foster, L., Fensin, S. J., Fletcher, K. M., Fernandez, L. E., *J. Chem. Phys.* **2010**, 132, 21.
8.   Gomez, M. A., Chunduru, M., Chigweshe, L., Fletcher, K. M., *J. Chem. Phys.* **2010**, 133, 6.
9.   Bjorketun, M. E., Sundell, P. G., Wahnstrom, G., *Phys. Rev. B* **2007**, 76, 054307.
10.   Sundell, P. G., Bjorketun, M. E., Wahnstrom, G., *Phys. Rev. B* **2007**, 76, 094301.
11.   Bjorketun, M. E., Sundell, P. G., Wahnstrom, G., *Faraday Discuss.* **2007**, 134, 247.
12.   Islam, M. S., Davies, R. A., Gales, J. D., *Chem. Mater.* **2001**, 13, 2049.
13.   Islam, M. S., Davies, R. A., Gale, J. D., *Chem. Commun.* **2001**, 7, 661.
14.   Shimojo, F., Hoshino, K., *Solid State Ionics* **2001**, 145, 421-427.
15.   Zhang, Q. F., Wahnstrom, G., Bjorketun, M. E., Gao, S. W., Wang, E. G., *Phys. Rev. Lett.* **2008**, 101, 215902.
16.   Ostrick, B., Fleischer, M., Lampe, U., Meixner, H., *Sensors Actuat. B Chem.* **1997**, 44, 601-606.
17.   Kreuer, K. D., *Solid State Ionics* **1999**, 125, 285-302.
18.   Murugaraj, P., Kreuer, K. D., He, T., Schober, T., Maier, J., *Solid State Ionics* **1997**, 98, 1-6.
19.   Schober, T., *Solid State Ionics* **1998**, 109, 1-11.
20.   Bevillon, E., Geneste, G., Chesnaud, A., Wang, Y. Z., Dezanneau, G., *Ionics* **2008**, 14, 293-301.
21.   Bevillon, E., Chesnaud, A., Wang, Y. Z., Dezanneau, G., Geneste, G., *J. Phys.: Condens. Matter* **2008**, 20, 145217.
22.   Snijkers, F. M. M., Buekenhoudt, A., Luyten, J. J., Cooymans, J., Mertens, M., *Scr. Mater.* **2004**, 51, 1129-1134.
23.   Kresse, G., Hafner, J., *Phys. Rev. B* **1993**, 47, 558.
24.   Kresse, G., Furthmüller, J., *Phys. Rev. B* **1996**, 54, 11169.
25.   Perdew, J. P., Chevary, J. A., Vosko, S. H., Jackson, K. A., Pederson, M. R., Singh, D. J., Fiolhais, C., *Phys. Rev. B* **1992**, 46, 6671-6687.
26.   Vanderbilt, D., *Phys. Rev. B* **1990**, 41, 7892-7895.
27.   Monkhorst, H. J., Pack, J. D., *Phys. Rev. B* **1976**, 13, 5188-5192.
28.   The Inorganic Crystal Structure Database (ICSD). The Inorganic Crystal Structure Database (ICSD) http://www.fiz-informationsdienste.de/en/DB/icsd/.
29.   Ackland, G. J., *J. Phys.: Condens. Matter* **2002**, 14, 2975.
30.   Parlinski, K. Software PHONON, 2005.
31.   Alapati, S. V., Johnson, J. K., Sholl, D. S., *J. Phys. Chem. C* **2008**, 112, 5258.

32. Mortimer, R. G., Physical Chemistry. 2nd ed.,
    (Academic Press, New York, 2000).
33. Chase, M. J. W., *J. Phys. Chem. Ref. Data Monogr.* **1998**, 9, 1.
34. Kreuer, K. D., Munch, W., Ise, M., He, T., Fuchs, A., Traub, U., Maier, J., *Ber. Bunsen. Phys. Chem.* **1997**, 101, 1344-1350.
35. Kim, K. C., Sholl, D. S., *J. Phys. Chem. C* **2010**, 114, 678.
36. Chamberlain, J. W., Hunten, D. M., Theory of Planetary Atmospheres: An Introduction to Their Physics and Chemistry (Academic Press, San Diego, 1987).
37. Sholl, D. S., Steckel, J. A., Density Functional Theory: A Practical Introduction (Wiley, Hoboken, NJ, 2009).
38. Kamakoti, P., Sholl, D. S., *Phys. Rev. B* **2005**, 71, 014301.
39. Kang, S. G., Coulter, K. E., Gade, S. K., Way, J. D., Sholl, D. S., *J. Phys. Chem. Lett.* **2011**, 2, 3040.
40. Semidey-Flecha, L., Sholl, D. S., *J. Chem. Phys.* **2008**, 128, 144701.

CHAPTER 7

POTASSIUM TANTALATE

7.1   Introduction

Perovskite-type oxides are considered as candidates for electrolyte materials in electrochemical applications.[1] The major features of proton migration through the Grotthuss mechanism consist of two elementary steps in perovskite materials:[2, 3] (1) transfer of protons between adjacent oxide ions and (2) rotation of proton-carrying oxide ions. In experiments, however, it is challenging to directly examine proton migration mechanisms and assess the energy barriers along the pathway of proton transfer. Gomez *et al.*[4] determined the proton binding site and energy barrier for proton diffusion mechanisms in a defect-free KTO, a prototypical cubic perovskite material[4, 5] using first-principles calculations. However, there is no comparable information available for isotope and tunneling effects associated with proton diffusion in this material. In a similar way, the effect of native point defects in KTO on proton transfer has also not previously been studied.

In the present work, we quantify isotope effects and quantum tunneling effects for proton conduction in defect-free KTO. We also investigated the role of the native point defects in this material.

The activation energy greatly affects the proton conductivity.[6] Here we also compare formation energies in three different cases: a proton far away from both the most preferable native point defect and the compensating defect, a proton close to the most preferable native point defect but far away from the compensating defect, and a proton

close to the compensating defect of the most favorable native point defect but far away from the most preferable native point defect. Examination of the energy barrier of the most preferable native point defect and the barrier of the movement of the defect with a proton paired are also considered, after establishing which defect has the lowest formation energy.

7.2   Calculation methods

We perform DFT calculations using the Vienna *ab initio* Simulation Package (VASP) with the PBE generalized gradient approximation (GGA) functional.[7-10] The projector augmented wave (PAW) method is used for describing the core electrons of each atom.[11] The 1x1x1 cubic unit cell calculations use an $8\times8\times8$ Monkhorst-Pack k-point mesh and an energy cutoff of 600 eV for the lattice calculation. Geometries are relaxed until the forces on all atoms are less than 0.03 eV/Å. Structural optimization of $KTaO_3$ is performed by the conjugate gradient method.

Simulation boxes containing a $2\times2\times2$ cubic unit cells are used, and this represents 40 atoms: 8 (KTO). The DFT optimized lattice parameter is 4.03 Å, in good agreement with the experimental values, 3.998 Å,[12] and a previous DFT calculation.[4] A plane wave basis set is generated on a $4\times4\times4$ Monkhorst-Pack k-point mesh for $2\times2\times2$ cubic unit cell. A cutoff energy of 400 eV is used in optimization calculations involving the proton for the calculation of the binding sites and transition states. Electrons are added to or removed from the supercell in calculations dealing with charged defects to maintain net neutrality in the supercell.

Transition states are computed using the Nudged Elastic Band (NEB) method.[13] For proton diffusion processes involving rotation around on O atom, initial estimates for H positions in NEB calculations are defined such that the OH distance is constant.

7.3   Isotope and tunneling effects

Gomez *et al*. reported DFT calculations for protons in defect-free KTO. They identified oxygen as the proton binding site, and found that proton transfer is a rate-limiting step for proton diffusion.[4] We begin by reproducing these results for defect-free KTO. We first consider proton diffusion in defect-free KTO. Gomez *et al*. calculated an energy barrier of 0.37 eV for proton transfer between adjacent O atoms in KTO and a barrier of 0.21 eV for rotation of a proton around an O atom using PBE-GGA DFT calculations. Our calculations are consistent with those of Gomez *et al*.[4]

There are a variety of applications in which transport of deuterium or tritium is of interest.[14-16] DFT calculations are well suited to examine isotopic effects in diffusion of interstitial H.[17-19] The origins of isotope effects in hopping rates are quite different at high and low temperatures. At low temperatures, diffusion occurs through quantum-mechanical tunneling.[20-22] At high temperatures, proton diffusion can be explained using transition state theory (TST), and isotopic effects arise from the zero point energies (ZPE).[23] We performed DFT calculations to find the vibrational frequencies of protons in KTO to consider isotope effects. To get the vibrational frequencies, only the degree of freedom associated with the proton is considered.

The zero point energies (ZPE) for H^+ isotopes are related to the result obtained for H by

$$E_{D+}^{ZP} = \frac{E_{H+}^{ZP}}{\sqrt{2}}, E_{T+}^{ZP} = \frac{E_{H+}^{ZP}}{\sqrt{3}}. \tag{7.1}$$

H^+ hopping is an activated process, as H^+ should overcome activation energy barriers between oxygen binding sites. Harmonic transition state theory (HTST) offers a useful way to describe hopping rates:[13]

$$k^{HTST} = \frac{\prod_{i=1}^{3} v_i^{min} f(h v_i^{min}/2kT)}{\prod_{j=1}^{2} v_j^{sad} f(h v_j^{sad}/2kT)} \exp\left(-E_a/kT\right) . \tag{7.2}$$

Here, h is Planck's constant and $f(x) = \sinh{(x)}/x$. This HTST description includes the quantization of H vibration, so it accounts for zero-point energy corrections to the classical activation energy, E_a. The isotopic hopping rates in defect-free KTO are shown in Figure 7.1, where it can be seen that the lighter isotope (H^+) hops faster than the heavier isotopes (D^+ and T^+).

In quantum tunneling, tunneling rate becomes more significant with decreasing mass of the moving particle.[13] Consequently, tunneling is the most important mechanism for transitions involving hydrogen. Quantum mechanical tunneling can make a significant contribution to net hopping rates at low temperatures. Several studies have demonstrated methods for accurately predicting the rates of activated hopping and quantum tunneling for H in metals and on metal surfaces by using first-principles DFT to compute the potential energy surface for H.[18]

We examine quantum tunneling effects using the semiclassically corrected harmonic transition state theory (SC-HTST) formulated by Fermann and Auerbach.[24] To apply this formalism, the energies and vibrational frequencies of a proton for the energy minima and transition state are necessary. When only the proton's degree of freedom is considered, an energy minimum has three vibrational frequencies, while a TS has two real frequencies and one imaginary frequency. The results from our calculations are

shown in Figure 7.1. One convenient feature of the Fermann and Auerbach formalism is that it provides a simple estimate of the crossover temperature for an individual hopping transition, T_c, as[24]

$$T_c = \frac{h\nu_{im}\Delta E_{ZP}/k}{(2\pi E_{ZP} - h\nu_{im}\ln 2)} \ , \tag{7.3}$$

where ν_{im} is the imaginary frequency at the TS, h is Planck's constant, k is the Boltzmann constant, and ΔE_{ZP} is zero point energy corrected activation energy defined as[24]

$$\Delta E_{ZP} = (E^{TS} + \sum_{j=1}^{2} \frac{h\nu_j^{TS}}{2}) - (E^{min} + \sum_{i=1}^{3} \frac{h\nu_i^{min}}{2}) \ . \tag{7.4}$$

Tunneling contributions are significant below the transition temperature.[13, 24]

In our case of defect-free KTO, T_c = 277 K, suggesting that tunneling contributions are the dominant mechanism of H$^+$ diffusion for T < 277 K while the importance of tunneling decreases rapidly for T > 277 K.
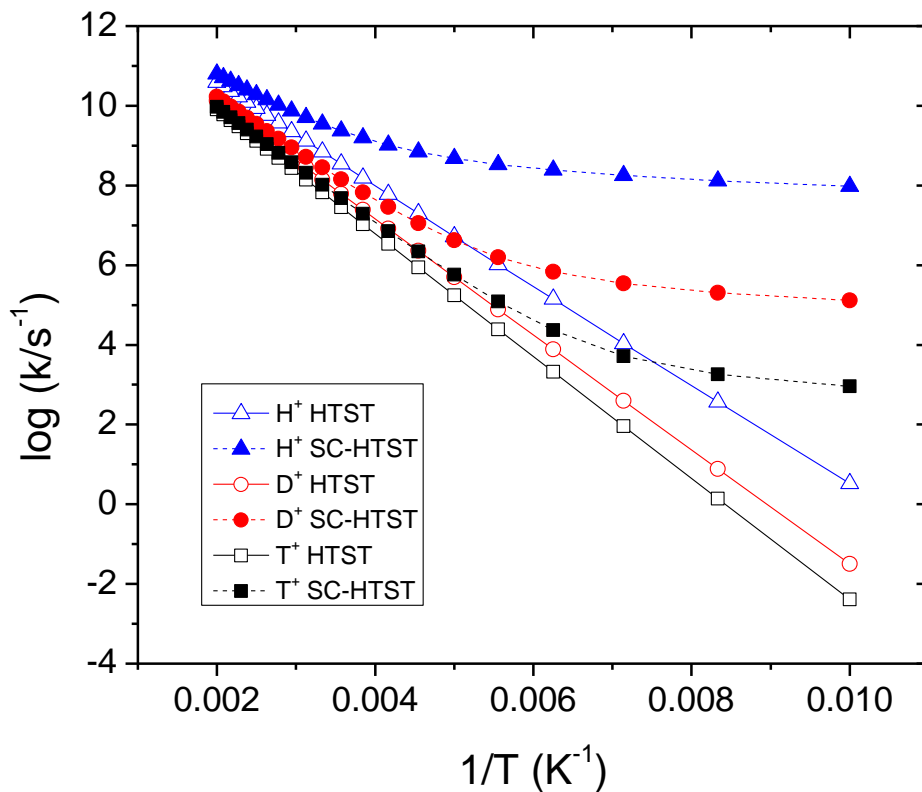
Figure 7.1: The hopping rate for the rate-determining step of H^{+}, D[+], and T[+] diffusion in KTO as predicted by harmonic transition state theory (HTST) and semiclassically corrected harmonic transition state theory (SC-HTST).

7.4   Native point defects in KTaO₃

We next investigate the most preferable native point defect by calculating the formation energies of vacancies in KTaO₃. An important limitation of the results of Gomez *et al.*[4] is that they only considered defect-free perovskites. However, in oxide materials, native point defects are known to exist and they affect diffusion mechanisms.[25] A variety of approaches exist for using DFT calculations to predict the kinds of defects that are relevant in oxides and related materials. For example, Sundell *et al.* investigated defect formation energies in BaZrO₃ perovskite oxide using DFT calculations.[26] Karki *et*

al. studied the formation and migration enegetics and geometric structures of the native point defects and protons in Mg_2SiO_4 by performing DFT simulations.[27] Van der Walle *et al.* also performed DFT calculations to characterize native point defects in ZnO including oxygen vacancies, zinc vacancies, oxygen interstitials, and zinc interstitials.[25] These studies, comparing the formation energies of each point defect, are good examples of approaches to find the most preferable native point defect.

We use DFT calculations to probe the electronic and structural properties of all Schottky-type native point defects in KTO. In Schottky defect formation, vacancies are created in stoichiometric proportions in the bulk crystal. Schottky defect energies are calculated by combining the individual defect energies and lattice energies. In KTO, we consider oxygen, potassium, and tantalum vacancies with different charge states: V_o^q (q = -2, -1, 0, +1, +2), V_K^q (q = -1, 0, +1), and V_{Ta}^q (q = -5, -4, -3, -2, -1, 0, +1, +2, +3, +4, +5).

In the DFT calculations, individual atoms from supercells are removed to create vacancies. We fix the cell shape and volume with a low defect density. The defect formation energy[28] is

$$E_f = \left(E_{tot}^v - E_{tot}^{bulk}\right) - \sum_i n_i \mu_i + q(\varepsilon_F + \varepsilon_v + \Delta V). \qquad (7.5)$$

Here, E_{tot}^v and E_{tot}^{bulk} are the total energies of a supercell including the defect, and a defect-free supercell, ε_F is the Fermi level, ε_v is the valence band maximum in the bulk, and ΔV is a factor that adjusts the electrostatic potential to set the average potential in a bulk-like region of the defect-containing supercell equal to the average potential in the defect-free supercell. The relevant Fermi energy value for a wide band-gap material like

KTO is found by determining the system with the lowest formation energy that is charge neutral overall.

The results for Schottky defects generated by combining various vacancies are shown in supporting information in Figure 7.A.1. The charges are controlled by the total number of electrons in the supercell[29]. Our calculations show that oxygen vacancies with a net charge of 2^+ have the lowest formation energy among all the defects we consider. This implies that the dominant native point defect in KTO is an oxygen vacancy. In a neutral system, O vacancies with a net charge of 2^+ net charges must be balanced by K vacancies with a net charge of 1^- for the charge neutrality.

7.5   Vacancy concentrations in KTaO₃

Once we find the most preferable native point defect, it is important to know the concentration of these vacancies. The concentration of a point defect is directly related to its formation energy, E_f. The concentration can be expressed in thermodynamic equilibrium as[25]

$$C = N\exp\left(-\frac{E_f}{kT}\right).$$ (7.6)

Here, N is the number of possible vacancy sites. A definition of the ideal gas chemical potential for O_2 is[13]

$$\mu_{O_2} = E_{O_2} + \mu^0_{O_2} + kT \ln\left(\frac{P_{O_2}}{P^0}\right).$$ (7.7)

Here, E_{O_2} is total energy of gaseous oxygen, $\mu^0_{O_2}$ is chemical potential of gaseous oxygen at the standard state, and P_{O_2} is partial pressure of oxygen.

In the presence of water vapor, protons are generated when water is absorbed into the oxygen vacancies. Specifically, hydroxyl ions fill the oxygen vacancies due to the presence of water vapor[30].

$$H_2O(g) + V_O^{\cdot\cdot} + O_O^{x} \leftrightarrow 2OH_O^{\cdot}. \tag{7.8}$$
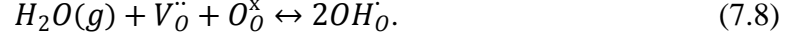
Here, $V_O^{\cdot\cdot}$ are oxygen ion vacancies, $OH_O^{\cdot}$ is a positively charged protonic defect, and O_O^{x} is an oxygen lattice site. Oxygen originates from water vapor as

$$H_2O(g) \leftrightarrow H_2(g) + \frac{1}{2}O_2(g). \tag{7.9}$$
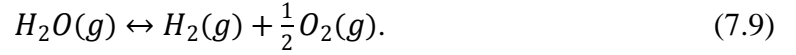
Once we know the equilibrium constant of the above reaction, we can describe partial pressure of oxygen as a function of water and hydrogen partial pressure, respectively.

$$P_{O_2} = \frac{K_P(P_{H_2O})^2}{(P_{H_2})^2}. \tag{7.10}$$

Here, K_P is a temperature-dependent equilibrium constant for the reaction in Equation (7.9).

$$\mu_{O_2} = E_{O_2} + \mu_{O_2}^0 + kT \ln\left(\frac{1}{P^0}\frac{K_P(P_{H_2O})^2}{(P_{H_2})^2}\right). \tag{7.11}$$

We use the moisture condition of 3% water vapor with the remaining 97% of the gas phase being hydrogen.[31]

From Equations (7.5) and (7.6), the defect concentration can be represented as,

$$C = N\exp\left(-\frac{1}{kT}\left((E_{tot}^v - E_{tot}^{bulk}) - \sum_i n_i\mu_i + q(\varepsilon_F + \varepsilon_v + \Delta V)\right)\right). \tag{7.12}$$

This equation shows that defects with high formation energies will occur in low concentrations. The vacancy concentrations under physically relevant conditions are also very low as shown in Figure 7.2, so determining the properties of a vacancy in a DFT calculation representing a vacancy surrounded by a large region of vacancy-free material is appropriate.
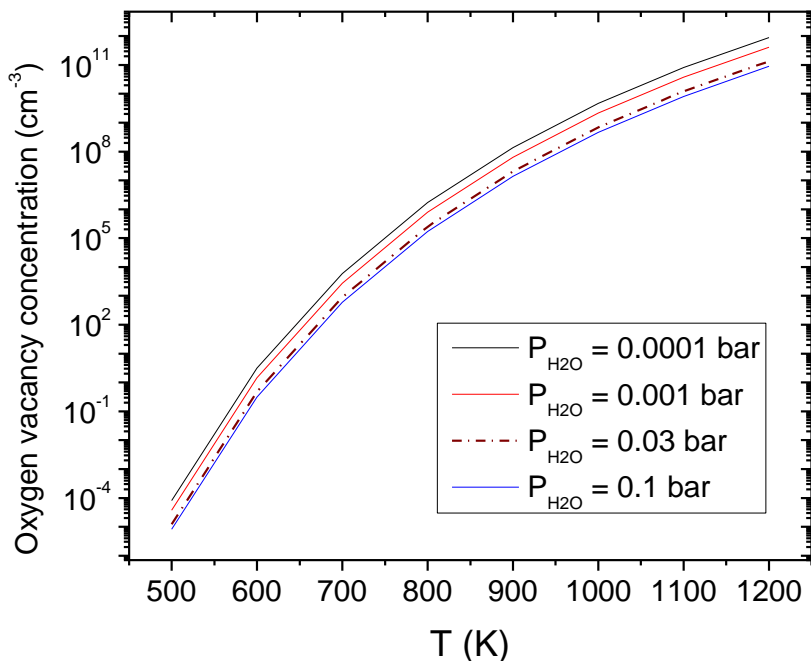
Figure 7.2: Oxygen vacancy concentrations in KTO calculated at P_{H2O} = 0.0001, 0.001, 0.03, and 0.1 bar.

7.6   Proton and defect interactions in KTaO$_3$

Since we know V_O^{2+} and V_K^- are the preferential point and compensating defects in KTaO$_3$, respectively, it is important to consider the interactions between H$^+$ and V_O^{2+} as well as between H$^+$ and V_K^-. We examine the energy barrier for proton motion near the previously identified O vacancies using NEB calculations similar to those outlined above in section 7.2. The energy barrier for proton transfer in the system with an oxygen vacancy is found to be 0.162 eV. However, in order to examine the net activation energy barrier, we investigate the formation energy, since this migration energy is insufficient for characterizing the net diffusion of protons. Thus, it is essential to consider the formation energy of H$^+$ close to V_O^{2+} and far away from V_K^-. These calculations show

that protons do not prefer positively charged oxygen vacancy sites. That is, oxygen vacancies make the nearest possible proton-hopping sites metastable states by acting as anti-trapping sites for protons, as seen by the O vacancy in Figure 7.3. Protons do not favorably bind at the oxygen vacancies due to charge repulsion. However, we find that there is an attractive charge interaction between H^+ and V_K^-. The energy barrier for protons to transfer to another oxygen-binding site in this case is 0.57 eV. When we study the formation energy of H^+ close to V_K^- and far away from V_O^{2+}, we find that formation energy decreases with proton proximity to V_K^-, demonstrating that V_K^- acts as a trap site for protons. This behavior can be observed in the K vacancy of Figure 7.3. This result can be explained by the Coulomb attraction between V_K^- and H^+. The results suggest that this electrostatic attraction between V_K^- and H^+ could be a factor inhibiting the mobility of protons in KTO. A detailed description of formation energy in each case is shown in Appendix 7.A.2 and 7.A.3.
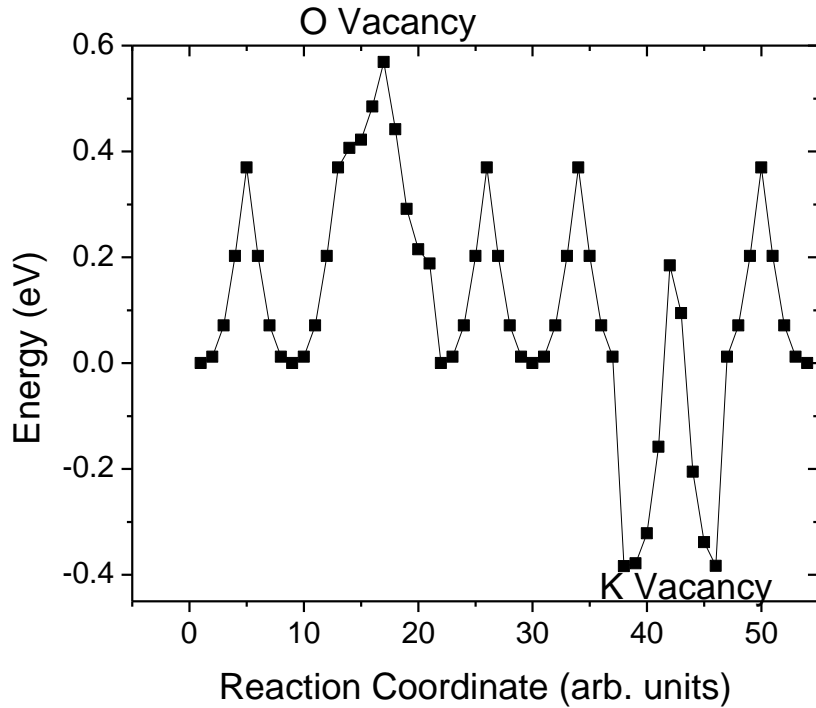
Figure 7.3: 1D potential energy surface (PES) of a proton, when it is far away from oxygen and potassium vacancies, or either near an oxygen vacancy or a potassium vacancy.

7.7   Diffusivity of H^+ in $KTaO_3$ perovskites with V_O^{2+}

We study how proton diffusivity is affected by the presence of oxygen vacancies. We consider all the possible hoppings, including transfer and rotation, to obtain the net diffusivity for protons in KTO with an oxygen vacancy. There are five distinct barriers to proton transfer, with four different barriers for proton rotation to different environments. Distances between the proton and the oxygen vacancy that are larger than sixth nearest neighbor are considered bulk cases.

Table 7.1: Complete lists of energy barriers for proton diffusion. 2N is the nearest neighbor distance, 3N is the next nearest neighbor distance, 4N is the next next nearest neighbor distance, 5N is the next next next nearest neighbor distance, and 6N is the next next next next nearest neighbor distance between the proton and the oxygen vacancy.

	Initial distance of proton from V_O^{2+}	Final distance of proton from V_O^{2+}	Energy barrier (eV)
Transfer 1	2N	4N	0.161
Transfer 2	4N	2N	0.382
Transfer 3	3N	3N	0.396
Transfer 4	3N	6N	0.296
Transfer 5	6N	3N	0.437
Rotation 1	2N	3N	0.152
Rotation 2	3N	2N	0.313
Rotation 3	3N	5N	0.457
Rotation 4	5N	3N	0.066

Once we have our complete lists of calculations for the energy barriers in transfer and rotation up to 6N, we calculate vibrational frequencies at energy minima and at TS, allowing only the proton to relax in order for us to obtain the hopping rates (s^{-1}) by Harmonic Transition State Theory (HTST)[13]. Upon obtaining the hopping rates for the proton, we perform KMC (Kinetic Monte Carlo) to calculate the net diffusivity of the proton in $KTaO_{3-\delta}$.

In our KMC simulations, we define a simulation volume consisting of randomly arranged oxygen vacancies. The sizes of simulation volume are 2×2×2, 3×3×3, 4×4×4, 5×5×5, and 6×6×6 unit cells, each limited to a single oxygen vacancy. The hopping dynamics of protons are then simulated using a simple algorithm that reproduces the absolute rate for each local hop[13]. At each time step in our KMC, we randomly choose a proton from all the protons in the simulation volume and a move direction of a proton from the 2 (2) possible directions available for transfer (rotation). Hops are accepted based on a probability, the ratio of the attempted hopping rate to the maximum hopping

rate possible in the simulation volume. Regardless of the outcome of the attempted hop, time is incremented by $1/4 \, k_{fast}N_{H+}$, where N_{H+} is the number of protons in the simulation volume and k_{fast} is the fastest hopping rate for all possible hops in the volume. An Einstein relation is used to determine the diffusivity.[32-34] The slope of the mean square displacement (msd) is related to the diffusion coefficient.

We calculate the diffusivity of protons as a function of the oxygen vacancy concentration. In our KMC, the position of an oxygen vacancy is randomly chosen.

Our calculations use oxygen vacancy concentrations of 1/24 (4.17%), 1/81 (1.23%), 1/192 (0.52%), 1/375 (0.27%), and 1/648 (0.15%). We find that diffusivity of a proton decreases as oxygen vacancy concentration increases. In other words, as the concentration of oxygen vacancies decrease, diffusivity of a proton approaches the defect-free case. Thus, the effect of oxygen vacancies on proton diffusivity is much smaller at the calculated oxygen vacancy concentrations.
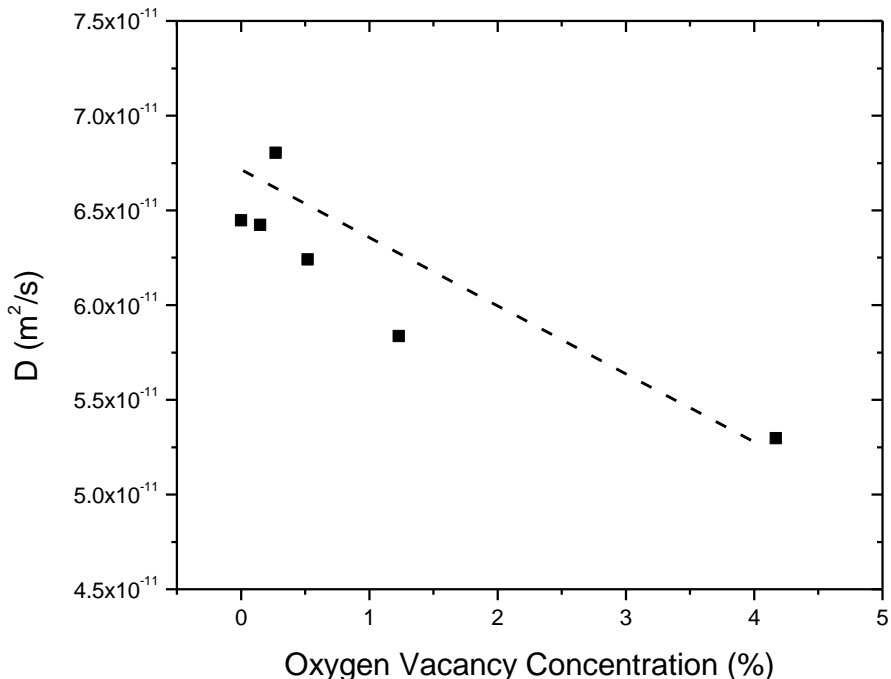
Figure 7.4: Proton diffusivity D (m^2/s) at different oxygen vacancy concentrations (%).The dashed line shows the trend of D as a function of oxygen vacancy concentration.

7.8   Mechanisms for migration of oxygen vacancy and hydroxyl in KTaO$_3$ perovskites

We next consider the migration of oxygen vacancies, which are the most favorable native point defects in KTO. The relationship between oxygen ion diffusion in KTO and its crystal structure at intermediate or low temperatures has not been studied until now.

There can be oxygen vacancy migration when a nearest neighbor oxygen atom in the oxygen lattice hops into the vacant site.[25] We calculated the energy required to move oxygen vacancies using the same methods employed for proton migration. Oxygen vacancy migration in KTaO$_3$ occurs through a curved pathway around the edge of the

TaO_6 octahedron, as shown in Figure 7.5. The activation energy for an oxygen vacancy to migrate is 0.79 eV. It was previously shown that the activation energy barrier for proton transfer to another oxygen binding site is 0.37 eV in defect-free KTO. In other words, it is more difficult for oxygen vacancies to migrate than it is for protons to transfer. This smaller activation energy for proton conduction can help lower the operating temperature,[35] a desirable property for a proton-conducting membrane.
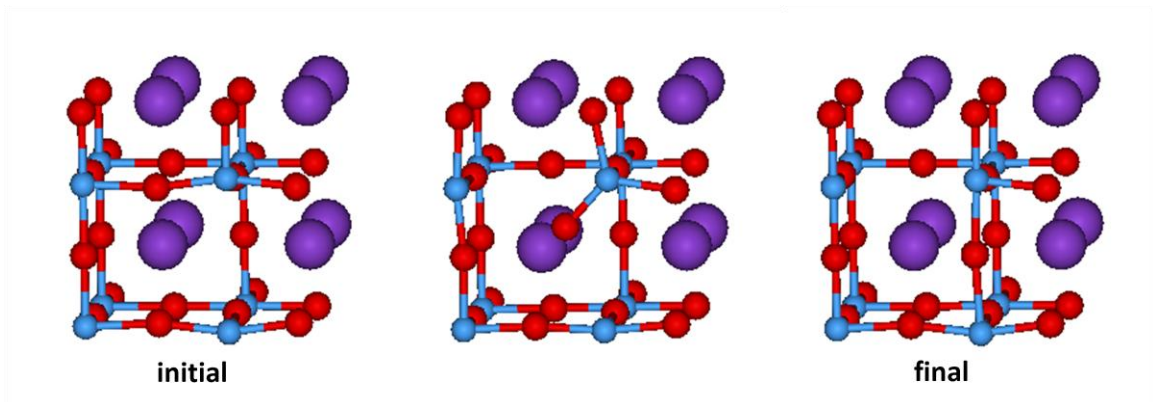
Figure 7.5: The mechanism for an oxygen vacancy migration.

To examine how protons bonded to oxygen atoms behave during oxygen vacancy migration, movement of hydroxyl groups is also investigated, as shown in Figure 7.6. When we consider hydroxyl group migration, the activation energy for the group to migrate is 0.42 eV. The activation energy for oxygen vacancy migration with protons is lower than the value for bare oxygen vacancy migration by 0.37 eV.
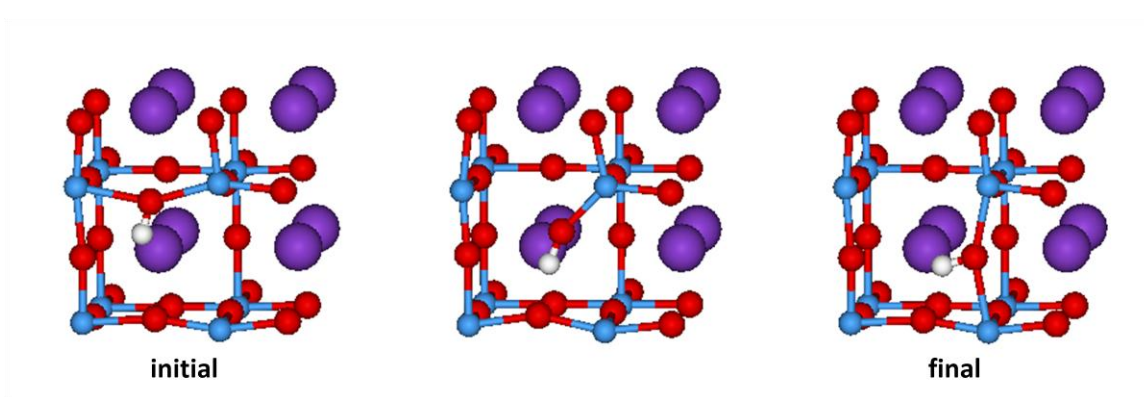
Figure 7.6: The mechanism of a hydroxyl group migration.

7.9 Conclusion

We use density functional theory (DFT) to investigate properties of $KTaO_3$ (KTO) including isotope effects and quantum tunneling effects, both of which can be significant for light materials. At elevated temperatures, characteristic of applications involving proton-conducting perovskites, tunneling is negligible, but zero point energy effects still lead to non-negligible isotope effects for H^+, D^+, and T^+.

Tunneling contributions are the dominant feature of H^+ diffusion for only low temperature regions. We also elucidate the proton conduction mechanism near the most favorable native point defect and the compensating defect. With respect to proton transport, we observe Coulomb charge repulsion between the proton and the oxygen vacancy, with the oxygen vacancy being the most preferable native point defect in KTO. In the case where protons are near the oxygen vacancy, the formation energy is higher than the formation energy of the other two cases examined (close to a potassium vacancy, and distant from both oxygen and potassium vacancies). This high formation energy makes the oxygen vacancy site an anti-trap site for protons. We find that energy barriers to transfer are larger compared to the transport in defect-free KTO due to Coulomb

attraction between V_K^- and H^+. This electrostatic attraction may be a factor inhibiting the mobility of protons in KTO. However, in terms of formation energy, when protons are near V_K^-, the lowest formation energy is noted among the cases investigated. From this perspective, we find that potassium vacancy sites are the trap sites, while oxygen vacancy sites act as anti-trap sites for the protons from our potential energy surface (PES) analysis. We also find that diffusivity of a proton decreases as oxygen vacancy concentration increases. This effect of oxygen vacancies on proton diffusivity is predicted to be small in KTO due to the low oxygen vacancy concentration.

The barrier to migration for oxygen vacancies is higher than the energy barrier for protons jumping to another oxygen binding site in the case where protons are far away from V_O^{2+} and V_K^-. This implies that $KTaO_3$ is desirable as a proton-conducting material because there is less oxygen movement due to its higher energy barrier. However, the energy barrier for an oxygen vacancy may be lowered by 0.37 eV by introducing a proton and allowing transfer to occur via a hydroxyl group.

7.10   References

1.   Iwahara, H., Esaka, T., Uchida, H., Maeda, N., *Solid State Ionics* **1981**, 3-4, 359.
2.   Agmon, N., *Chem. Phys. Lett.* **1995**, 244, 456.
3.   Kreuer, K. D., Dippel, Th., Hainovsky, N. G., Maier, J., *Ber. Bunsenges. Phys. Chem.* **1992**, 96, 1736.
4.   Gomez, M. A., Jindal, S., Fletcher, K. M., Foster, L. S., Addo, N. D. A., Valentin, D., Ghenoiu, C., Hamilton, A., *J. Chem. Phys.* **2007**, 126, 194701.
5.   Wemple, S. H., *Phys. Rev.* **1965**, 137, 1575.
6.   Shi, C. S., Morinaga, M., *J. Comput. Chem.* **2006**, 27, 711-718.
7.   Perdew, J. P., Chevary, J. A., Vosko, S. H., Jackson, K. A., Pederson, M. R., Singh, D. J., Fiolhais, C., *Phys. Rev. B* **1992**, 46, 6671-6687.
8.   Kresse, G., Hafner, J., *Phys. Rev. B* **1993**, 47, 558-561.
9.   Kresse, G., Furthmuller, J., *Phys. Rev. B* **1996**, 54, 11169-11186.
10.   Vanderbilt, D., *Phys. Rev. B* **1990**, 41, 7892-7895.
11.   Kresse, G., Joubert, D., *Phys. Rev. B* **1999**, 59, 1758.

12. Shirane, G., Newnham, R., Pepinsky, R., *Phys. Rev.* **1954**, 96, 581-588.
13. Sholl, D. S., Steckel, J. A., Density Functional Theory: A Practical Introduction (Wiley, Hoboken, NJ, 2009).
14. Mukundan, R., Brosha, E. L., Birdsell, S. A., Costello, A. L., Garzon, F. H., Willms, R. S., *J. Electrochem. Soc.* **1999**, 146, 2184-2187.
15. Iwahara, H., Asakura, Y., Katahira, K., Tanaka, M., *Solid State Ionics* **2004**, 168, 299-310.
16. Nowick, A. S., Vaysleyb, A. V., *Solid State Ionics* **1997**, 97, 17-26.
17. Semidey-Flecha, L., Hao, S. Q., Sholl, D. S., *J. Taiwan Inst. Chem. Eng.* **2009**, 40, 246-252.
18. Bhatia, B., Sholl, D. S., *Phys. Rev. B* **2005**, 72, 224302.
19. Carter, E. A., Johnson, D. F., *J. Mater. Res.* **2010**, 25, 315-327.
20. Sundell, P. G., Bjorketun, M. E., Wahnstrom, G., *Phys. Rev. B* **2007**, 76, 094301.
21. Bell, R. P., The Tunnel Effect in Chemistry (Chapman and Hall, London, 1980).
22. Gol'danskii, V. I., Trakhtenberg, L. I., Fleurov, V. N., Tunneling Phenomena in Chemical Physics (Gordon and Breach Science, New York, 1989).
23. Swain, C. G., Stivers, E. C., Reuwer, J. F., Schaad, L. J., *J. Am. Chem. Soc.* **1958**, 80, 5885.
24. Fermann, J. T., Auerbach, S., *J. Chem. Phys.* **2000**, 112, 6787-6794.
25. Janotti, A., Van de Walle, C. G., *Phys. Rev. B* **2007**, 76, 165202.
26. Sundell, P. G., Bjorketun, M. E., Wahnstrom, G., *Phys. Rev. B* **2006**, 73, 104112.
27. Ashok K. Verma, B. B. K., *Earth Planet. Sci. Lett.* **2009**, 285, 140-149.
28. Van de Walle, C. G., Neugebauer, J., *J. Appl. Phys.* **2004**, 95, 3851-3879.
29. Luo, X., Wang, B., Zheng, Y., *Phys. Rev. B* **2009**, 80, 104115.
30. Islam, M. S., Slater, P. R., Tolchard, J. R., Dinges, T., *Dalton Trans.* **2004**, 19, 3061.
31. Chen, X. J., Liu, Q. L., Chan, S. H., Brandon, N. P., Khor, K. A., *Electrochem. Commun.* **2007**, 9, 767-772.
32. Kamakoti, P., Sholl, D. S., *Phys. Rev. B* **2005**, 71, 014301.
33. Kang, S. G., Coulter, K. E., Gade, S. K., Way, J. D., Sholl, D. S., *J. Phys. Chem. Lett*. **2011**, 2, 3040.
34. Semidey-Flecha, L., Sholl, D. S., *J. Chem. Phys.* **2008**, 128, 144701.
35. Quarez, E., Noirault, S., Caldes, M. T., Joubert, O., *J. Power Sources* **2010**, 195, 1136-1141.
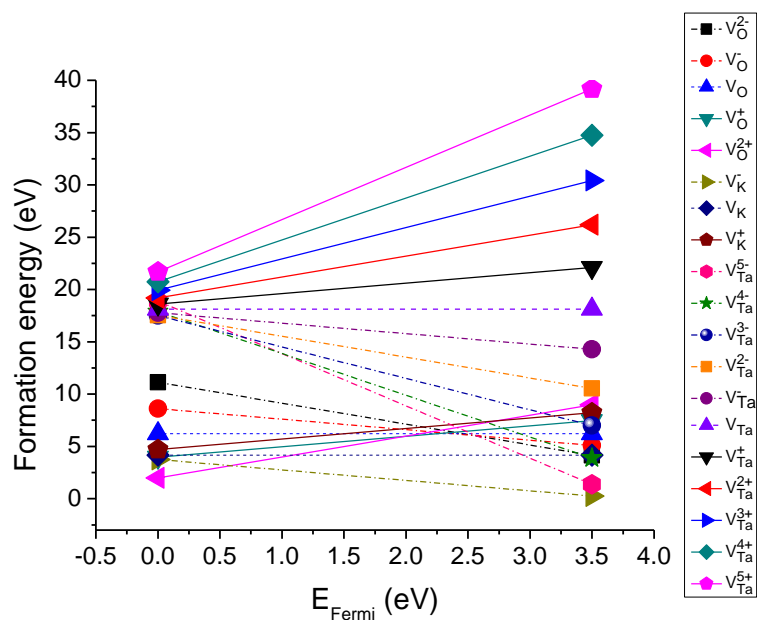
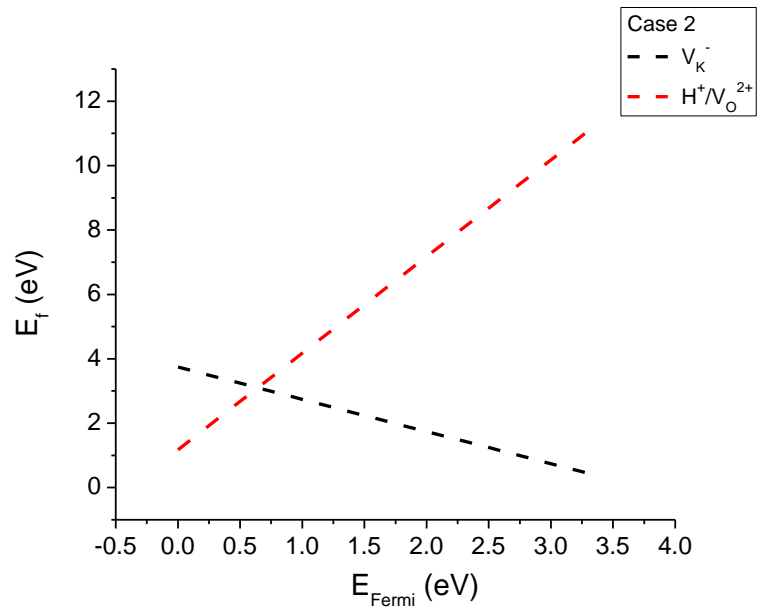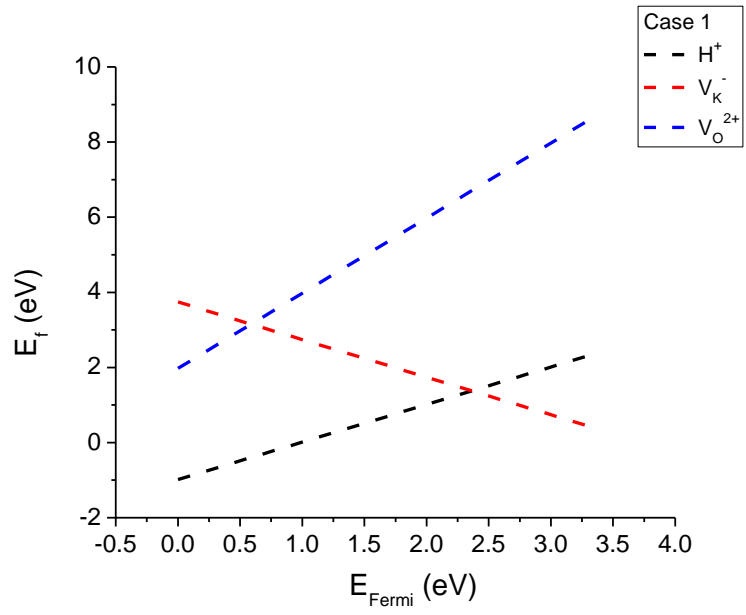**Figure 7.A.1**: Calculated formation energies for Schottky defects in $KTaO_3$.
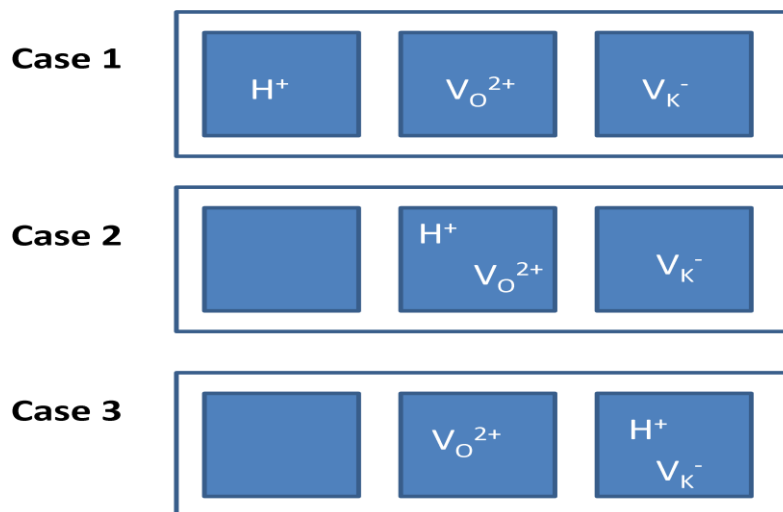
Figure 7.A.2: Schematic of cases for a proton near vacancies in $KTaO_3$. A proton is far away from both an oxygen vacancy and a potassium vacancy in Case 1. The proton is near an oxygen vacancy and far away from a potassium vacancy in Case 2, and *vice versa* in Case 3.
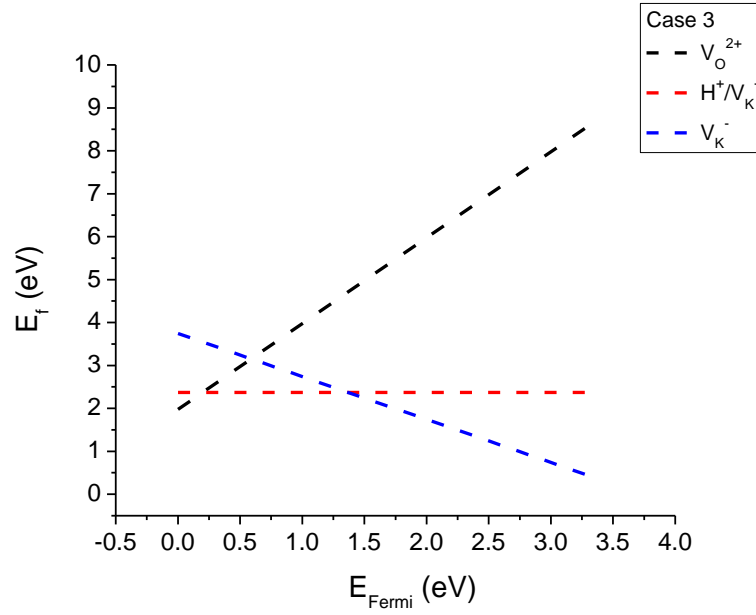
Figure 7.A.3: Calculated formation energies in $KTaO_3$ for H^+, V_K^-, and V_O^{2+} in Case 1, for V_K^- and $H^+V_O^{2+}$ in Case 2, and for V_O^{2+}, $H^+V_K^-$, and V_K^- in Case 3.

Case 1: $E_f = E_f(H^+) + 3\ E_f(V_K^-) + E_f(V_O^{2+})$,

Case 2: $E_f = 3\ E_f(V_K^-) + E_f(H^+V_O^{2+})$,

Case 3: $E_f = E_f(V_O^{2+}) + E_f(H^+V_K^-) + 2E_f(V_K^-)$.

CHAPTER 8

CHEMICAL STABILITY STUDIES OF LI GARNET-RELATED STRUCTURES

8.1   Introduction

Solid-state Li-ion electrolytes have been considered as good replacements for liquid organic electrolytes because of their safety and low cost.[1] However, the lithium ionic conductivity of solid-state ion conductors is lower than that of liquid organic electrolytes.[2] Therefore, it is important to improve ionic conductivity of solid-state electrolytes. A longstanding aim in development of electrolytes has been to find conductors that give high Li-ion conductivity coupled with low electronic conductivity.[1, 2] Chemical stability is also important for solid-state Li-ion batteries.[3]

Lithium ion conduction has been studied for a wide range of crystalline metal oxides. Lithium phosphorus oxynitride (LiPON) has been used as a thin-film solid state electrolyte, but it has low lithium ion conductivity.[4-7] $Li_{14}ZnGe_4O_{16}$ (LISICON) shows high lithium ion conductivity, but the conductivity decreases with time; the material is highly reactive with Li-metal, and its CO_2 stability is limited.[8] $Li_{1.3}Ti_{1.7}Al_{0.3}(PO_4)_3$ (NASICON) is not stable with Li-metal.[8] Perovskite-type (Li, La)TiO_3 has very high lithium ion conductivity compared to other oxides, but this material is electrochemically unstable.[9-11] Li-ion conductors with garnet-like structures have been considered as potential electrolyte materials in solid-state lithium batteries due to their high conductivity and electrochemical stability.[1, 12] For example, $Li_5La_3Nb_2O_{12}$ and $Li_5La_3Ta_2O_{12}$ have been examined as Li-ion conductors.[13] $Li_5La_3Nb_2O_{12}$ and

$Li_5La_3Ta_2O_{12}$ have higher ionic conductivities than LiPON, Li_9AlSiO_8, and Li-β-alumina.[13] $Li_7La_3Zr_2O_{12}$, with a cubic garnet-related type structure, has been considered a promising solid electrolyte for solid-state lithium ion batteries, since it has high Li-ion conductivity as well as high chemical stability.[12] The structure of $Li_7La_3Sn_2O_{12}$ has been reported as tetragonal with a low Li-ion conductivity.[14, 15] Tetragonal $Li_7La_3Hf_2O_{12}$ has also been studied as a new garnet-related fast Li-ion conductor.[16]

In considering garnets for Li-ion conducting applications, the study for chemical stability is highly important. In this study, we examine the chemical stability of $Li_7La_3Zr_2O_{12}$, $Li_7La_3Sn_2O_{12}$, and $Li_7La_3Hf_2O_{12}$ with respect to the carbonate and hydroxide formation reactions.

8.2   Calculation methods

In this chapter, we study the chemical stability of $Li_7La_3Zr_2O_{12}$, $Li_7La_3Sn_2O_{12}$, and $Li_7La_3Hf_2O_{12}$ which are the only available crystalline compounds with the stoichiometry of $Li_7La_3M_2O_{12}$ (where M = tetravalent metal) from the Inorganic Crystal Structure Database (ICSD)[17]. In this study, the Vienna *ab initio* Simulation Package (VASP), with the PW91 generalized gradient approximation (GGA) functional, is employed to calculate the electronic structure of solid oxides, hydroxides, and carbonate materials. All calculations are done using the projector augmented wave (PAW) pseudopotentials to describe the core electrons of each atom.[18] Plane wave basis sets are used with a cutoff of 500 eV. *k*-points are obtained using the Monkhorst–Pack method,[19] with the number of *k*-points chosen to give a spacing of about 0.028 Å^{-1} along the axes of the reciprocal unit cells in our bulk calculations.

We use a single unit cell to optimize the bulk crystal structure of each compound we study. The initial structures for geometry relaxations are obtained from the experimental data available from ICSD.[17] Geometry is relaxed until the forces on all atoms are less than 0.03 eV/Å with a conjugate gradient method algorithm. As an example, the optimized crystal structure of $Li_7La_3Sn_2O_{12}$ is shown in Figure 8.1.
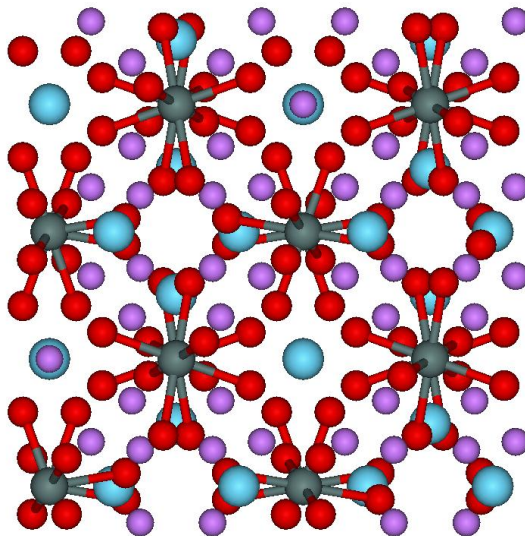

Figure 8.1: The optimized crystal structure of tetragonal $Li_7La_3Sn_2O_{12}$ where the purple spheres are lithium, red spheres are oxygen, blue spheres are lanthanum, and grey spheres are tin.

To assess chemical stability, we compute the vibrational density of states (VDOS) of solid compounds in order to determine the reaction free energy for carbonate and hydroxide formation reactions at finite temperature, $\Delta G(T)$, within the harmonic approximation.[20] In a variety of metal hydride decomposition reactions and pervoskite carbonate formation reactions, these first-principles calculations have been shown to yield reaction free energies that are accurate within about 10 kJ/mol.[21, 22] For these VDOS calculations, we use the PHONON code developed by Parlinski,[23] and with this information, we calculate the relevant reaction free energies. These VDOS calculations

require computing the force constant matrix of each atomic interaction in a periodic material via finite difference approximations calculated from DFT total energy calculations. Structures with a displacement magnitude of 0.03 Å of the nonequivalent atoms are generated from the optimized supercells.

Pressure-volume (PV) contributions because of changes in the volumes of the solid phases are ignored, since the volume change associated with gaseous CO_2 and H_2O is relatively larger than the volume changes in the solid components. Gas phase CO_2 and H_2O are treated as ideal gases. The free energies of CO_2 and H_2O are defined from standard statistical mechanics as [24]

$$G_{CO2} = \frac{7}{2}RT + \sum_{i=1}^{4} \frac{N_a h v_i}{e^{h v_i / kT} - 1} - T S_{CO2}(T) , \qquad (8.1)$$

$$G_{H2O} = 4RT + \sum_{j=1}^{3} \frac{N_a h v_j}{e^{h v_j / kT} - 1} - T S_{H2O}(T) , \qquad (8.2)$$

where N_a is Avogadro's constant, R is a gas constant, T is the temperature, v_i are the vibrational frequencies of CO_2, and v_j are the vibrational frequencies of H_2O in Equation (8.1) and (8.2), respectively. The vibrational frequencies of a CO_2 molecule are 673 (π_u), 1354 (σ_g^+), and 2397 cm^{-1} (σ_u^+),[25] and the vibrational frequencies of an H_2O molecule are taken as 3657.05 (v_1), 1594.75 (v_2), and 3755.93 cm^{-1} (v_3).[26] The Shomate equation is employed to obtain the entropy of CO_2 and H_2O.[27]

8.2.1 DFT calculated results of geometry optimization

The optimized lattice constants for each compound considered in this work are presented in Table 8.1 along with the corresponding experimental data. We use available experimental lattice constants from the Inorganic Crystal Structure Database (ICSD) as input structures.[17] Predicted values agree with experimental lattice constants and angles, although all the calculated lattice constants with the GGA functional are slightly larger than the experimental lattice constants.

We calculated the optimized unit cell volume with all the atoms and unit cell size and shape allowed to relax for each material except the disordered cubic structure of $Li_7La_3Zr_2O_{12}$. $Li_7La_3Zr_2O_{12}$ has two different structures: a disordered cubic phase and an ordered tetragonal structure.[12, 19, 28-32] For the cubic disordered structure of $Li_7La_3Zr_2O_{12}$, we randomly choose 10 different configurations with the restriction that there are no pairs of nearest neighbors of Li as adjacent $96h$ pairs, or adjacent pairs of $24d$ and $96h$ sites occupied at the same time.[33]

We use the lowest energy structure among the 10 different structures for further consideration. We fix unit cell shape at the DFT-optimized structure for cubic phase of $Li_7La_3Zr_2O_{12}$ to maintain the cubic structure. By manually changing the lattice constants, we obtain the optimized lattice constant at 13.059 Å in Figure 8.2.
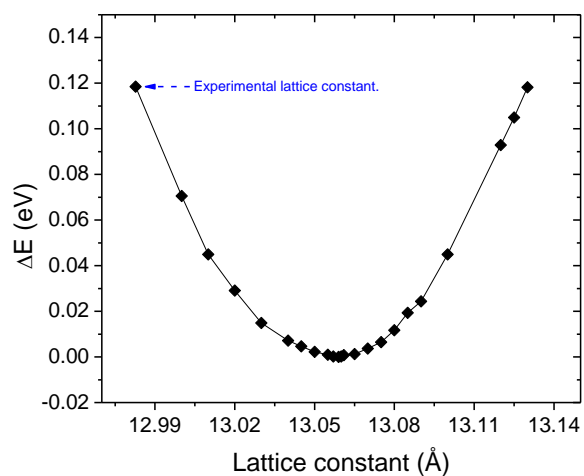
Figure 8.2: Relative total energy, ΔE, of a disordered cubic structure of $Li_7La_3Zr_2O_{12}$ as a function of the lattice constant. Data points are from DFT calculations.

Table 8.1: Comparison of the experimental[17] and the DFT calculated structural parameters for the 8 crystalline compounds considered in our calculations, with all lengths in Å and angles in degrees.

Compound	Space group	Structural Parameters (Å, degree)	
		Experimental	Calculated
ZrO_2	*P12₁/c1*	$a = 5.143$ $b = 5.204$ $c = 5.310$ $\beta = 99.166$	$a = 5.212$ $b = 5.286$ $c = 5.386$ $\beta = 99.574$
SnO_2	*P42/MNM*	$a = 4.733$ $c = 3.182$	$a = 4.820$ $c = 3.240$
HfO_2	*P12₁/c1*	$a = 5.113$ $b = 5.172$ $c = 5.295$ $\beta = 99.188$	$a = 5.123$ $b = 5.188$ $c = 5.294$ $\beta = 99.716$
Li_2CO_3	*C12/c1*	$a = 8.353$ $b = 4.974$ $c = 6.189$ $\beta = 114.677$	$a = 8.452$ $b = 5.045$ $c = 6.329$ $\beta = 115.051$
$Li_7La_3Zr_2O_{12}$	*I41/acdZ*	$a = 13.134$ $c = 12.664$	$a = 13.225$ $c = 12.669$
$Li_7La_3Zr_2O_{12}$	*Ia-3d*	$a = 12.983$	$a = 13.059$
$Li_7La_3Sn_2O_{12}$	*I41/acdZ*	$a = 13.121$ $c = 12.547$	$a = 13.256$ $c = 12.554$
$Li_7La_3Hf_2O_{12}$	*I41/acdZ*	$a = 13.106$ $c = 12.630$	$a = 13.179$ $c = 12.586$
LiOH	*P4/nmms*	$a = 3.557$ $c = 4.339$	$a = 3.585$ $c = 4.403$

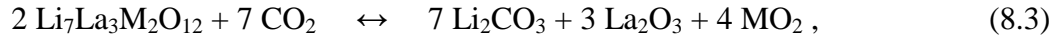**Table 8.2:** Comparison of the DFT total energy of the cubic and tetragonal structure of $Li_7La_3Zr_2O_{12}$.

Structure	E/f.u (eV)	ΔE (E-E$_{lowest}$) (eV)
Cubic	-172.317	0.06
Tetragonal	-172.379	0

From the comparison of the cubic and tetragonal structure of $Li_7La_3Zr_2O_{12}$, we find that the tetragonal structure is more stable at 0 K than the cubic structure by 0.06 eV/formula unit (see Table 8.2). Therefore, we use the tetragonal structure for the later calculation of thermodynamic properties to assess the chemical stability of $Li_7La_3Zr_2O_{12}$ in CO_2 and H_2O containing environments. If the cubic phase is more stable than the tetragonal phase at finite temperatures, our use of the tetragonal phase in our stability calculations may lead to underestimation of the material's stability.

8.3   Chemical stability

The carbonate formation reactions in the presence of CO_2 and the hydroxide formation reactions in the presence of H_2O of $Li_7La_3Zr_2O_{12}$, $Li_7La_3Sn_2O_{12}$, and $Li_7La_3Hf_2O_{12}$ can be given as

$$2\ Li_7La_3M_2O_{12} + 7\ CO_2 \quad \leftrightarrow \quad 7\ Li_2CO_3 + 3\ La_2O_3 + 4\ MO_2 \,, \tag{8.3}$$

$$2\ Li_7La_3M_2O_{12} + 7\ H_2O \quad \leftrightarrow \quad 14\ LiOH + 3\ La_2O_3 + 4\ MO_2 \,, \tag{8.4}$$

where M = Zr, Sn, or Hf.

The van't Hoff relation provides an expression for carbonate formation:

$$\frac{P_{CO2}}{P_0} = \exp\left(\frac{\Delta G}{RT}\right) \tag{8.5}$$

$$\Delta G(T) = \Delta E_0 - n_1 G_{CO2}(T) + \Delta F^{solids}(T) \,, \tag{8.6}$$

$$\Delta G(T) = \Delta E_0 - n_2 G_{H2O}(T) + \Delta F^{solids}(T) \,, \tag{8.7}$$

where ΔE_0 is the difference of ground state total energy determined using DFT between the reactants and products, ΔG is the Gibbs free energy difference between the reactants and products, n_1 is the number of moles of CO_2 involved in the reaction, G_{CO2} is the free energy of CO_2, n_2 is the number of moles of H_2O involved in the reaction, G_{H2O} is the free energy of H_2O, ΔF^{solids} is the vibrational free energy change between the solids of products and reactants, and P_0 is the standard state reference pressure.

Figure 8.3 reports predicted calculations with $P_0 = 1$ bar for the equilibrium CO_2 pressure of carbonate formation for $Li_7La_3Zr_2O_{12}$, $Li_7La_3Sn_2O_{12}$, and $Li_7La_3Hf_2O_{12}$. Similarly, the equilibrium H_2O pressure related to hydroxide formation of $Li_7La_3Zr_2O_{12}$, $Li_7La_3Sn_2O_{12}$, and $Li_7La_3Hf_2O_{12}$ as predicted by our calculations is shown in Figure 8.4, using $P_0 = 1$ bar. We indicate the temperature at which carbonate/hydroxide formation becomes favorable as T*. As the CO_2 pressure is increases, the critical temperature increases for the carbonate and hydroxide formation reactions as seen in Table 8.3 for all three materials.

Table 8.3: Critical temperature of $Li_7La_3Zr_2O_{12}$, $Li_7La_3Sn_2O_{12}$, and $Li_7La_3Hf_2O_{12}$ at the different pressures of CO_2 and H_2O.

P_{CO2} (bar)	T* (K), $Li_7La_3Zr_2O_{12}$	T* (K), $Li_7La_3Sn_2O_{12}$	T* (K), $Li_7La_3Hf_2O_{12}$
0.01	840	837	857
0.1	855	852	872
1.0	869	868	889
10.0	885	884	906
P_{H2O} (bar)	T* (K), $Li_7La_3Zr_2O_{12}$	T* (K), $Li_7La_3Sn_2O_{12}$	T* (K), $Li_7La_3Hf_2O_{12}$
0.01	452	424	432
0.1	460	433	440
1.0	469	441	449
10.0	478	450	458

Among a set of materials, Li garnet-related structures with higher critical temperatures are more susceptible to carbonate and hydroxide formation and are less chemically stable. As seen in Table 8.3, all three materials have a lower critical temperature for the hydroxide formation reaction than for carbonate formation reaction. In other words, all three materials are more stable with respect to H_2O than to CO_2. In Table 8.3, in the range of pressures between 0.01 bar and 10.0 bar, the chemical stability ranking with respect to CO_2 is $Li_7La_3Sn_2O_{12} > Li_7La_3Zr_2O_{12} > Li_7La_3Hf_2O_{12}$. In the pressure range of H_2O from 0.01 bar to 10.0 bar, the chemical stability ranking with respect to H_2O is $Li_7La_3Sn_2O_{12} > Li_7La_3Hf_2O_{12} > Li_7La_3Zr_2O_{12}$. The differences in stability between the Sn, Zr, and Hf-containing materials, however, are small.
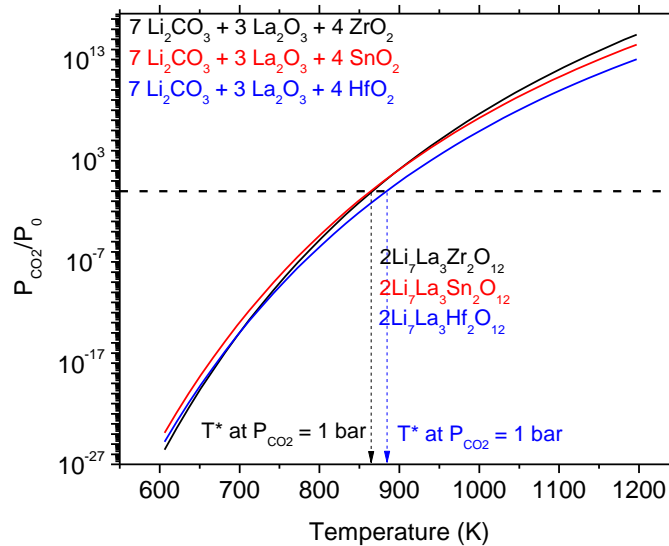
Figure 8.3: van't Hoff plot for the carbonate formation reaction of $Li_7La_3Zr_2O_{12}$, $Li_7La_3Sn_2O_{12}$, and $Li_7La_3Hf_2O_{12}$. The horizontal dashed line refers to $P_{CO2}/P_0 = 1$.

$2\ Li_7La_3M_2O_{12} + 7\ CO_2 \leftrightarrow 7\ Li_2CO_3 + 3\ La_2O_3 + 4\ MO_2$ for M = Zr, Sn, or Hf.
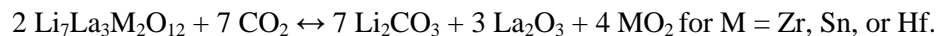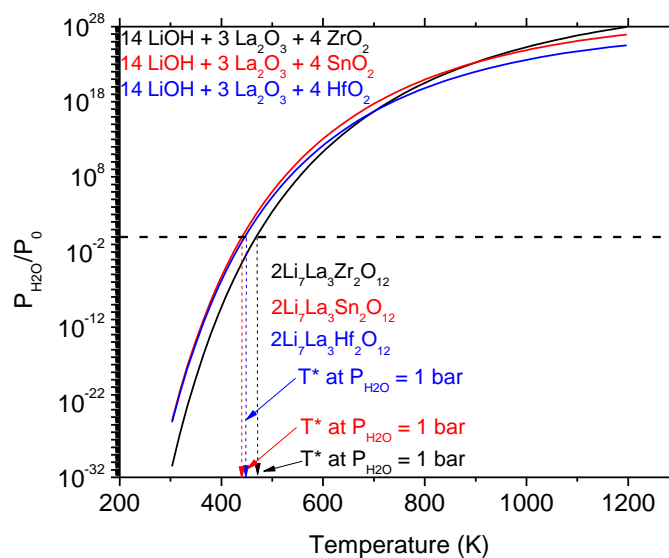
Figure 8.4: van't Hoff plot for the hydroxide formation reaction of $Li_7La_3Zr_2O_{12}$, $Li_7La_3Sn_2O_{12}$, and $Li_7La_3Hf_2O_{12}$. The horizontal dashed line refers to $P_{CO2}/P_0 = 1$.

$2\ Li_7La_3M_2O_{12} + 7\ H_2O \leftrightarrow 14\ LiOH + 3\ La_2O_3 + 4\ MO_2$ for M = Zr, Sn, or Hf.
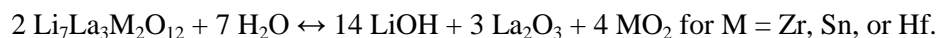
Because the stability of the Zr, Sn, and Hf-containing materials is similar, the ranking of their predicted stability depends on the partial pressure of CO_2 or H_2O. At low CO_2 pressures, $Li_7La_3Sn_2O_{12}$ has a lower critical temperature than $Li_7La_3Zr_2O_{12}$. $Li_7La_3Sn_2O_{12}$ also has a lower critical temperature than $Li_7La_3Zr_2O_{12}$ at low H_2O pressures.
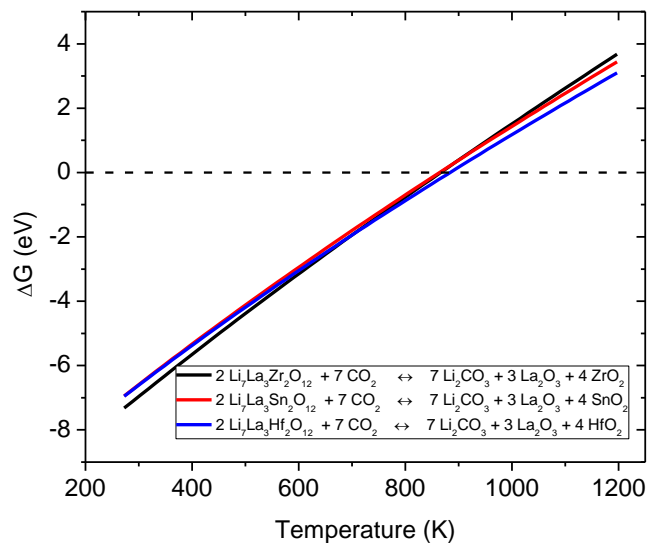
Figure 8.5: Free energy of reaction, ΔG, as a function of temperature for carbonate formation reactions. The results correspond to the reaction
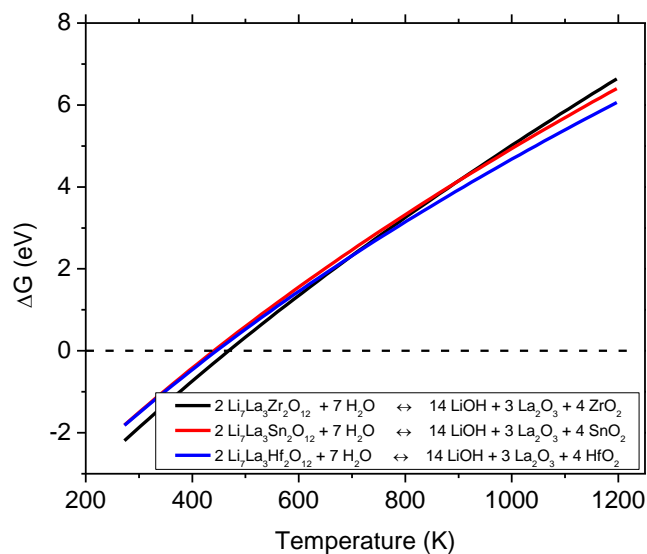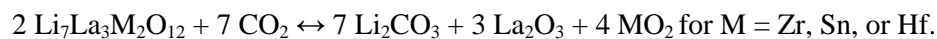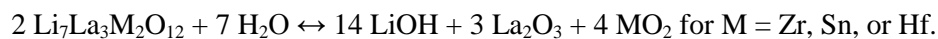
$$2\ Li_7La_3M_2O_{12} + 7\ CO_2 \leftrightarrow 7\ Li_2CO_3 + 3\ La_2O_3 + 4\ MO_2 \text{ for M = Zr, Sn, or Hf.}$$

Figure 8.6: Free energy of reaction, ΔG, as a function of temperature for hydroxide formation reactions. The results correspond to the reaction

$$2\ Li_7La_3M_2O_{12} + 7\ H_2O \leftrightarrow 14\ LiOH + 3\ La_2O_3 + 4\ MO_2 \text{ for M = Zr, Sn, or Hf.}$$

171

A stability diagram for $Li_7La_3Zr_2O_{12}$, $Li_7La_3Sn_2O_{12}$, and $Li_7La_3Hf_2O_{12}$ is shown in Figure 8.5 for a CO_2 pressure of 1 bar. Figure 8.5 shows that the rankings of the chemical stabilities of $Li_7La_3M_2O_{12}$ with respect to CO_2 are $Li_7La_3Sn_2O_{12}$ (T* = 868 K) > $Li_7La_3Zr_2O_{12}$ (T* = 869 K) > $Li_7La_3Hf_2O_{12}$ (T* = 889 K). This difference of the critical temperature between $Li_7La_3Zr_2O_{12}$ and $Li_7La_3Sn_2O_{12}$ is almost negligible. For the chemical stability with respect to H_2O, a stability diagram for $Li_7La_3Zr_2O_{12}$, $Li_7La_3Sn_2O_{12}$, and $Li_7La_3Hf_2O_{12}$ is shown in Figure 8.6 for a H_2O pressure of 1 bar. Figure 8.6 shows that the rankings of the chemical stabilities of $Li_7La_3M_2O_{12}$ with respect to H_2O are $Li_7La_3Sn_2O_{12}$ (T* = 441 K) > $Li_7La_3Hf_2O_{12}$ (T* = 449 K) > $Li_7La_3Zr_2O_{12}$ (T* = 469 K).

Under atmospheric dry air conditions (P_{CO2} = 400 ppm), the rankings of the chemical stability of $Li_7La_3M_2O_{12}$ with respect to CO_2 are $Li_7La_3Sn_2O_{12}$ (T* = 817 K) > $Li_7La_3Zr_2O_{12}$ (T* = 821 K) > $Li_7La_3Hf_2O_{12}$ (T* = 835 K). The vapor pressure of water (P_{H2O}) increases as temperature increases based on the Antoine equation[34] that gives vapor pressure of water as a function of temperature. For example, P_{H2O} = 2.44 bar at T = 400 K, and under the conditions of P_{H2O} = 2.44 bar, the rankings of chemical stability of $Li_7La_3M_2O_{12}$ with respect to H_2O are $Li_7La_3Sn_2O_{12}$ (T* = 444 K) > $Li_7La_3Hf_2O_{12}$ (T* = 452 K) > $Li_7La_3Zr_2O_{12}$ (T* = 472 K). Because all T* of these three materials are higher than the temperature we used, all three are unstable against H_2O at this vapor pressure of water.

8.4   Conclusion

In this chapter, we have used DFT calculations to examine the chemical stability of $Li_7La_3Zr_2O_{12}$, $Li_7La_3Sn_2O_{12}$, and $Li_7La_3Hf_2O_{12}$ with respect to carbonate and hydroxide formation reactions in environments with CO_2 and H_2O. The chemical stability of $Li_7La_3Sn_2O_{12}$ is higher than $Li_7La_3Zr_2O_{12}$ and $Li_7La_3Hf_2O_{12}$ with respect to both carbonate and hydroxide formation reactions at 1 bar of CO_2 partial pressure. The chemical stabilities of $Li_7La_3Zr_2O_{12}$ and $Li_7La_3Sn_2O_{12}$, however, are very similar to each other in terms of their carbonate formation reactions at 1 bar of CO_2 partial pressure. Since the chemical stabilities of the $Li_7La_3Zr_2O_{12}$, $Li_7La_3Sn_2O_{12}$, and $Li_7La_3Hf_2O_{12}$ are similar, the ranking of their predicted chemical stability depends on the partial pressure of CO_2 or H_2O. Therefore, depending on the partial pressure of CO_2 and H_2O, the choice of an appropriate garnet-related material can be made. At an atmospheric dry air condition, $Li_7La_3Sn_2O_{12}$ has higher chemical stability than $Li_7La_3Zr_2O_{12}$ with a clear difference of their critical temperatures.

The partial pressure of water vapor can be affected by temperature, and indirectly this saturated pressure of water impacts on chemical stabilities of $Li_7La_3Zr_2O_{12}$, $Li_7La_3Sn_2O_{12}$, and $Li_7La_3Hf_2O_{12}$. In other words, we can control the moist air conditions with different pressures of water vapor by changing temperature, and choose an appropriate material among three garnet-related materials.

8.5   References

1.   Knauth, P., *Solid State Ionics* **2009**, 180, 911-916.
2.   Park, M., Zhang, X. C., Chung, M. D., Less, G. B., Sastry, A. M., *J. Power Sources* **2010**, 195, 7904-7929.
3.   West, W. C., Whitacre, J. F., Lim, J. R., *J. Power Sources* **2004**, 126, 134-138.
4.   Yu, X. H., Bates, J. B., Jellison, G. E., Hart, F. X., *J. Electrochem. Soc.* **1997**, 144, 524.
5.   Seo, I., Martin, S. W., *Inorg. Chem.* **2011**, 50, 2143-2150.
6.   Bates, J. B., Dudney, N. J., Gruzalski, G. R., Zuhr, R. A., Choudhury, A., Luck, C. F., Robertson, J. D., *J. Power Sources* **1993**, 43, 103-110.
7.   Jones, S. D., Jr, A., *Solid State Ionics* **1992**, 53, 628-634.
8.   Thangadurai, V., Weppner, W., *Ionics* **2006**, 12, 81-92.
9.   Inaguma, Y., Chen, L. Q., Itoh, M., Nakamura, T., Uchida, T., Ikuta, H., Wakihara, M., *Solid State Commun* **1993**, 86, 689-693.
10.   Kotobuki, M., Munakata, H., Kanamura, K., *J. Power Sources* **2011**, 196, 6947-6950.
11.   Nakayama, M., Usui, T., Uchimoto, Y., Wakihara, M., Yamamoto, M., *J. Phys. Chem. B* **2005**, 109, 4135-4143.
12.   Murugan, R., Thangadurai, V., Weppner, W., *Angew. Chem. Int. Ed.* **2007**, 46, 7778.
13.   Thangadurai, V., Kaack, H., Weppner, W. J. F., *J. Am. Ceram. Soc.* **2003**, 86, 437-440.
14.   Percival, J., Kendrick, E., Smith, R. I., Slater, P. R., *Dalton Trans.* **2009**, 5177.
15.   Galven, C., Fourquet, J. L., Crosnier-Lopez, M. P., Le Berre, F., *Chem. Mat.* **2011**, 23, 1892-1900.
16.   Awaka, J., Kijima, N., Kataoka, K., Hayakawa, H., Ohshima, K., Akimoto, J., *J. Solid State Chem.* **2010**, 183, 180-185.
17.   The Inorganic Crystal Structure Database (ICSD). The Inorganic Crystal Structure Database (ICSD) http://www.fiz-informationsdienste.de/en/DB/icsd/.
18.   Kresse, G., Joubert, D., *Phys. Rev. B* **1999**, 59, 1758.
19.   Monkhorst, H. J., Pack, J. D., *Phys. Rev. B* **1976**, 13, 5188-5192.
20.   Ackland, G. J., *J. Phys.: Condens. Matter* **2002**, 14, 2975.
21.   Alapati, S. V., Johnson, J. K., Sholl, D. S., *J. Alloys Compd.* **2007**, 446, 23.
22.   Kang, S. G., Sholl, D. S., *RSC Adv*. **2013**, 3, 3333-3341.
23.   Parlinski, K. Software PHONON, 2005.
24.   Mortimer, R. G., Physical Chemistry. 2nd ed., (Academic Press, New York, 2000).
25.   Gygi, F., Galli, G., *Phys. Rev. B* **1995**, 52, 2229-2232.
26.   Chaplin, M. See http://www.lsbu.ac.uk/water for Water Structure and Science.
27.   Chase, M. J. W., *J. Phys. Chem. Ref. Data Monogr.* **1998**, 9, 1.
28.   Awaka, J., Kijima, N., Hayakawa, H., Akimoto, J., *J. Solid State Chem.* **2009**, 182, 2046-2052.
29.   Kokal, I., Somer, M., Notten, P. H. L., Hintzen, H. T., *Solid State Ionics* **2011**, 185, 42.
30.   Rangasamy, E., Wolfenstine, J., Sakamoto, J., *Solid State Ionics* **2012**, 206, 28.

31. Ohta, S., Kobayashi, T., Asaoka, T., *J. Power Sources* **2011**, 196, 3342-3345.
32. Kotobuki, M., Munakata, H., Kanamura, K., Sato, Y., Yoshida, T., *J. Electrochem. Soc.* **2010**, 157, 1076-1079.
33. Bernstein, N., Johannes, M. D., Hoang, K., *Phys. Rev. Lett.* **2012**, 109, 205702.
34. Antoine, C., *C. R. Hebd. Seances Acad. Sci.* **1888**, 107, 778

CHAPTER 9

CONCLUSION

Metal membranes are ideal for high-temperature hydrogen purification.[1] Pd-based metal membranes have attracted significant attention for H_2 purification due to their effectively infinite selectivity for H_2 over other gases.[2] By separating H from a CO_2-rich stream, Pd membranes could be helpful in carbon sequestration from gasification processes.[3] Because pure Pd membranes are susceptible to H_2-induced embrittlement and sulfur poisoning, Pd-based metal alloys are useful to improve the performance of pure Pd membranes.

Proton-conducting perovskites work as electrolytes, the center of a fuel cell. Transport through electrolytes should be highly selective and fast. High proton conductivity and good chemical stability are prerequisites for the application of proton-conducting perovskites.

Solid-state lithium ionic conductors are considered promising as clean and safe energy storage systems.[4] Li garnet-related structures are considered to be promising as fast ion-conducting electrolytes in solid-state lithium-ion batteries.[5]

In Chapter 3, our efficient DFT-based modeling broadens the available information on hydrogen permeation for a wide range of materials, since we study hydrogen permeation through *all* FCC Pd-rich binary alloys. Among several new alloys that have higher hydrogen permeability than pure Pd, $Pd_{96}Tm_4$ shows the highest hydrogen permeability. Experimental tests were performed by our collaborators with $Pd_{95.5}Tm_{4.5}$ (at. %) and confirmed that this binary alloy has higher hydrogen permeability

than pure Pd and the PdAg binary alloy, which is an industry standard alloy. Unfortunately, $Pd_{94}Tm_4$ is not ideal for the development of high flux membranes, because the experiments showed significant embrittlement at moderate temperatures or high H_2 pressures. Nevertheless, our theoretical predictions provide an effective complement to experiments in the development of practical metal membranes for H_2 purification.

In Chapter 4, we perform Density Functional Theory (DFT) calculations to predict the chemical stability and proton conductivity in perovskites, specifically in B-site doped $BaZrO_3$. We examine the physical relationship between chemical stability and proton conductivity and find that there is a simple tradeoff between these two properties.

In Chapter 5, among the monovalent A-site dopants we examine, K shows the highest proton conductivity and chemical stability in A-site doped $BaZrO_3$. Motivated by these results, we examine the relative proton formation energies of (K,M_2)-doped $BaZrO_3$, because proton formation energies play a more important role in determining proton conductivity than proton diffusivity.

In Chapter 6, we examine the chemical stability and proton conductivity in B-site doped $BaSnO_3$ and $BaHfO_3$. Improvements in the chemical stability cause decreased proton conductivity and *vice versa*. We find that B-site doped $BaHfO_3$ is promising to study further with (M_1,M_2)-doping, since it shows both higher proton conductivity and chemical stability than B-site doped-$BaZrO_3$.

In Chapter 7, we study properties of proton transport in $KTaO_3$ (KTO), including quantum tunneling and isotope effects. We find that tunneling is negligible, but zero point energy effects lead to non-negligible isotope effects for H^+, D^+, and T^+ at elevated temperatures. We probed the electronic and structural properties of native point defects in

KTO. Coulomb charge repulsion exists between protons and oxygen vacancies, whereas there is electrostatic attraction between protons and potassium vacancies. This electrostatic attraction may inhibit the mobility of protons in KTO. From our formation energy studies, protons have the lowest formation energies near potassium vacancies. Our main conclusion is that potassium vacancy sites are trap sites while oxygen vacancy sites act as anti-trap sites for protons. Another important conclusion is that proton diffusivity decreases as the concentration of oxygen vacancies increases. These fundamental results for undoped perovskites will aid in more completely characterizing proton conductivity in doped perovskites in the future.

In Chapter 8, we study chemical stability of Li garnet-related structures of $Li_7La_3Zr_2O_{12}$, $Li_7La_3Sn_2O_{12}$, and $Li_7La_3Hf_2O_{12}$ with respect to carbonate formation and hydroxide formation reactions. These materials are considered for use in Li ion-conducting electrolytes in solid-state lithium-ion batteries. We find that $Li_7La_3Sn_2O_{12}$ has higher chemical stability than $Li_7La_3Zr_2O_{12}$ and $Li_7La_3Hf_2O_{12}$ with respect to carbonate and hydroxide formation at low pressures of CO_2 and H_2O. However, the ranking of these materials according to their chemical stability with respect to carbonate and hydroxide formation changes at higher pressures of CO_2 and H_2O.

9.1 References

1. Sholl, D. S., Ma, Y. H., *MRS Bull.* **2006**, 31, 770-773.
2. Su, C., Jin, T., Kuraoka, K., Matsumara, Y., Yazawa, T., *Ind. Eng. Chem. Res.* **2005**, 44, 3053.
3. Paglieri, S.N., Way, J.D., *Sep. Purif. Meth.* **2002,** 31, 1-169.
4. Knauth, P., *Solid State Ionics* **2009**, 180, 911-916.
5. Murugan, R., Thangadurai, V., Weppner, W., *Angew. Chem. Int. Ed.* **2007**, 46, 7778.